"Metal oxides for thermoelectrics"

Dissertation

zur Erlangung des akademischen Grades eines
"Doktor der Naturwissenschaften"

am Fachbereich Chemie, Pharmazie
und Geowissenschaften der

Johannes Gutenberg-Universität Mainz

Giacomo Cerretti

Geboren am 3. Oktober 1985 in Sarzana, Italien

Mainz, Januar 2017

Dekan:

First Supervisor:

Second Supervisor:

Day of Defense: 30/03/2017

To my wife Valeria.

The work for this thesis was carried out at the *Johannes Gutenberg-Universität Mainz* during the period between 1st October 2013 and 10th December 2016 under the guidance of PROF. DR. WOLFGANG TREMEL.

I hereby declare that I wrote the submitted dissertation without any unauthorized external assistance and I used only sources acknowledged in the work. All textual passages, which are appropriated verbatim or paraphrased from published and unpublished texts, as well as all information obtained from oral sources are duly indicated and listed in accordance with bibliographical rules. In carrying out this research, I complied with the rules of standard scientific practice as formulated in the statutes of the Johannes Gutenberg-Universität Mainz to insure standard scientific practice.

Mainz, 26 January 2017.

Giacomo Cerretti

Publications

1. **G. Cerretti**, M. Schrade, X. Song, B. Balke, M. Panthöfer, I. Lieberwirth, T. Norby, W.Tremel, "Thermal stability and enhanced thermoelectric properties of the tetragonal tungsten bronzes $Nb_{8-x}W_{9+x}O_{47}$ ($0 < x < 5$)" *J. Mater. Chem. A*, submitted.

2. **G. Cerretti**, B. Balke, G. Kieslich, W. Tremel, "Towards higher zT in early transition metal oxides: optimizing the charge carrier concentration of the WO_{3-x} compounds" *Materials Today: Proceedings*, submitted.

3. J. Luo, **G. Cerretti**, B. Krause, L. Zhang, T. Otto, W. Jenschke, M. Ullrich, W. Tremel, B. Voit, P. Pötschke, "Polypropylene-based melt mixed composites with singlewalled carbon nanotubes for thermoelectric applications: Switching from p-type to n-type by the addition of polyethylene glycol" *Polymer*, accepted.

4. **G. Cerretti**, D. Martella, H. Zeng, C. Parmeggiani, S. Palagi, A. G. Mark, K. Melde, T. Qiu, P. Fischer, D. S. Wiersma, "Towards Photo-Induced Swimming: Actuation of Liquid Crystalline Elastomer in Water" *Proc. SPIE* 9738, **2016**, 97380T.
   doi:10.1117/12.2219855

5. G. Kieslich[#], **G. Cerretti**[#], I. Veremchuk, R. P. Hermann, M. Panthöfer, J. Grin, W. Tremel, "A chemists view: Metal oxides with adaptive structures for thermoelectric applications" *Phys. Status Solidi A*, **2016**, 213, 3, 808-823.
   doi:10.1002/pssa.201532702

6. C. P. Heinrich[#], M. Schrade[#], **G. Cerretti**, I. Lieberwirth, P. Leidich, A. Schmitz, H. Fjeld, E. Mueller, T. G. Finstad, T. Norby, W. Tremel. "Tetragonal tungsten bronzes $Nb_{8-x}W_{9+x}O_{47-\delta}$: optimization strategies and transport properties of a new n-type thermoelectric oxide" *Mater. Horiz.*, **2015**, 2, 519-527.
   doi:10.1039/C5MH00033E

7. H. Zeng, P. Wasylczyk, **G. Cerretti**, D. Martella, C. Parmeggiani, D. S. Wiersma. "Alignment engineering in liquid crystalline elastomers: Free-form microstructures with multiple functionalities" *Appl. Phys. Lett.*, **2015**, 106, 111902.
   doi:10.1063/1.4915268

8.   H. Zeng, D. Martella, P. Wasylczyk, **G. Cerretti**, J. C. Gomez Lavocat, C. H. Ho, C. Parmeggiani, D. S. Wiersma. "Liquid-Crystalline Elastomers: High-Resolution 3D Direct Laser Writing for Liquid-Crystalline Elastomer Microstructures" *Adv. Mater.*, **2014**, 26, 2319-2322.
        doi:10.1002/adma.201470095

[#] Co-first authorship

Acknowledgments

First, I would like to thank my supervisor Prof. Dr. ███████████ for giving me the opportunity to join his research group and to expand my knowledge working on such an interesting topic. Thanks a lot for the stimulating conversations and for the useful advices provided during the time of my Ph.D..

The sincerest thanks to Dr. ███████████ for all the support and for always finding the time for me to discuss about professional as well as personal issues. I am very happy that what started as a working collaboration, became over the time a good friendship.

Thanks also to Dr. ███████████ for the constructive discussions and for the help provided at the beginning of my Ph.D..

I would like to thank Prof. Dr. ███████████ for giving me the opportunity to work with the SPS and for agreeing in being my second thesis supervisor.

I would like to acknowledge also Dr. ███████████ (FERMIO – Oslo), Prof. Dr. ███████████ and ███████████ (DLR – Köln) for the fruitful collaborations and helpful discussions.

I want to express my gratitude to ███████████ for his help and availability, and for the always pleasant conversations.

Thank you to all the "old" (Dr. ███████████ Dr. ███████████, Dr. ███████████ and Dr. ███████████) and the "new" (███████████, ███████████ ███████████ ███████████ members of the thermoelectric subgroup for the good working relation and for the useful and enjoyable discussions, not only during the meetings. An extra thanks goes to ███████████ for helping me with the German version of the Abstract.

I would like to say thank you to all the colleagues and friends of the Tremel's group for the nice time and for all the occasions and parties in which we had a lot of fun. A special thank goes to Dr. ███████████ and to Dr. ███████████ for the great time we had together, not only partying and having coffee, but also in the everyday circumstances. Most of all thank you for being my friends. Furthermore, I am very grateful to Dr. ███████████ for the helpful advices and the pleasant discussions, especially during the writing time.

Many thanks to the DFG and the SPP1386 for the research funding and for making it possible to meet great people during their meetings, the summer schools and the conferences.

Finally, I want to acknowledge my family and friends. A huge thank goes to my wife ███████ for being such an amazing person, for supporting me no matter what, and for always being at my side even in the toughest moments. Thank you for teaching me a lot and for making me a better person.

Thanks a lot to my parents, to ████████████████████████ for being a fantastic family and for always being there for me and ████████. Many thanks also to all the other members of the Italian and Bolivian family. You are too many to say thanks to each one of you, but you know that I mean it.

I want to say thanks to my good friends scattered in the world, and a big thanks to all the Mainz friends. You made these three years really memorable with all the fun we had together during our discussions, parties, dinners, movie nights, wine testing, excursions, trips, brunches, sports… I am very grateful for having met you.

Abstract

The goal of this work is to investigate the synthesis, the stability, and the thermoelectric properties of some binary and ternary early transition metal oxides with adaptive structures. The biggest advantages of metal oxides are their extremely low costs paired with low or no toxicity, high abundance, and long term stability. On the other hand, their break-through as thermoelectric materials has been limited by their low figure of merit ($zT = S^2T/\rho\kappa$) caused by the low mobility of the charge carriers and a generally high thermal conductivity. Nevertheless, the research on the thermoelectric oxides is still a relatively new field, and therefore there is much space for improvement. In this scenario, metal oxide with adaptive structures could overcome most of the limitation of the metal oxides. The combination of intrinsic defects and large unit cells along with the possibility of manipulating the electronic transport properties independently from the thermal properties, make them promising candidates for high temperature thermoelectric applications.

The focus of this thesis lies on the study of metal oxides systems with adaptive structures. In detail, the thermoelectric optimization of the tungsten Magnéli phase $WO_{2.90}$, the thermoelectric properties and the stability of the tetragonal tungsten bronze series $Nb_{8-x}W_{9+x}O_{47}$, and the synthesis of reduced molybdenum oxides have been thoroughly investigated.

In the literature for the tungsten Magnéli phase $WO_{2.90}$ promising thermoelectric properties are reported. It shows a relatively low thermal conductivity (≈ 3.5 $Wm^{-1}K^{-1}$) due to the presence of crystallographic shear (CS) planes, coupled with a good electrical conductivity. The main reason of the low figure of merit of this material is caused by the high charge carrier concentration. Therefore, the optimization strategy relies on the reduction of the charge carrier density. Since this compound is an n-type conductor, the decrease of the electron count was achieved by increasing the oxygen content up to a nominal composition $WO_{2.91}$. This manipulation was beneficial to the thermoelectric properties of the compound, resulting in an improvement of the figure of merit of about 30% compared to the reference $WO_{2.90}$ compound. The highest measured value of zT was 0.24 at 1200 K.

The n-type tetragonal tungsten bronze (TTB) series $Nb_{8-x}W_{9+x}O_{47}$ shows intrinsic crystal defects which are similar to those observed in the Magnéli phases. This nanostructure containing crystallographic shear (CS) planes leads to low thermal conductivity values. The change of the cation composition and the concomitant change of the charge carrier concentration, does not substantially affect the crystal structure, and therefore the thermal transport properties for all the members of the series. Therefore, the substitution of niobium with tungsten allows a decoupled variation of the thermoelectric properties. To study the potential of these compounds, samples with low substitution degree $x = 0, 0.075, 0.1, 1$ and 2 were synthesized and structurally characterized. The thermal stability and the oxygen deficiency were studied together with the thermoelectric transport properties. Both cation substitution and the oxygen deficiency lead to an enhancement of the transport properties.

The second part of the investigation focused on the highly substituted compounds of the series: $Nb_5W_{12}O_{47}$ $(x = 3)$ and $Nb_4W_{13}O_{47}$ $(x = 4)$. These two compositions have been synthesized as pure polycrystalline samples. Subsequently, their chemical and physical stability when subjected to thermal cycling was studied. A complete thermoelectric characterization of the substituted TTB was carried out. A second set of measurements was done on the devices available at the University of Oslo (FERMIO), to verify the reproducibility of the obtained results. The X-ray analysis of powder patterns at different stages of the investigation, and the agreement of the cycled measurements results confirmed the high stability of the samples.

Finally, another transition metal oxide from the Magnéli-type phases was investigated. Some components of the molybdenum oxide family MoO_{3-x} were synthesized by solid state reactions. After optimization of the synthesis conditions, it was possible to obtain polycrystalline powders of γ-Mo_4O_{11}, $Mo_{17}O_{47}$, and $Mo_{18}O_{52}$ whose purity was confirmed by PXRD measurements. Spark plasma sintering (SPS) was used to consolidate dense pellets, but all attempts in SPS led to the formation of side phases. Therefore, a thorough study of the sintering conditions has to be performed to obtain pure phase pellets that can be used for the thermoelectric characterization.

Abstract - German

Ziel der vorliegenden Arbeit ist die Optimirung der Synthese, der Stabilität und der thermoelektrischen Eigenschaften von binären und ternären Übergangsmetalloxiden mit adaptiven Strukturen. Die größten Vorteile von Metalloxiden sind ihre niedrigen Materialkosten gepaart mit geringer Toxizität, hoher Verfügbarkeit und Langzeitstabilität. Andererseits ist ihr Durchbruch als thermoelektrisches Materialien durch ihren geringe Gütefaktoren ($zT = S^2T/\rho\kappa$) begrenzt, die durch die geringe Beweglichkeit der Ladungsträger und eine allgemein hohe thermische Leitfähigkeit verursacht wird. Dennoch ist die Erforschung der thermoelektrischen Oxide noch ein relativ neues Gebiet mit großem Spielraum für Verbesserungen. In diesem Zusammenhang könnten Metalloxide mit adaptiven Strukturen die meisten Beschränkungen von Metalloxiden überwinden. Große Elementarzellen und eine hohe Defektdichte, kombiniert mit der Möglichkeit die elektronischen Transporteigenschaften unabhängig von den thermischen zu variieren, machen sie zu vielversprechenden Kandidaten für thermoelektrische Anwendungen bei hohen Temperaturen.

Der Schwerpunkt dieser Arbeit liegt auf der Untersuchung verschiedener Metalloxide mit adaptiven Strukturen. Die Optimierung der Magnéli-Phase $WO_{2.90}$, die thermoelektrischen Eigenschaften und Stabilität verschiedener tetragonaler Wolframbronzen $Nb_{8-x}W_{9+x}O_{47}$ und die Synthese einiger reduzierter Molybdänoxide wurden eingehend untersucht.

Die Magnéli-Phase $WO_{2.90}$ weist vielversprechende thermoelektrische Eigenschaften auf. So ist ihre thermische Leitfähigkeit durch das Vorhandensein von Scherebenen relativ niedrig ($\approx$ 3.5 $Wm^{-1}K^{-1}$) und sie besitzt zudem eine gute elektrische Leitfähigkeit. Hauptgrund für die niedrige Gütezahl bei diesen Materialien ist die hohe Zahl an Ladungsträgern. Daher konzentriert sich die hier vorgestellte Optimierungsstrategie auf die effektive Verringerung der Ladungsträgerdichte. Da diese Verbindung ein n-leitendes Material ist, wurde die Verringerung der Elektronenzahl dichte durch eine Erhöhung des Sauerstoffgehalts auf eine nominelle Zusammensetzung von $WO_{2.91}$ erreicht. Diese Verändung wirkte sich positiv auf die thermoelektrischen Eigenschaften der Verbindung aus und führte zu einer Verbesserung der

Gütezahl um ca. 30% im Vergleich zu $WO_{2.90}$. Der höchste gemessene zT-Wert betrug 0.24 bei 1200 K.

Die n-leitenden tetragonalen Wolframbronzen $Nb_{8-x}W_{9+x}O_{47}$ zeigen intrinsische Defekte, die denen der Magnéli-Phasen ähneln. Die schichtenförmige Nanostruktur, die sich aufgrund der kristallographischen Scherebenen bildet, garantiert niedrige Werte der thermischen Leitfähigkeit. Bei dieser Verbindungsreihe wirkt sich die Änderung der Kationenzusammensetzung und die damit verbundene Änderung der Ladungsträgerkonzentration nicht wesentlich auf die Kristallstruktur aus, wodurch alle Verbindungen ähnliche thermische Transporteigenschaften besitzen. Gleichzeitig ermöglicht die Substitution von Niob durch Wolfram eine entkoppelte Variation der elektrischen und thermischen Transporteigenschaften. Aus diesen Gründen wurden Verbindungen mit niedrigen Substitutionsgrad $x = 0$, 0.075, 0.1, 1, 2 synthetisiert und strukturell charakterisiert. Die thermische Stabilität und das Sauerstoffdefizit wurden zusammen mit den thermoelektrischen Transporteigenschaften bestimmt. Erste Untersuchungen zeigten, dass sowohl die Kationensubstitution als auch das induzierte Sauerstoffdefizit zu einer Verbesserung der thermoelektrischen Eigenschaften führt.

Aufgrund dieser Ergebnisse wurde im zweiten Teil der Untersuchung der Schwerpunkt auf die höhersubstituierten Verbindungen $Nb_5W_{12}O_{47}$ ($x = 3$) und $Nb_4W_{13}O_{47}$ ($x = 4$) gesetzt. Diese zwei Zusammensetzungen wurden in Form einphasiger polykristalliner Proben hergestellt deren chemische und physikalische Stabilität bei wiederholtem Aufheizen und Abkühlen untersucht wurden. Zudem wurde eine vollständige thermoelektrische Charakterisierung der Proben durchgeführt. Ein zweiter Satz Messungen wurde an den Geräten der Universität Oslo (FERMIO) erstellt, um die Reproduzierbarkeit der erhaltenen Ergebnisse zu überprüfen. Die Analyse der Röntgenpulverdiffraktogramme zu unterschiedlichen Zeitpunkten der Untersuchung und die Übereinstimmung mit den zyklisierten Messergebnissen bestätigte eine hohe Stabilität der Proben.

Abschließend wurde ein weiteres zu den Magnéli-Phasen gehörendes System von Übergangsmetalloxiden untersucht. Einige Verbindungen der Molybdänoxid-Familie MoO_{3-x} wurden durch klassische Festkörperreaktionen hergestellt. Durch die Optimierung der Synthesebedingungen konnten polykristalline Pulver von γ-Mo_4O_{11}, $Mo_{17}O_{47}$, und $Mo_{18}O_{52}$ erhalten werden, deren Reinheit durch PXRD-Messungen bestätigt wurde. Das Spark-Plasma-

Sinterverfahren wurde für die Verdichtung zu Tabletten verwendet. Dabei führten alle Versuche zur Bildung von Nebenphasen. Um einphasige Tabletten zu erhalten, die für die thermoelektrische Charakterisierung dieser Verbindungen verwendet werden können, muss daher in Zukunft eine umfassende Studie der Sinterbedingungen durchgeführt werden.

Table of Contents

List of Figures

List of Tables

List of symbols and notations

a, b, c	Lattice parameters
C_{11}	Elastic constant
C_p	Heat capacity
CS	Crystallographic shear
CWD	Charge density wave
D	Thermal diffusivity
d	Density
DSC	Differential Scanning Calorimetry
e	Electron charge
e^-	Electron
$\hbar$	Planck's constant
h^+	Holes
HRTEM	High resolution transmission electron microscopy
I	Electrical current
k_B	Boltzmann's constant
L	Lorenz number
LFA	Laser flash analysis
LSR	Linseis Seebeck & resistivity
M	Atomic mass
m^*	Effective mass
N	Number of atoms in the unit cell
n	Charge carrier concentration
NP	Nano powders
PF	Power factor
PV	Photovoltaic
PXRD	Powder X-ray diffraction
q	Phonon wave vector
$\dot{Q}$	Heat flow

S	Seebeck coefficient (thermopower)
SEM	Scanning electron microscopy
SPS	Spark plasma sintering
T	Temperature
T_C	Temperature cold side
T_H	Temperature hot side
TE	Thermoelectric
TEG	Thermoelectric generator
TG	Thermogravimetric
TTB	Tetragonal tungsten bronze
V	Voltage
zT	Figure of merit
$\overline{zT}$	Average figure of merit
η	Efficiency
η_C	Carnot efficiency
η_{TEG}	Thermoelectric generator efficiency
θ_D	Debye temperature
К	Thomson coefficient
κ	Thermal conductivity
κ_{el}	Electronic contribution of thermal conductivity
κ_L	Lattice contribution of thermal conductivity
Λ	Phonon mean free path
μ	Electron mobility
v_g	Group velocity of phonons
Π	Peltier coefficient
ρ	Electrical resistivity
σ	Electrical conductivity
τ	Relaxation time
$\overline{\tau}$	Scattering time
ω	Vibrational frequency

The content of the following chapter is partially taken and adapted from *Phys. Status Solidi* **2016**, *213*, 808–823[1]. Taken parts are delimited by quotation marks.

Authorship contributions

Category 1

Conception and design of study:

G. Kieslich, G. Cerretti, W. Tremel.

Acquisition of data:

G. Cerretti, G. Kieslich.

Analysis and/or interpretation of data:

G. Cerretti, G. Kieslich.

Category 2

Drafting the manuscript: G. Kieslich, G. Cerretti.

Revising the manuscript critically for important intellectual content: I. Veremchuk, R. P. Hermann, M. Panthöfer, J. Grin, W. Tremel.

Category 3

Approval of the version of the manuscript to be published:

G. Kieslich, G. Cerretti, I. Veremchuk, R. P. Hermann, M. Panthöfer, J. Grin, W. Tremel.

FIGURE 1.6: PREPARED BY G. KIESLICH.

FIGURE 1.9: PREPARED BY G. CERRETTI.

1 Introduction

1.1 Motivation

The inevitable depletion of the fossil fuels and the huge pollution that derives from their utilization along with the worldwide increasing demand for energy are some of the biggest challenges of our times. In the last years we observed a rapid escalation of the consequences of the global warming deriving from the worrying achieved levels of pollution. These reasons induced an always rising number of countries to focus their efforts on the development of cleaner and more sustainable ways of producing energy. Renewable energy sources and energy-efficiency technologies are believed to play a key role for the future energy revolution. At the moment, the most efficient renewable alternatives are represented by the wind-, the hydro- and the thermal-energy, but the research has investigated also other promising sources. Among them, photovoltaics (PV),[2–4] solar fuels,[5,6] batteries,[7–9] and thermoelectric (TE)[10–12] are the ones that attracted most attention. Thermoelectricity is a very interesting technology because it can be used to generate power through the direct conversion of heat into electrical energy, or can be used as heat sink in cooling applications. The complete lack of moving parts, which are always the most critical components of each machine, makes the thermoelectric modules truly fascinating devices.

Thermoelectric devices have already proven their high reliability. The most spectacular examples are the space missions Voyager I and II where a radioisotope-driven thermoelectric generator (TEG) acts as power source for more than 30 years.[13] In general, TEGs can be coupled with already existing systems, like industrial plants, cars or even solar cells, to increase the overall efficiency through the reutilization of otherwise lost heat. Indeed, most of the major car industries are starting to incorporate thermoelectric modules on their automobiles to further increase the efficiencies of the engines and reduce the CO_2 emissions.

Fuel Efficiency vs. Electrification: The Race is On

Thermoelectrics Boost MPG & Enable Computing Power for the Future Car

Thermoelectric generators (TEGs) **improve fuel efficiency by 5%** ▶ and provide necessary power for displays, sensors, LIDAR, and more.

eliminates 7,585,061 metric tons of CO^2 / year

Fuel Efficiency – US CAFE Standards

60
50
40
30
20

38.5 mpg

44.5 mpg

55.4 mpg

Today   **2020**   **2025**

Electrification – Estimated Power Requirements

1 kW*   +1 kW*   +2 kW*

Today's Car   **Connected Car**   **Semiautonomous**

*For every 100 watts needed for electrical power requirements, there is a 1% fuel efficiency loss.

10% lost efficiency / 1kWe = -3.85 mpg

20% lost efficiency / 2kWe = -7.7 mpg

Waste heat is valuable

Sources:
US EPA Greenhouse Gas Equivalencies Calculator
US EPA, NHTSA CAFE_2017-25_Fact Sheet
what-when-how.com/automobile/vehicle-electrical-loads-automobile/
+1kW and +2kW electrical power requirement are assumptions

Designed by:
alphabet energy
alphabetenergy.com

Figure 1.1: To meet the increased electrical power requirements of the future cars, several automotive industries are implementing the utilization of TEGs in their models to reduce the fuel consumption and the CO_2 emissions.[14]

To spread the commercialization of thermoelectric devices, the required materials need to have acceptable efficiencies and to fulfill certain parameters like cost, abundance, toxicity and stability. In this contest, metal oxides propose themselves as promising candidates for

applications. They are extremely cheap materials, due to their high abundance, they have low or no toxicity and they show very high physical and thermal stability. So far the biggest limitations to their break through are the low efficiencies, but there is a lot of space for improvement because the research in thermoelectric oxides is still a relatively new field.

The main aim of this work is to investigate and characterize different types of metal oxides for thermoelectric applications. The studied materials have been chosen among systems that, due to the presence of intrinsic crystal defects, ensure low thermal conductivity, a key requirement for a good thermoelectric material. From there on, a targeted optimization of the electron transport properties was pursued in order to increase the overall thermoelectric performances of the analyzed compounds.

In this chapter an introduction to the topic covered by this thesis will be provided. At the beginning the basic concepts and aspects that govern the thermoelectricity will be discussed. A concise discussion on the common used optimization strategies for thermoelectric materials will be also presented. Will be given an overview on the metal oxides with adaptive structures, a class of materials to which the compounds studied for this work belong, followed by an outlook of the thermoelectric properties of such compounds.

1.2 Thermoelectricity

1.2.1 History and basic concepts

Thermoelectricity is a two-way effect. It can refer to the direct conversion of a temperature difference into an electric voltage or, *vice versa*, to the generation of a temperature gradient when a voltage is applied. The first part of this phenomenon was discovered in 1821 by the Estonian-German physicist Thomas J. Seebeck. He found that a circuit made out of two dissimilar metals, with junctions at different temperatures, would deflect a compass magnet.[15] He did not realize that there was an electric current involved, and called the observed phenomenon the thermomagnetic effect. The Danish physicist Hans C. Ørsted recognize the true nature of this effect and coined the term "thermoelectricity". Further investigations led to the expression that links the produced voltage (ΔV) to the temperature difference of the junction (ΔT) and to the Seebeck coefficient (S).

$$\Delta V = S \cdot \Delta T \tag{1}$$

Later on the French physicist Jean C. A. Peltier, who studied the phenomenon in more detail, discovered that an electrical current would produce heating or cooling at the junction of two dissimilar metals. The Peltier coefficient (Π) is the proportionality constant that correlates the heat flow generated at the junction ($\dot{Q}$) with the applied electrical current (I).

$$\dot{Q} = (\Pi_A - \Pi_B) \cdot I \tag{2}$$

Twenty years later, William Thomson (also known as Lord Kelvin) issued a comprehensive explanation of the Seebeck and Peltier effects and described their interrelationship.[16] The two coefficients are related through thermodynamics and are proportional to the absolute temperature. This derivation lead Thomson to predict a third thermoelectric effect. In the Thomson effect, heat is absorbed or produced when current flows in a material with a

temperature gradient. The heat is proportional to both the electric current and the temperature gradient. The proportionality constant, known as the Thomson coefficient (K), is related by thermodynamics to the Seebeck coefficient.

$$K = T \cdot \frac{dS}{dT} \tag{3}$$

$$\Pi = T \cdot S \tag{4}$$

In terms of applications, the Peltier effect is used nowadays to create a refrigeration circuit which is compact and do not require circulating fluids or moving parts. On the other hand, the Seebeck effect is the one used in thermoelectric generators for the direct conversion of heat in usable electric current.

Thermoelectric devices are made of several thermoelectric couples consisting of n-type (excess electrons) and p-type (excess defect electrons) elements connected electrically in series and thermally in parallel (Figure 1.2). As a consequence of the temperature difference, the charge carriers (e^- and h^+) diffuse from the hot to the cold side of the p-n junction until an equilibrium is reached.

"The efficiency of a thermoelectric generator can be related to the materials properties using the laws of thermodynamics. A thermoelectric generator is a machine, converting heat into electric energy, and therefore its efficiency can be related to the efficiency of the Carnot process

$$\eta = \frac{W}{\dot{Q}} = \eta_C \cdot \eta_{TEG} = \frac{T_H - T_C}{T_H} \frac{\sqrt{1 + \overline{zT}} - 1}{\sqrt{1 + \overline{zT}} + \frac{T_C}{T_H}} \tag{5}$$

where W is the power generated, $\dot{Q}$ the net heat flow, η_c the Carnot efficiency, η_{TEG} the efficiency of the thermoelectric generator, $\overline{zT}$ is the average figure of merit, and T_C and T_H are the temperatures at the cold and hot sides, respectively. The thermoelectric figure of merit zT is a dimensionless factor that is commonly used to compare the quality of a thermoelectric

material since it contains both, the electrical and the thermal contributions to the materials properties.
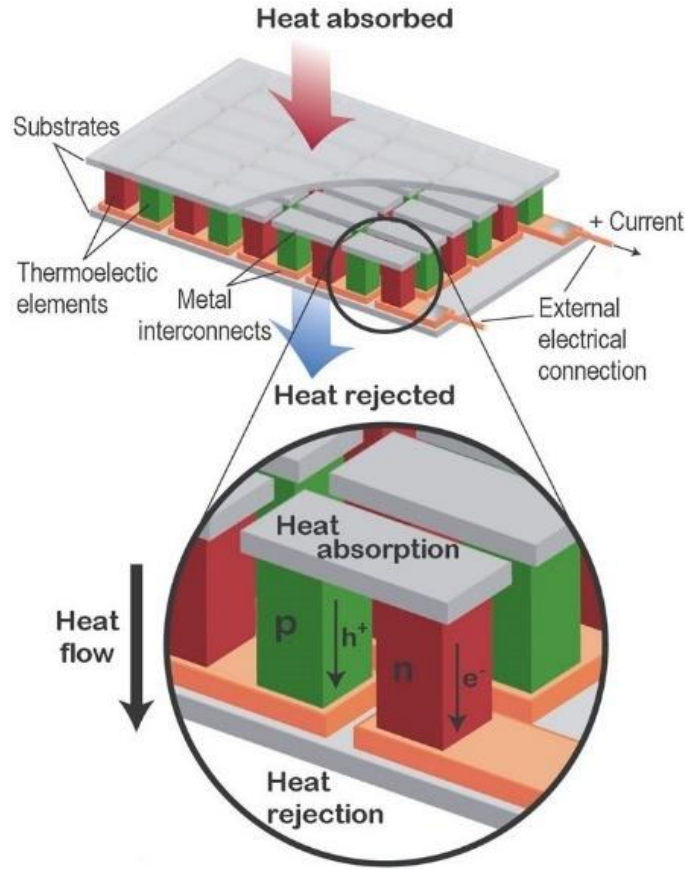
Figure 1.2: Schematic representation of a thermoelectric device with the thermoelectric elements connected electrically in series and thermally in parallel. In the zoomed section the thermal and the electric transport are shown. The charges, and the heat, diffuse from the hot to the cold side until an equilibrium is reached.[17]

$$zT = \frac{S^2\,T}{\rho\,\kappa} \tag{6}$$

Here S is the Seebeck coefficient (or thermopower), T the absolute temperature, ρ the electrical resistivity and κ the thermal conductivity. It reflects the requirements for a good thermoelectric material. Increasing a material's zT (i.e., the device efficiency) has been the challenge in the field of thermoelectric research since the late 50s. The big trade-off is the interrelation of the different variables, which makes the optimization of zT challenging.

From Eq. (6) can be noticed that the perfect thermoelectric material exhibits a glass-like thermal conductivity and electronic transport properties of a crystal, thus fulfilling the concept of a "phonon-glass electron-crystal" as put forward by Slack.[18]
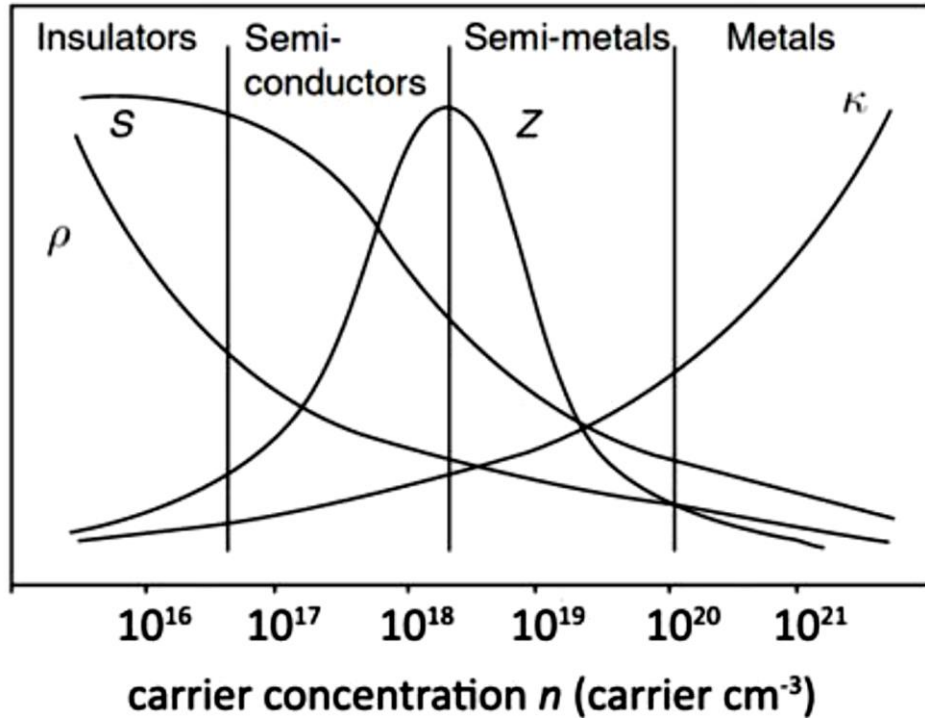
Figure 1.3: Representation of how the various parameters and the figure of merit vary in function of the charge carrier concentration. This strict correlation among the thermoelectric parameters makes it challenging to optimize the zT of the thermoelectric materials.[19]

In order to balance the interdependent thermal and electric transport properties of a material an in-depth understanding of the underlying transport mechanisms is essential.[20] There are qualitative guidelines for selecting a good thermoelectric material.[21] Very often however, the underlying transport processes can only be explained *a posteriori*, although the key variables have been identified. In the following sections these variables are briefly summarized and put into context for oxide materials."

1.2.2   Thermal transport

"Due to their intrinsic high thermal conductivity, arising from the low atomic mass of oxygen and strong bonding deriving from large differences in electronegativity, conductive oxides remained basically unrecognized as thermoelectric materials until almost 20 years ago when Terasaki et al[22] reported a large thermopower in Na_xCoO_2. This led to a surge of activities on cobaltites for thermoelectric applications. In parallel, the thermoelectric performance of oxides was improving steadily.[23]

In the solid state, the thermal conductivity κ occurs due to (i) lattice vibrations propagating through the lattice (phonons) and (ii) heat carrying charge carriers. In a first approximation it can be described as

$$\kappa = \kappa_L + \kappa_{el} \tag{7}$$

with κ_L being the lattice part of the thermal conductivity and κ_{el} the electronic part. Via the Boltzmann transport theory and the free electron theory the electronic contribution to thermal conductivity is given by the Wiedemann-Franz law[24]"

$$\kappa_{el} = L \cdot \sigma \cdot T \tag{8}$$

with L being the Lorenz number, σ the electrical conductivity, and T the temperature. The Lorenz number is equal to $2.4453 \cdot 10^{-8}$ $W\Omega K^{-2}$ for metals and highly degenerate semiconductors. Under the assumption of acoustic phonon scattering the Lorenz number for non-degenerate semiconductors reduces to $1.4866 \cdot 10^{-8}$ $W\Omega K^{-2}$. When the temperature is clearly above the Debye temperature θ_D ($T \gg \theta_D$) and below the Debye temperature ($T \ll \theta_D$) the Wiedemann-Franz law gives proper values for κ_{el}. At intermediate temperatures the law fails due to inelastic phonon scattering of the charge carriers, which leads to a lower value of the Lorenz number. "As κ_{el} is related to the electronic properties, and hence to the charge carriers, the challenge is to identify structural features reducing the lattice thermal conductivity toward the amorphous limit. In non-crystalline materials and glasses thermal transport can be

described using a random walk algorithm rather than by phonon scattering.[25] However, amorphous materials are poor thermoelectrics due to their unfavorable electronic transport properties. The lattice contribution to the overall thermal conductivity can be calculates as

$$\kappa_L = \frac{1}{3} C_P \cdot v_g \cdot \Lambda \qquad (9)$$

where C_P is the heat capacity, Λ is the mean free path of the phonons, and v_g is the group velocity of the phonons in a material. The heat in solids is transferred by vibrations of the lattice, which can be described as quasi particles (phonons). The high energetic optical phonons, which are not effective heat carriers, exhibit low group velocities but interact with acoustic phonons and influence the heat transfer.[26] These acoustic phonons are the main heat carriers and indeed their group velocity is high. In analogy to the thermal conductivity of an ideal gas, Eq. (9) describes the thermal conductivity of a "phonon-gas." A low heat capacity, a short mean free path and a low phonon group velocity are required for a low lattice thermal conductivity."
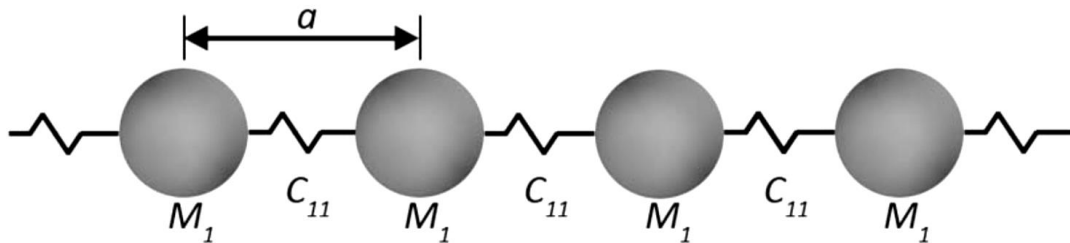
Figure 1.4: Illustration of a monoatomic chain with a unit cell length of *a* and a single atom composing it. Even if it is an extremely simplified model of a real solid, it can help understanding some important relations that concur in the definition of the lattice part of the thermal conductivity. Image adapted from literature.[19]

In Figure 1.4 the monoatomic chain with one atom in the unit cell is illustrated. At temperatures above the absolute zero, atoms start to oscillate around their equilibrium positions. In the simplified monoatomic model, the atoms are linked by equal springs with elastic constant C_{11} (bond strength), and the oscillations are highly coupled to neighboring atoms. Therefore, can

be noticed the importance of this constant. Applying Newton's law to the monoatomic model, the dispersion relation for a monoatomic chain can be calculated.

$$\omega = 2\sqrt{\frac{C_{11}}{M}}\left|\sin\left(\frac{qa}{2}\right)\right| \tag{10}$$

with

$$q = \frac{n\pi}{a} \tag{11}$$

being ω the vibrational frequency, M the atomic mass, q the phonon wave vector, and a the unit cell parameter. The phonon dispersion curves are usually plotted as q function of the vibrational frequency and the wave vector, and the phonon group velocities are the slopes of such curves. Since ω is periodic, it is sufficient to plot it over the interval from 0 to π/a.
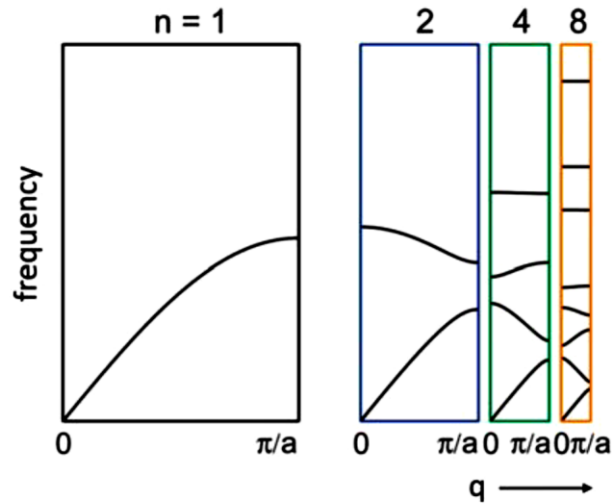
Figure 1.5: Plot of the phonon dispersion curves in function of the number of atoms (n) present in the unit cell. Increasing n, flat optical branches are introduced and this induce a lowering of the phonon group velocities.[27]

In Figure 1.5 a plot of the phonon dispersion curves is shown. By increasing the number of atoms in the unit cell (n), and hence increasing the unit cell length, a second branch is introduced. In general, a phonon dispersion curve has 3 acoustic components and 3n-3 optical components.

"Within the model of a harmonic, monoatomic chain the group phonon velocity can be linked to the bond energy through the force constants C_{11}.

$$v_g = a_0 \sqrt{\frac{C_{11}}{M}} \cos\left(\frac{qa}{2}\right) \tag{12}$$

In reality, the model of a monoatomic chain may be too simplified, but the dependence of the group velocity on the masses and coupling constants remains valid. Within the dominant phonon approximation, the phonon group velocity in a material corresponds to the sound velocity. This is a reasonable approximation since primarily acoustic phonons contribute to the heat conduction due to their higher group velocity and occupancy. With increasing volume of the primitive unit cell more optical branches appear in the phonon dispersion and therefore compounds with large unit cells should show low thermal conductivities. In addition, optical phonons can lead to anharmonic phonon scattering, as shown for PbTe where the absence of optical phonons leads to an increased lattice thermal conductivity.[28]

Similarly to the case of the ideal gas, the phonon mean free path Λ describes the average distance which phonons travel between two scattering events. The phonon mean free path allows tuning the thermal transport properties by incorporating scattering centers on several length scales. Phonons can be scattered by defects, (grain) boundaries and other phonons. This allows for reducing the thermal conductivity due to the introduction of artificial scattering centers, for instance in thin film multilayer systems. Manipulating the mean free path of phonons was the major approach to improve the zT of thermoelectric materials during the past decade.

The heat capacity at high temperatures is usually approximated by the Dulong–Petit rule. The term "high" is vague and depends on the Debye temperature of a material. Above the Debye temperature, all vibrational states of the material are occupied and C_P approaches the Dulong–Petit limit. Further uncertainties arise from the anharmonicity of the potential, which is not

included in the Dulong–Petit rule. Room temperature thermoelectric generator will have niche applications, because most waste heat is generated at temperatures above 600 K, where the Dulong–Petit rule is in general a good approximation. Elaborate estimations of the heat capacity of complex oxides are available,[29] however, for new materials an experimental determination of Debye temperature and heat capacity is required.[30]"

1.2.3 Electronic transport

"In this section an outline of the basic rules that govern the electrical conductivity of transition metal oxides is given.

An extensive datamining project by Gaultois et al[31] revealed that thermoelectric oxides should exhibit electrical resistivity < 0.1 Ω·cm. Formation of solid solutions ("doping") can often be employed in a straightforward manner to tune the carrier concentrations and to adjust the band gap and surface energy in metal oxides.

In the simplest approximation, the electrical conductivity σ, and its reciprocal the electrical resistivity ρ, are proportional to the charge carrier concentration as a function of the density of states $n(E)$.

$$\sigma = \frac{1}{\rho} = n(E) \cdot e \cdot \mu(E) = n(E) \cdot e^2 \cdot \frac{\tau(E)}{m^*} \tag{13}$$

e is the electronic charge and $\mu(E)$ is the charge carrier mobility, $\tau(E)$ is the relaxation time and m^* the effective mass. Most oxide have narrow bands and therefore a low charge carrier mobility and a large effective mass m^*.[32–35] As a result, the electrons in many transition metal oxides such as TiO_2 or layered cobaltites have large effective masses m^* and suffer from short scattering lengths. Indeed, the charge carrier mobility μ is a function of the electronic charge e, the effective mass m^* and the average scattering time $\bar{\tau}$.

$$\mu = \frac{e}{m^*} \bar{\tau} \tag{14}$$

To contrast the negative effect of low mobility, a relatively high carrier concentration is needed to obtain electrical resistivity < 0.1 Ω·cm. In addition, high charge carrier concentrations lead to high electronic thermal conductivities.

The Seebeck coefficient S is a measure of the magnitude of thermoelectric voltage in response to a temperature difference across a material. The Seebeck effect is caused by charge-carrier diffusion. The mobility and the charge carrier concentration are not only important for the electrical conductivity, but also for the magnitude of the Seebeck coefficient. It can be shown that for a degenerate semiconductor that has a parabolic band structure (it is a semiconductor that acts like a metal with pure acoustic phonon scattering of the carriers) the Seebeck coefficient is given by

$$S = \frac{8m^*\pi^2 k_B^2}{3e\hbar} T \left(\frac{\pi}{3n}\right)^{\frac{2}{3}} \tag{15}$$

Here n is the carrier concentration, m^* the carrier effective mass, e the electronic charge, T the temperature, $\hbar$ the Planck's constant, and k_B the Boltzmann's constant. Large S values in transition metal oxides arise from high effective masses (m^*) due to electronic correlations[36] and electron–electron interactions.[37] For semiconducting transition metal oxides, the simplified Seebeck coefficient S can be estimated by Eq. (15) which shows that a higher effective mass results in larger Seebeck coefficients. This explains the high S values observed in many transition metal oxides. Equation (15) also predicts that increasing temperature increases the Seebeck coefficient. Dramatically enhanced S values at elevated temperatures have been observed in many transition metal oxides such as ZnO.[38]"

1.3 TE oxides: state-of-the-art

"At first glance, oxides exhibit intrinsic properties that seem not easily compatible with the general guidelines for high zT materials. The performance is limited by the low mobility of the charge carriers and a comparatively high thermal conductivity. However, since the discovery of a large power factor (S^2/ρ) in cobaltites[22,36,37,39–45] the research on oxides for thermoelectric applications has advanced dramatically.
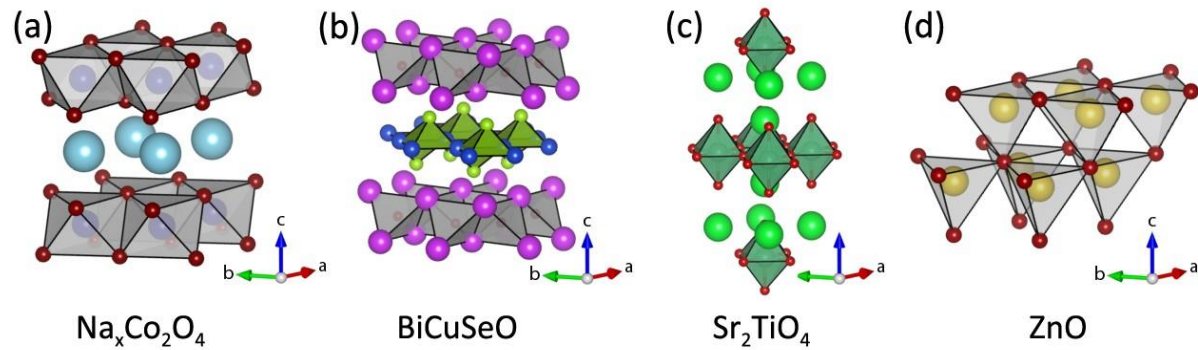
Figure 1.6: Crystal structures of *p*-type layered cobalt oxides (a) and oxyselenides (b) where the low lattice thermal conductivity can be associated with the layered structure. The Ruddlesden–Popper phase Sr$_2$TiO$_4$ ($n = 1$) is illustrated in (c). The perovskite is obtained for $n = \infty$, and ZnO which is currently the best *n*-type oxide thermoelectric is illustrated in (d).

1.3.1 Layered cobalt oxides

Currently, there is a gap between the thermoelectric properties of *p*-type and *n*-type materials, the first showing superior performance compared to the second that so far do not exceed the critical value of zT=1. Cobaltites are *p*-type materials with $zT \approx 1$ due to the beneficial electronic transport properties and a low thermal conductivity of 2 Wm^{-1}K^{-1}. Currently cobaltites with zT values around 1 and oxyselenides[46–49] represent the state-of-the-art *p*-type materials for oxides and oxide-related compounds. Their performance is attributed to a combination of their electronic properties and low thermal conductivity, which in turn is related to the underlying crystal structures. The reason for the electronic properties of Na$_x$CoO$_2$

is still under debate. Although considerations using Heikes formula[50] often led to reasonable values of the thermopower, the results need to be treated with care. Heikes formula describes the entropy per charge carrier in the high temperature limit and is applicable for polaron conductors, whereas cobaltites show electrical resistivities of ≈ 0.2 m$\Omega\cdot$cm, indicating a metal-like conduction mechanism. Koshibae et al[51] presented a modified version of Heikes formula in which they took in account also the degeneracy of the ions in the polaron conduction. This generalized formula held not only for the $NaCo_2O_4$ system, but also for the identification of new possible thermoelectric oxides like $La_{1-x}Sr_xCoO_3$,[52] the layered rhodium oxides $(Bi_{1-x}Pb_x)_{1.8}Sr_2Rh_{1.6}O_y$,[53] the doped $SrRuO_3$,[54] $La_{1-x}Sr_xVO_3$,[55] the perovskites $Pr_{0.5}Ca_{0.5}MnO_3$ and $Ca(Mn_{3-y}Cu_y)Mn_4O_{12}$,[56] the iron bases $SrFeO_x$,[57] and the layered cobaltites $RBaCo_2O_{5+x}$ (R = Gd, Nd).[58]

The most promising p-type oxide thermoelectric materials are alkali or alkaline-earth cobaltites with layered structures.[21,36,37,39–45] These compounds have large Seebeck coefficients, which are attributed to the low spin state of Co^{3+}.[51] Variations in the cobalt valence, as evidenced by the changes in oxygen content, have been reported to affect the thermoelectric properties of the related cobaltite $Ca_3Co_4O_9$.[59] Its structure contains $[CoO_2]$ planes, which provide a path for p-type electronic conduction, while the interfaces between the layers disrupt heat transfer by lattice phonons scattering. In $Ca_3Co_4O_9$ the $[CoO_2]$ planes are separated by a Ca_2CoO_3 layer with a NaCl-type structure, while in Na_xCoO_2, the $[CoO_2]$ sheets are separated by a layer of sodium ions (Figure 1.6). Alkaline earth compounds like Ca_xCoO_2,[60] Ba_xCoO_2,[61] or $Ca_3Co_2O_6$[62,63] can be formed as well. $Ca_3Co_2O_6$ has a large Seebeck coefficient, but its electrical conductivity is low. $Ca_3Co_4O_9$ and its derivatives have been popular targets of thermoelectric research.

1.3.2   Oxyselenides

BiCuSeO crystallizes in a ZrCuSiAs structure, which is based on a layering of two different square nets[64], which are mutually separated.[65] LaAgSO, a related phase with a Pearson hard LaO sublattice was studied as an ionic conductor very early. Due to the similarity of the ZrCuSiAs crystal structure with that of superconducting cuprates, oxychalcogenides were studied during the 1990s as potential high temperature superconductors.[66] Several

isostructural compounds of the general formula RMQO (R = Bi, Ce, Dy; M = Cu, Ag; Q = S, Se, Te) have been reported.[67,68] The semiconducting properties make the oxychalcogenides useful for optoelectronics.[69–71]

The large Seebeck coefficient of LaFeAsO around 100K is a promising indicator for thermoelectric cooling applications in the low-temperature range,[72] but the zT of oxychalcogenides is restricted by their electrical resistivity. Indeed, the high electrical resistivity is related to a low carrier concentration of 1×10^{18} cm^{-3} and a carrier mobility of 22 cm^{2}V^{-1}s^{-1}. The Seebeck coefficient of BiCuSeO is about 350 µVK^{-1} at room temperature, and rises to 425 µVK^{-1} at 923 K. The p-type conduction in pristine BiCuSeO is related to Cu vacancies. The total thermal conductivity of 0.60 Wm^{-1}K^{-1} at room temperature (decreasing to 0.40 Wm^{-1}K^{-1} at 923 K) is determined by the lattice part, as the electrical thermal conductivity is much lower than the values observed in other thermoelectric materials.[73,74] A relatively low power factor of 2.5 mWcm^{-1}K^2 at 923 K is overcompensated by a very low κ, which leads to a respectable zT value 0.5 at 923 K.[74] The electrical transport properties of BiCuSeO could be improved by doping with bivalent alkaline earth metals (Mg, Ca, Sr, and Ba).[75–78] An attempt to influence electronic transport substituting completely the chalcogen by a pnictogen leads immediately to a strong loss of thermoelectric performance due to the too large charge carrier concentration, e.g., in LaZnSbO.[79] In addition, the thermoelectric performance of BiCuSeO can be improved not only by introducing Cu vacancies and doping with Pb or tuning the band gap, but also by increasing the carrier mobility through grain texture.[80]

1.3.3   Ruddlesden-Popper phases

Highly reduced oxide ferroelectrics are another class of active materials. The parent compound strontium titanate ($SrTiO_3$) shows a strong structural tolerance with respect to the substitutional doping.[81,82] Due to its d-band nature, the effective mass of the carriers is quite large resulting in a large Seebeck coefficient S. In its pure form, $SrTiO_3$ is an insulating material, but it can be tuned to be semiconducting or metallic by substitutional doping with La^{3+} or Nb^{5+}.[82] The highest zT for a La^{3+} and Nb^{5+} doped $SrTiO_3$ single crystal is 0.1 at room temperature and 0.27 at 1000 K.[83–86] The zT values of SrTiO3 are limited by its thermal conductivity because even in the presence of dopant cations the phonon scattering by point defects is low.

18

Coupled ferroelectric–thermoelectric materials with oxygen deficiency have shown high power factors and nanoscale features, a result of oxygen vacancy clustering on the size scale of 5 - 10 nm. Examples include the tungsten bronze $Sr_xBa_{1-x}Nb_2O_{6-\delta}$[86] and the layered $Sr_2Nb_2O_{7.2}$.[87] zT values of up to 2.4 were reported for oxide superlattices, estimated for the conducting layer in a $SrTiO_3/SrTiO_3$:Nb superlattice.[23]

The crystal structure may have large effects on the electronic band structure and the thermopower, as demonstrated by small distortions of the TiO_6 octahedra in the $SrO(SrTiO_3)_n$ Ruddlesden–Popper phases that dominate the Seebeck coefficient.[23] Here, a symmetry-induced crystal field splitting breaks the spin-orbital degeneracy of the titanium t_{2g} orbitals at the bottom of the conduction band, which in turn leads to a decrease of the density of states and a concomitant decrease of both the effective mass $m*$ and the Seebeck coefficient S. Even a slight structural distortion can induce a dramatic change of the Seebeck coefficient and a resulting zT value of 0.14 for $SrO(SrTiO_3)_2$ with niobium doping and distorted octahedra. In contrast, the structural distortion from doping with lanthanides is small and zT reaches a value of 0.24. Furthermore, thermal expansion slightly decreases the octahedra's distortions, thus improving the Seebeck coefficient at higher temperatures. A comparable case is represented by cubic spinel structure $LiMn_2O_4$, where the absence of the Jahn-Teller distorted MnO_6 octahedra lead to a thermopower three times higher.[88] This result is due to the increase of the degeneracy ratio of the ion pair involved in the polaron conduction (Mn^{3+} and Mn^{4+}). Nevertheless, the too high values of electrical resistivity neutralize the positive effect on the Seebeck generating a PF of ca. 10^{-6} $Wm^{-1}K^{-2}$.

A key advantage of layered oxides is their unusually low thermal conductivity normal to the layers and, in some cases, parallel to the layers. Therefore, highly textured polycrystalline specimens of the ferroelectric Aurivillius phase $Bi_4Ti_3O_{12}$ and the homologous series $Sr_2Nb_2O_7$ ($Sr_nNb_nO_{3n+2}$) have nearly constant low thermal conductivities of ≈ 1 $Wm^{-1}K^{-1}$ up to 1000°C across the layers. The in-plane thermal conductivity values of 1.5–2 $Wm^{-1}K^{-1}$ are also low and invariant with temperature, but distinctly bigger[89,90] than the cross-plane values.[17,91] This unusual temperature independence raises new questions about the thermal transport mechanisms in complex structures.[92] When phonon scattering from defects is considered and the mean free path is estimated on the order of the interatomic spacing, the anisotropy in thermal conductivity must have been caused by phonon scattering as a result of the acoustic

mismatch between layers with substantially different density and thickness.[93] Although the 2D structure of layered oxides can be exploited to decrease the thermal conductivity in an anisotropic fashion, the electrical performance along the temperature gradient is important as well. The design of nano- and micro-structures requires an understanding of the anisotropy in the electrical and thermal properties.

1.3.4 Zinc Oxides

ZnO is considered as a cheap, abundant, and promising high temperature thermoelectric material. Pure ZnO shows at room temperature a power factor of ≈ 800 Wm^{-1}K^{-2}, but also a relatively large thermal conductivity ($\kappa \approx 40$ Wm^{-1}K^{-1}), which reduces at higher temperatures to ≈ 5 Wm^{-1}K^{-1} (at 1000 K). This has been attributed to increased phonon scattering due a large and anisotropic thermal expansion.[94] Although it is possible to reach κ values of 2-3 Wm^{-1}K^{-1} at room temperature for nanograined ZnO,[95] it still maintains a low electrical conductivity σ. Therefore, zT does not improve. Defects at grain boundaries are major contributors to the low electrical conductivity.[96]

Nanostructuring for both, undoped and doped ZnO reduces the thermal conductivity.[97,98] Many reports appeared on pure and doped polycrystalline ZnO[99–110] in particular on nanostructures,[109,110] which results in a significant increase in the thermopower S. The zT values of doped and co-doped ZnO can reach values up to 0.65, making ZnO a viable candidate for a variety of thermoelectric applications."

1.4 Strategies to tune the TE properties

1.4.1 Tailoring the thermal conductivity

"A challenge for the materials scientist is to translate existing physical concepts into real chemical compounds. A good starting point is to estimate the strength of the chemical bonds between the atoms of the material under consideration. From Equation (10) can be seen as a strong bond (i.e., a large force constant) corresponds to a high lattice thermal conductivity. A textbook example is the 3D network of carbon atoms in diamond or an ionic solid with a highly symmetric 3D structure and large lattice energy (e.g., MgO). Large coordination numbers and bond distances are indicators for weak bonding and low thermal lattice conductivities. Therefore, the heat conductivity of solids with low dimensional structures like cobaltites[21,36,37,39–45] and oxyselenides[46,48,111,112] (Figure 1.6) is low. In addition, framework structures containing large voids filled with heavy atoms are candidates for low lattice thermal conductivities. Prominent examples are the Sb_2^{4-} dumbbells in Zn_4Sb_3,[113–118] the filled skutterudites such as $A_yCo_4Sb_{12}$[119–125] (being "A" the filler and "y" the degree of filling) and intermetallic clathrates.[126] All three materials exhibit remarkable low lattice thermal conductivities down to 0.5 $Wm^{-1}K^{-1}$ and 1.4 $Wm^{-1}K^{-1}$. The complex open structure of skutterudites allows interstitial atoms to be placed into a 20-atom "oversized" cage of the structure, consisting of covalently linked metal and p-element atoms with low charge, as determined by electron density studies.[123–125] The guest atom exhibits low-energy thermal vibrations, which lowers the lattice thermal conductivity.[127] Another approach to decrease the thermal conductivity is the formation of additional scattering centers such as grain boundaries on different length scales. In particular, grain boundaries on the nanoscale have been shown to reduce the lattice thermal conductivity efficiently.
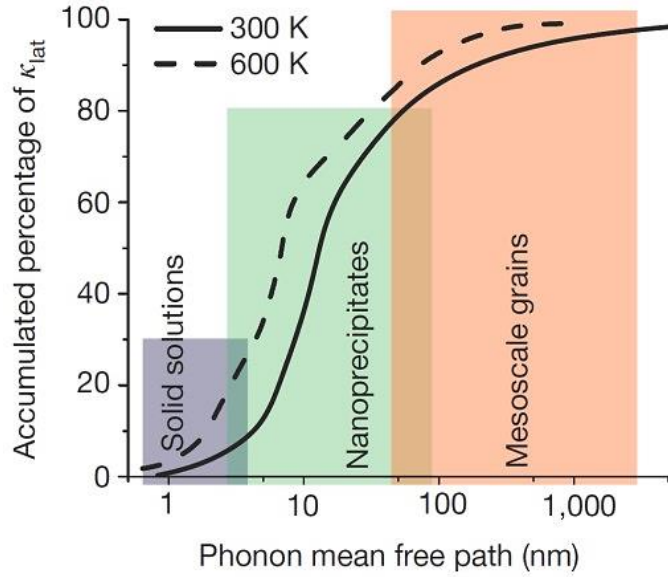
Figure 1.7: Percentage contribution to thermal conductivity from the lattice part of the thermal conductivity as a function of the phonon mean free path for PbTe. In a material with microscale crystallites more than 80% of the heat is carried by acoustic phonons. This is in agreement with the dominant phonon approximation. Figure adapted and modified from reference.[128]

This is in agreement with calculations that exhibit, for example in PbTe at 300 K, more than the 80% of κ_L is contributed by phonons with mean free paths < 100 nm.[128,129] A promising approach to reach thermal conductivities close to the amorphous limit is to introduce scattering centers on different length scales.[130–132] Still, the use of nanoparticular materials for thermoelectric application seems counterintuitive. Nanoparticles do not represent the thermodynamic equilibrium and tend to coalesce at high temperatures.[133,134] Thus the cycling behavior needs to be investigated to ensure long term stability of a material. Another approach to further reduce the mean free path is phonon scattering due to defects. The impact depends upon the mass difference (mass field fluctuations) and differences of the atomic radii (strain field fluctuations) of the defects and was demonstrated for half-Heusler phases,[135] oxyselenides,[75] and oxides.[136] An example where many of the above mentioned concepts have been applied are multiply-filled skutterudites.[137,138] Here the lattice thermal conductivity is continuously reduced through the filling of carefully selected guest atoms. In summary, complex crystal structures with different types of bonding interactions lead to low thermal conductivities.[17] This has been not only demonstrated for filled skutterudites,[118–124,137,138] but also for Zintl compounds[139] like $Yb_{14}MnSb_{11}$,[140] zinc antimonides,[112–117] and

clathrates.[141,142] However, the impact on the electronic transport properties must be balanced at the same time. Therefore, a flexible structure motif is required which allows optimizing the materials properties for thermoelectric application.

1.4.2   Manipulation of the charge carrier density

Dresselhaus and coworkers[143,144] outlined the challenges and strategies to improve our understanding of carrier transport processes that is needed because of the complexities in determining the key effects in electron and phonon transport experimentally and theoretically. The incorporation of dopants and change of stoichiometry are widely employed for adjusting the thermoelectric properties of transition metal oxides. Still, the solubility limits may suppress extensive doping, and thermodynamically favored compounds may be formed, instead, at elevated temperature. Besides cation doping, anion doping can be achieved for oxides with nitrogen (fluorine) to remove (add) carriers. This would also have a beneficial impact on the thermal conductivity due to mass field fluctuations. It has been shown for perovskites that this can be achieved by heating the parent compounds with urea or Teflon.[145,146] Disorder may result from doping or changing the stoichiometry of metal oxides. These manipulations change the vibrational properties of the crystal and therefore affect also the thermal transport by introducing additional scattering sites for phonons.[11,147] Thus, the charge carrier concentration is affected by changing the composition of the target compounds, and it affects the thermal conductivity as well. Therefore, doping, compositing, and other processes altering the oxygen deficiency can be implemented to adapt the thermal conductivity.

1.4.3   Decoupling the optimization

In engineering transition metal oxides, it is desirable to decouple, as far as possible, the electronic and the thermal transport. This can be achieved by structuring, which relies for example on a periodic arrangement of segments with different electron and phonon transport characteristics. It leads to the formation of a complex material structure with distinct regions having individual functionalities. An ideal thermoelectric transition metal oxide would

comprise a high mobility semiconductor region interpenetrating a phonon scattering region with disordered structures (e.g., dopants and lack of stoichiometry) that leave the carrier mobility of the other region unaffected.[17] Solids containing natural superlattices can offer an independent control of transport properties, providing an excellent platform to engineer high performance thermoelectric materials. Na_xCoO_2 and $In_2O_3 - (ZnO)_k$ (k = 1, 2, . . ., 9)[148,149] are good textbook examples. A further case is represented by the so-called Magnéli phases, a homologous series of transition metal oxides with the general formula M_nO_{3n-2} (or M_nO_{3n-1}) detected by Magnéli many years ago.[150] They are derived from the MoO_3, ReO_3, and TiO_2 structure types, and their common structural components are MO_6 octahedra. Variations of these compounds, forming a whole family of structures, can be described in terms of ordered 1- or 2-D crystallographic shears (CS), whose occurrence results as a consequence of a systematic elimination of oxygen atoms from the basic structures. Disordered occurrence of the CS planes in host structures is one of the principal sources of structural complexity. Crystallographic shear occurs in a particular crystallographic orientation. The preference may be explained by a different degree of distortion along the principal axes of the parent compounds. Shear planes reduce the thermal conductivity and allow approaching the problem of separating electronic and thermal scattering from a new direction: starting with a material that has a comparably low thermal conductivity, and then attempting to increase its power factor by adjusting the metal oxidation state.[151]

1.5 Metal oxides with adaptive structures

In the 1950s a homologous series of reduced early titanium oxides,[152,153] the so-called Magnéli phases, has been discovered, but only recently it came into the focus of thermoelectric research.[154–160] Structurally related to Ruddlesden–Popper phases through the ReO_3 parent structure, they attracted attention during the 1990s due to the occurrence of charge density waves in the low temperature regime.[161,162] In the context of thermoelectric research, Magnéli oxides of titanium fulfill several requirements for good thermoelectrics. Within a homologous series, e.g. Ti_nO_{2n-1} ($4 \leq n \leq 11$),[163–166] a slight oxygen deficiency is responsible for the formation of crystallographic shear (CS) planes which have been identified as effective phonon scattering centers. The concept underlying the use of Magnéli phases is based on the intrinsic, layered nanostructure defined by CS planes as structure motifs. As previously said, this allows reducing the thermal conductivity through CS in a first step, thereby starting with a material with a low thermal conductivity, and then increasing its power factor by adjusting the carrier concentration by changing the oxidation state of the metal.[151]

An architecture similar to that of the Magnéli oxides can be found in a series of tetragonal tungsten bronze (TTB) compounds such as $Nb_{8-x}W_{9+x}O_{47}$[167–170] and related W–Nb–O systems.[171,172] These compounds are structurally related to the Magnéli phases, and they show the peculiarity of changing the cation composition, hence the charge carrier concentration, without substantial structural variations. In the last years high power factors have been demonstrated for the niobium bronze $Sr_xBa_{1-x}Nb_2O_{6-\delta}$[86] and also for the TTB series which, due to its intrinsic architecture, might reveal interesting properties for thermoelectric applications. This section highlights the structural features of the Magnéli phases and relates them to their thermoelectric properties, also summarizing recent results on their high temperature thermoelectric properties.

1.5.1 The intrinsic nature of the CS planes

Before Magnéli reported the first type of homologous series in early transition metal oxides in the 1950s[173], compounds like $TiO_{1.90}$, $MoO_{2.75}$, and $WO_{2.90}$ were believed to be nonstoichiometric compositions with a wide homogeneity range. Since then, electron imaging and diffraction techniques confirmed the proposed structural concept, and many different homologous series including non-equilibrium structures were discovered.[174–177]
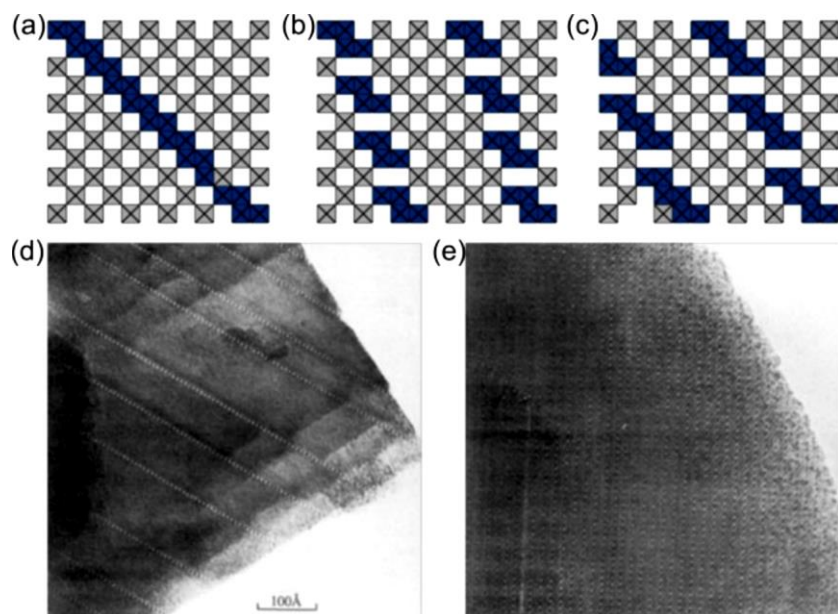
Figure 1.8: Idealized arrangements of crystallographic shear planes in WO_{3-x} projected along [010]. In the figure are shown crystallographic shear planes upon {001} (a), {102} (b), and {103} (c), and real space electron microscopy micrographs of highly disordered CS planes in WO_{3-x} (d) and $WO_{2.90}$ (e). In the homologous series W_nO_{3n-2} a higher degree of reduction is realized by CS that lie upon {103} planes. The orientation of the shear plane is termed according to the orientation of the shear with respect to the parent ReO_3-like structure of WO_3. (a–c) Image adapted and modified from.[178]

When early transition metal oxides such as TiO_2, V_2O_5, MoO_3, and WO_3 are partially reduced, either with the corresponding metal or with gaseous H_2, the reduction is accompanied by the formation of crystallographic shear planes. Within the crystal structure, the coordination of the cations remains essentially unchanged, but the anion coordination number increases to accommodate the lower metal to oxygen ratio. In the simplest case of a ReO_3-like parent structure (WO_3 and MoO_3) the reduction leads to the formation of planes where the octahedra

are edge- rather than corner-shared.[173] Such planes have been dubbed crystallographic shear (CS) planes (Figure 1.8). The term was introduced by Wadsley[165] to describe the periodicity of the planar defects using a mathematical description. Isolated planar defects of this kind are therefore named Wadsley defects.

In titanium oxides the derived edge-sharing rutile structure is replaced, along some crystallographic planes, by face-shearing octahedra. Thus, crystallographic shear planes appear whenever a type of linkage between two elements of a structure is changed along a specific crystallographic direction. In a simplified picture the formation steps of the CS planes can be viewed as follows: starting from a perfect crystal, oxygen vacancies are generated either by heating or chemical reduction. In early transition metal oxides, these vacancies normally emerge at the crystal surface and then diffuse to and accumulate at certain planes in the structure.[165,179] In the last step, these vacancies are then eliminated by the formation of corner/face sharing octahedra giving rise to crystallographic shear planes. Different mechanisms for the formation of CS planes have been proposed: (i) the migration of oxygen vacancies from the surface into the crystal and subsequent annihilation of vacancies by crystallographic shear; (ii) the formation of random anion vacancies and subsequent segregation in planar disks which tend to collapse under the formation of CS; (iii) a cooperative migration of cation–anion planes within the crystal where cation migration supports the rearrangement; (iv) cooperative migration of anions and cations, where only the tip of the area is able to move into the crystal, leaving a pair of CS planes behind; and (v) the formation of CS planes in the crystal and ordering of following CS planes due to strain field oscillations in the lattice. A common feature of all models is that oxygen vacancies are formed in the first step and the whole process can be interpreted as an assimilation of defects to incorporate them as new structural element. A similar ordering of vacant sites is observed in $Fe_{1-x}S$ and $Fe_{1-x}O$ compounds (Koch–Cohen clusters) where the reduction of Coulomb interactions is the driving force of the processes.[180–182] CS planes and related structural features have been found for many early transition metal oxides of titanium,[152,176,183] vanadium,[184–188] niobium,[189–192] molybdenum,[193–196] and tungsten.[173,197–200] In addition, a number of ternary and multinary oxides with CS planes are known.[201] Those oxides are formally insulators, such as PNb_9O_{25},[202] however, oxygen defects usually make them electrically conductive.

In contrast, the majority of the perovskite-based homologous series are anion-excessive. In the $A_{n+1}B_nO_{3n+1}$ Ruddlesden–Popper series, $A_nB_nO_{3n+1}$ Dion–Jacobson series, and $Bi_2A_{n-1}B_nO_{3n+3}$ Aurivillius series, the O/B ratio exceeds 3, because extra oxygen or metal-oxygen layers are added between the $\{001\}_p$-shaped perovskite blocks.[203–209] Another anion-excessive homologous series, $A_nB_nO_{3n+2}$, is based on $\{110\}_p$-shaped perovskite blocks separated by extra oxygen layers.[210,211]

In titanium oxides, starting from the rutile structure a homologues series of Ti_nO_{2n-1} ($4 \leq n \leq 9$) was identified with shear planes parallel to $\{1\text{-}21\}$.[174–176] The denotation of the CS planes follows the orientation of the shear plane with respect to the parent structure (Figure 1.8). The rutile-like substructure can still be identified between the shear planes. The separation between the shear planes increases with increasing "n" for all Magnéli compounds. For values of $n > 9$, a family with $\{13\text{-}2\}$ CS was determined by electron microscopy and selected area diffraction.[212] However, these $\{13\text{-}2\}_r$ phases always exhibit fine scale polysynthetic twinning and several members usually coexist in one crystal. The homologous series of vanadium oxides V_nO_{2n-1} ($3 \leq n \leq 9$) can also be derived from the rutile parent structure.[213] In contrast to the titanium oxides, a higher degree of reduction only increases the number of shared edges of the octahedra. For example, the structure of V_6O_{13} can be derived from the layered V_2O_5 by removing every third oxygen layer parallel to the $\{010\}$ plane and a following rearrangement. In case of the tungsten and molybdenum oxides, the corresponding Magnéli phases are derived from the ReO_3 parent structure by shear. Similar to the titanium oxides a homologous series of Mo_nO_{3n-1} can be defined for molybdenum with $n = 8, 9, 10$. In addition there are the compounds Mo_4O_{11} and $Mo_{17}O_{47}$ which have been widely studied because of their temperature driven charge density wave (CDW) transition to an incommensurate state at low temperatures.[214] The higher members of the homologous series also indicate a CDW-driven phase transition.[215] In the quasi-binary system WO_3 - WO_2, the CS planes lie on the $\{102\}$ and $\{103\}$ planes. In the approximate composition of $WO_{2.96} - WO_{2.933}$ a series with the formula W_nO_{3n-1} was identified.[197,199] For a higher degree of reduction, starting from $WO_{2.92}$, the CS is situated on the $\{103\}$ planes. Although the CS planes are relatively well ordered, an equidistant spacing is barely found. The series formula for compounds with $\{103\}$ is W_nO_{3n-2}, with values of n between 18 and 25 ($WO_{2.92}$ - $WO_{2.885}$). Figure 1.8a shows a scheme of the idealized CS $\{102\}$ and $\{103\}$ planes in the WO_3 - WO_2 system.

In contrast to the oxides discussed above, the family of niobium oxides shows two sets of non-collinear CS planes leading to the well-known block structures of binary and ternary niobium oxides. The structures can be derived from the ReO_3 as parent structure by CS on {100} and {010} planes. Compounds such as $Nb_{12}O_{29}$ and $Nb_{25}O_{62}$ were identified and thermodynamically investigated in the late 1960s.[190,216–222] In order to overview the structural features more easily, a short notation of the form $(m \times n)_p$ was introduced by Wadsley which represents the block character of the compounds.[165] The subscripts m and n designate the size of a block m by n corner-sharing octahedra. The variable p can adopt values of 1 (isolated blocks), 2 (blocks joined pairwise by edge-sharing), and infinity (formation of infinite strips or sheets). Assuming total homogeneity, the composition of the compounds is related to the block structure by the general formula $M_{mnp+1}O_{3mnp-(m+n)p+4}$. A more detailed discussion of the building principle of the different block-structures and existing phases is given elsewhere.[201,223]

Many of the Magnéli phases are metallic or semimetallic. The formation of CS goes along with a reduction of the metal atoms. The electrons occupy the metal d-bands and lead to n-type conduction.[223] In order to understand the electronic structure in more detail, the nature of the partially filled d-bands needs to be considered. In their seminal work Whangbo and Canadell[161] developed a very powerful semi empirical approach that allows an understanding and prediction of the electronic structure of these metal oxides.

The structure of many ternary compounds of early transition metal oxides show CS planes. This underlines the tendency of different transition metals to adopt an octahedral coordination. The TTBs $Nb_{8-x}W_{9+x}O_{47}$ are an illustrative example. The structure of this series with x ranging from 0 to 5 was studied by Krumeich et al.[167] The structure of the ternary oxides adopting the TTB structure in both the Nb-rich and W-rich regions shows a close relation to the ReO_3 type by forming a 3D superstructure with corner-sharing octahedra forming pentagonal tunnels. Some of these pentagonal tunnels are filled with metal and oxygen atoms which give rise to pentagonal bipyramids. Assuming the oxygen content of the lattice to be constant, the replacement of Nb^{5+} by W^{6+} (from $x = 0$ to $x = 5$) formally leads to a reduction and a concomitant occupation of the lower portion of the metal d-band. The change of the charge carrier concentration can be accomplished by substitution: the number of available electrons (TTBs are also n-type materials) increases with increasing degree of substitution. Due to the

large unit cell and to the presence of both, ordered CS planes and disordered grains of different size, the thermal conductivity of the TTBs is relatively low.[224] This intrinsically low thermal conductivity of the TTBs in combination with their adaptability, makes them interesting as *n*-type thermoelectric. The control of the oxygen content and the formation of oxygen vacancies, similarly to the mixed valent Magnéli phases, might open an additional path to tune the electronic properties of the TTBs.

1.5.2 Thermoelectric properties

Metal oxides with adaptive structures like the Magnéli phases fulfill many of the requirements for thermoelectric materials. A combination of an intrinsically low thermal conductivity and the possibility to tune the electronic transport properties by controlled oxygen reduction and cation substitution has sparked the interest in these materials. The CS planes and the natural disorder can be interpreted as intrinsic nanostructures. In contrast to crystalline interfaces, CS planes are stable at high temperature, i.e. they survive long-term high temperature application/cycling. Although modeling of the electronic structure is difficult because of the large unit cell and disorder, the degree of reduction in the homologous series allows the targeted manipulation and optimization of the electronic transport properties. So far, only a limited number of studies on the high temperature thermoelectric properties of Magnéli oxides of titanium and related composites are available.[154–160,212,225–227] This group of chemically inert and physically stable compounds show a big potential and may close the gap between *n*-type and *p*-type oxide materials.

Tsuyomoto et al.[228] demonstrated that TiO_x (x = 1.94; Ti_8O_{15}) exhibits a Seebeck coefficient S of -518 μVk^{-1} and σ of 2 x 10^3 Sm^{-1} at 350 K. They demonstrated that both S and σ increase with temperature, resulting in a thermoelectric power factor of 540 $\mu Wm^{-1}K^{-2}$ at 343 K. Single crystal rutile TiO_2 reduced to TiO_{2-x} by heating under hydrogen at 1050 K shows high *PF* at low cryogenic temperatures. The thermal conductivity of TiO_{2-x} is low (0.83 $Wm^{-1}K^{-1}$) due to enhanced phonon scattering by the defect planes. The Seebeck coefficient of TiO_{2-x} can be as large as 6 x 10^4 μVK^{-1}, leading to a *zT* of 0.1 at 10 K.[229]

Another study showed that non-stoichiometric TiO_{2-x} (derived from Rutile), formed after annealing and reduction with carbon at 1373 K, has a power factor of 100 $\mu Wm^{-1}K^{-2}$ up to 550

K.[225] The formation of oxygen vacancies in TiO2 leads to enhanced electrical conductivity due to an increased carrier concentration. Although TiO_2 is a classical-type wide band semiconductor, conduction is reported for slightly reduced TiO_2. Calculations using Heikes formula suggests temperature activated polaron conduction, at least in the high temperature regime.[230] In combination with a thermal conductivity as low as 2 - 3 $Wm^{-1}K^{-1}$, zT of 0.13 could be achieved at 800 K. Calculations of the charge carrier mobility as a function of the reduction suggests that crystallographic shear planes are effective scattering centers for phonons without disrupting the electronic transport properties. This underlines the role of the CS planes. TiO_2 nanoparticles doped with Nb on the metal position and N on the oxygen site, show so far the best performance of Magnéli oxides and related systems.[231] Although these nanoparticles do not belong strictly to the Magnéli phases, defects and metal cations with different valances may induce the formation of Wadsley defects.

Tungsten-based Magnéli phases show similar properties as the titanium-based compounds, but the thermal stability range is shifted by about 300 K to higher temperature.[232–235] Spark plasma sintered (SPS) samples of $WO_{2.90}$ and $WO_{2.722}$ exhibit crystallographic shear planes as typical feature of the crystal structures of Magnéli-type metal oxides, which leads to a remarkably low thermal conductivity for $WO_{2.90}$. The figures of merit ($zT = 0.13$ at 1100 K for $WO_{2.90}$ and 0.07 at 1100 K for $WO_{2.722}$) are relatively high for binary tungsten oxides and metal oxides in general. The $WO_{2.722}$ shows metallic behavior with temperature, while $WO_{2.90}$ has the characteristics of a heavily doped semiconductor. The low thermopower of 80 μVK^{-1} at 1100 K for $WO_{2.90}$ is attributed to its high charge carrier concentration. The enhanced thermoelectric performance for $WO_{2.90}$ compared to $WO_{2.722}$ originates from its much lower thermal conductivity, due to the presence of crystallographic shear and dislocations in the crystal structure. This demonstrates that intrinsically nanostructured materials rather than artificially structured layered systems can substantially reduce the lattice thermal conductivity.

Among the ternary compounds, the TTB-type $Nb_{8-x}W_{9+x}O_{47-\delta}$ have been studied and the thermoelectric properties of such transition metal oxides with complex structures have been assessed.[224] The structure is complex and allows electronic tuning by cation substitution x and oxygen deficiency δ. A series of compounds with substitution degrees $x = 0, 0.075, 0.1, 1, 2, 3,$ and 4 were investigated. HR-TEM studies revealed varying grain sizes down to few nanometers and a variety of different oxygen defects, including point defects, Wadsley defects

and crystallographic shear planes. The oxygen deficiency can be reversibly controlled by equilibrating the sample in a controlled atmosphere at 1173 K. Due to the reversible generation and annihilation of oxygen vacancies at elevated temperatures, the electronic properties can be tuned to some extent. A maximum oxygen deficiency of $\delta = 0.3$ was determined for $Nb_8W_9O_{47-\delta}$. Each oxygen vacancy acts as a donor of two electrons to the system, so that the maximum oxygen deficiency of 0.3 corresponds to a change in substitution degree of $x = 0.6$. The lowest substituted samples exhibited a relatively high electric resistivity (above 20 mΩcm) and high negative Seebeck coefficients ranging from -280 to -65 µV/K, indicating n-type conduction. With increasing degree of substitution, the number of charge carriers was increased, which in turn leads to a drastic reduction of the electric resistivity (≈ 3 mΩ·cm for the sample with $x = 4$) and a decrease of the thermopowers. The complex structure composed of nano-sized grains, and a high concentration of Wadsley defects and crystallographic shear planes results in glass-like values of the thermal conductivity, ranging from 1 to 2.5 $Wm^{-1}K^{-1}$. The highest figure of merit zT was obtained for the highest substituted sample ($Nb_4W_{13}O_{47}$) with a value of ≈ 0.2 at 1173 K. Although the obtained figure of merit is lower than in other optimized n-type oxides, the highest substituted samples of this series demonstrates a good potential for thermoelectric applications.
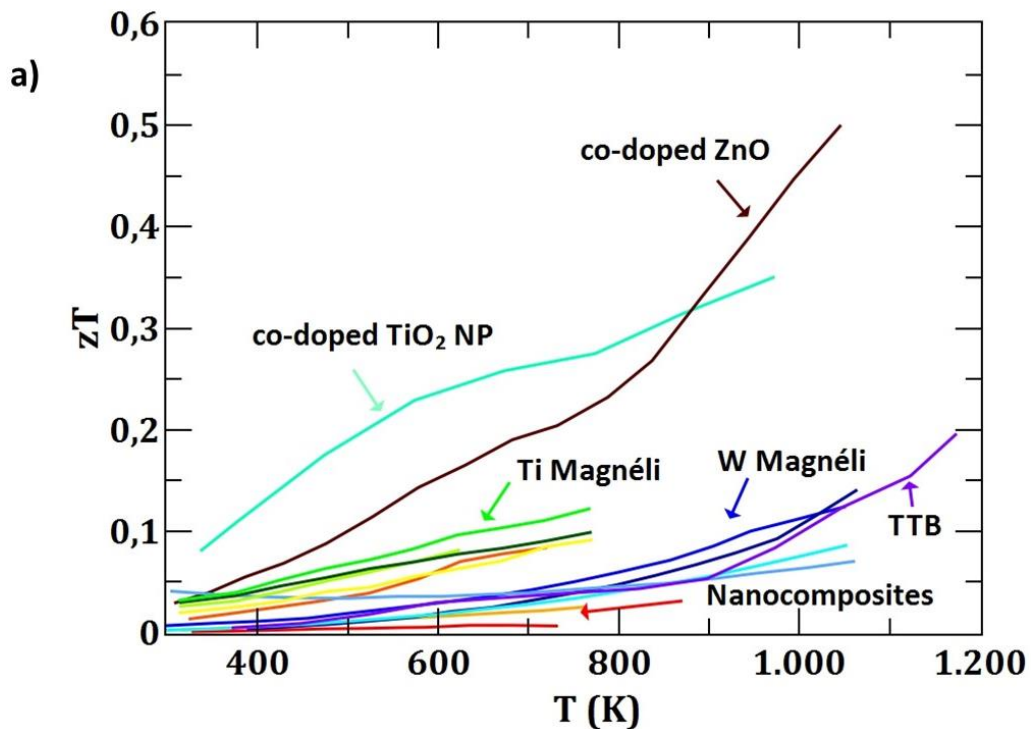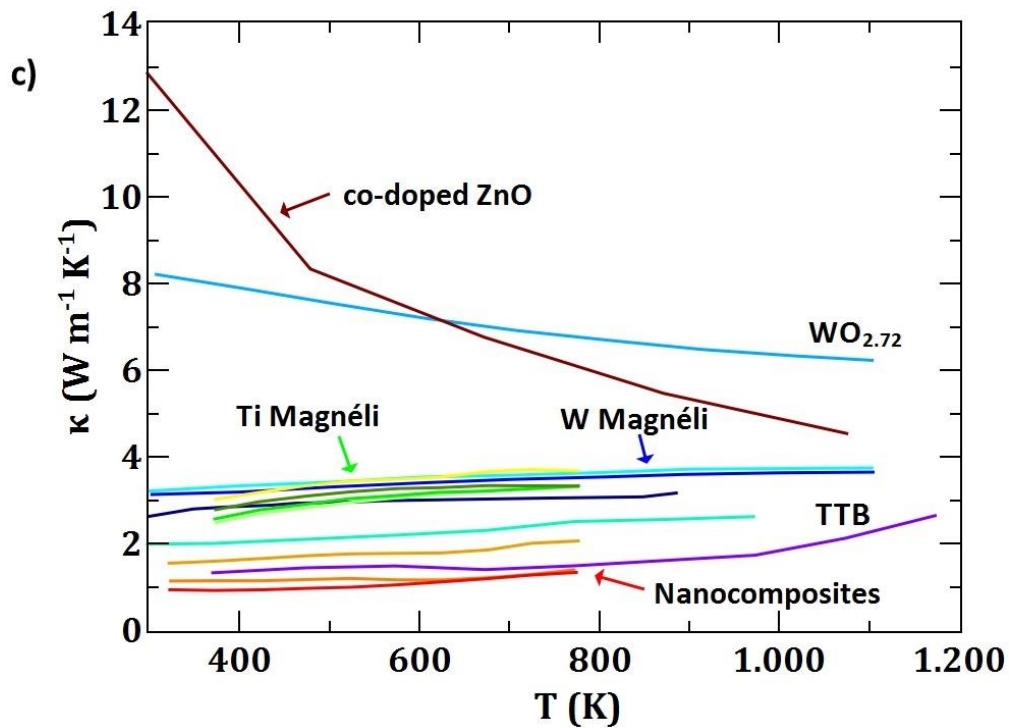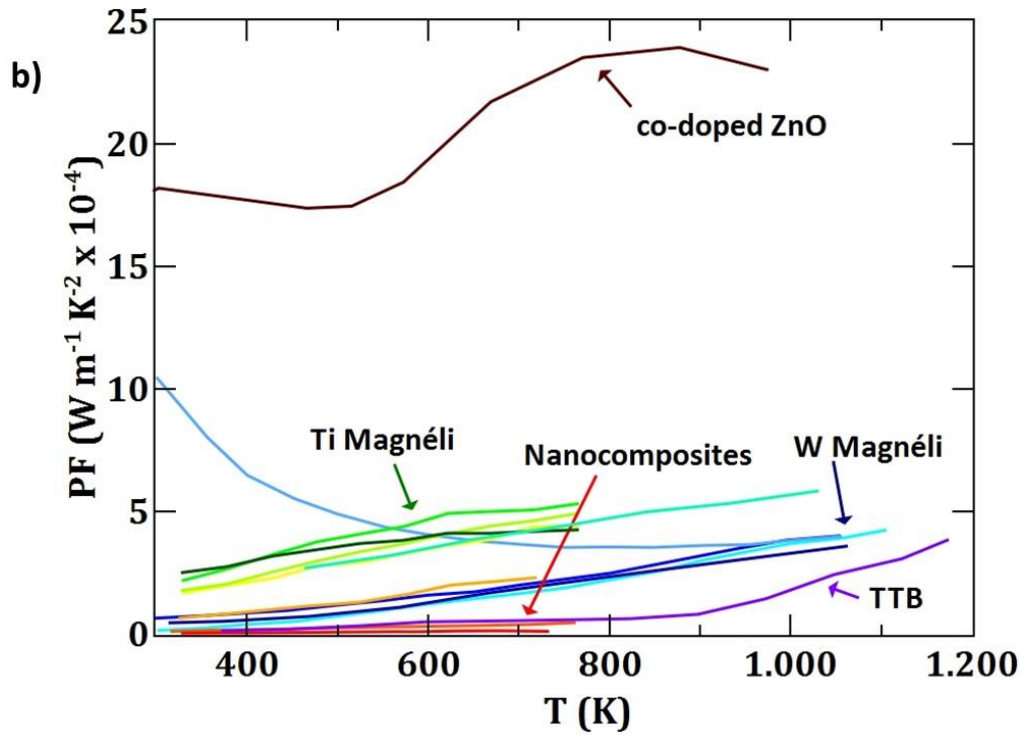
Figure 1.9: Comparison of *zT* values (a), temperature dependent power factors *PF* (b), and thermal conductivities κ (c) of different Magnéli phases and Al, Ga doped ZnO as reference. Titanium oxides are the best characterized Magnéli phases. The values for titanium oxides (green-scale colors), titanium oxide composite systems (light blue and red-scale colors), tungsten oxides (blue-scale colors), and the tetragonal tungsten bronze $Nb_6W_{11}O_{47}$ (violet) were adapted from the literature.

In summary, oxides with adaptive structures are interesting candidates for thermoelectric applications because of (i) their intrinsic low thermal conductivity, (ii) metallic electrical conductivity, and (iii) the possibility of tuning the charge carrier concentration. Although Magnéli phases and structurally related oxides are a relatively new class in the context of thermoelectric materials, they show promising properties and still have options for further optimization. Early transition metal oxides fulfill the sustainability requirements for new materials and can clearly help to tackle the upcoming challenges in the energy sector. Indeed, transition metal oxides are interesting for commercial applications where cheap, benign, and robust materials are required. The preparation of the powders usually involves standard solid state techniques. In addition, fast and facile SPS-assisted preparation of phase pure compounds is possible. Although some intrinsic properties of oxides are not completely matching the guideline for good thermoelectric materials (among all low zT values), the low producing costs and their high thermal and physical stability make them highly interesting candidates."

References

[1]   G. Kieslich, G. Cerretti, I. Veremchuk, R. P. Hermann, M. Panthöfer, J. Grin, W. Tremel, *Phys. Status Solidi* **2016**, *213*, 808–823.

[2]   A. Luque, S. Hegedus, *Handbook of Photovoltaic Science and Engineering*, Wiley, **2003**.

[3]   M. A. Green, K. Emery, Y. Hishikawa, W. Warta, E. D. Dunlop, *Prog. Photovolt Res. Appl.* **2016**, *24*, 3–11.

[4]   R. M. Swanson, *Science* **2009**, *324*, 891–892.

[5]   K. S. Joya, Y. F. Joya, K. Ocakoglu, R. Van De Krol, *Angew. Chem. Int. Ed.* **2013**, *52*, 10426–10437.

[6]   L. Zhang, E. Reisner, J. J. Baumberg, *Ener. Environ. Sci.* **2014**, *7*, 1402.

[7]   J. B. Goodenough, K. S. Park, *J. Am. Chem. Soc.* **2013**, *135*, 1167–1176.

[8]   M. N. Tahir, B. Oschmann, D. Buchholz, X. Dou, I. Lieberwirth, M. Panthöfer, W. Tremel, R. Zentel, S. Passerini, *Adv. Ener. Mater.* **2016**, *6*, 1–9.

[9]   N. S. Choi, Z. Chen, S. A. Freunberger, X. Ji, Y. K. Sun, K. Amine, G. Yushin, L. F. Nazar, J. Cho, P. G. Bruce, *Angew. Chem. Int. Ed.* **2012**, *51*, 9994–10024.

[10]   L. E. Bell, *Science* **2008**, *321*, 1457–1461.

[11]   J. R. Sootsman, D. Y. Chung, M. G. Kanatzidis, *Angew. Chem. Int. Ed.* **2009**, *48*, 8616–8639.

[12]   V. Andrei, K. Bethke, K. Rademann, *Ener. Environ. Sci.* **2016**, *9*, 1528–1532.

[13]   V. Mireles, J. W. Stultz, in *SAE Tech. Pap.*, **1994**, p. 941269.

[14]   Alphabet Energy, "Fuel Efficiency vs. Electrification: The Race Is On," can be found under https://www.alphabetenergy.com/, **2016**.

[15]   T. J. Seebeck, *Ann. Phys.* **1826**, *82*, 133–160.

[16]   W. Thomson, *R. Soc. Edinburgh Earth Sci.* **1851**, *3*, 91–98.

[17]   G. J. Snyder, E. S. Toberer, *Nat. Mater.* **2008**, *7*, 105–114.

[18]   G. A. Slack, *CRC Handbook of Thermoelectrics*, CRC Press, **1995**.

[19]   G. Kieslich, Thermoelectric Properties of Nanostructured and Naparticular Compounds, Johannes Gutenberg Universität Mainz, **2013**.

[20]   W. G. Zeier, A. Zevalkink, Z. M. Gibbs, G. Hautier, M. G. Kanatzidis, G. J. Snyder, *Angew. Chem. Int. Ed.* **2016**, *55*, 6826–6841.

[21]   G. D. Mahan, J. O. Sofo, *Proc. Natl. Acad. Sci. U. S. A.* **1996**, *93*, 7436–7439.

[22]   I. Terasaki, Y. Sasago, K. Uchinokura, *Phys. Rev. B* **1997**, *56*, R12685–R12687.

[23]   K. Koumoto, Y. Wang, R. Zhang, A. Kosuga, R. Funahashi, *Annu. Rev. Mater. Res.* **2010**, *40*, 363–394.

[24]   M. Jonson, G. D. Mahan, *Phys. Rev. B* **1980**, *21*, 4223–4229.

[25]   C. Dames, G. Chen, *Thermoelectrics Handbook: Macro to Nano*, CRC Press, **2006**.

[26]   J. Yang, in *Therm. Conduct. Theory, Prop. Appl.* (Ed.: T.M. Tritt), Springer US, New York, **2004**.

[27]   E. S. Toberer, A. Zevalkink, G. J. Snyder, *J. Mater. Chem.* **2011**, *21*, 15843–15852.

[28]   O. Delaire, J. Ma, K. Marty, F. May, M. McGuire, M.-H. Du, D. J. Singh, A. Podlesnyak, G. Ehlers, M. D. Lumsden, et al., *Nat. Mater.* **2011**, *10*, 614–619.

[29]   J. Leitner, P. Voňka, D. Sedmidubský, P. Svoboda, *Thermochim. Acta* **2010**, *497*, 7–13.

[30]   J. Brgoch, S. P. DenBaars, R. Seshadri, *J. Phys. Chem. C* **2013**, *117*, 17955–17959.

[31]   M. W. Gaultois, T. D. Sparks, C. K. H. Borg, R. Seshadri, W. D. Bonificio, D. R. Clarke, *Chem. Mater.* **2013**, *25*, 2911–2920.

[32]   P. A. Cox, *The Electronic Structure and Chemistry of Solids*, Oxford University Press,

New York, **1987**.

[33] A. Shakouri, *Annu. Rev. Mater. Res.* **2011**, *41*, 399–431.

[34] N. Tsuda, K. Nasu, A. Fujimori, K. Siratori, *Electronic Conduction in Oxides*, Springer Berlin Heidelberg, Berlin, Heidelberg, **2000**.

[35] Y. Tokura, *Science* **2000**, *288*, 462–468.

[36] P. Limelette, S. Hébert, V. Hardy, R. Frésard, C. Simon, A. Maignan, *Phys. Rev. Lett.* **2006**, *97*, 46601.

[37] M. Lee, L. Viciu, L. Li, Y. Wang, M. L. Foo, S. Watauchi, R. a Pascal, R. J. Cava, N. P. Ong, *Nat. Mater.* **2006**, *5*, 537–540.

[38] S. Walia, R. Weber, S. Balendhran, D. Yao, J. T. Abrahamson, S. Zhuiykov, M. Bhaskaran, S. Sriram, M. S. Strano, K. Kalantar-zadeh, *Chem. Commun.* **2012**, *48*, 7462–7464.

[39] Y. Wang, N. S. Rogado, R. J. Cava, N. P. Ong, *Nature* **2003**, *423*, 425–428.

[40] M. L. Foo, Y. Wang, S. Watauchi, H. W. Zandbergen, T. He, R. J. Cava, N. P. Ong, *Phys. Rev. Lett.* **2004**, *92*, 247001.

[41] Q. Huang, M. L. Foo, R. A. Pascal, J. W. Lynn, B. H. Toby, T. He, H. W. Zandbergen, R. J. Cava, *Phys. Rev. B* **2004**, *70*, 184110.

[42] J. Sugiyama, J. H. Brewer, E. J. Ansaldo, H. Itahara, T. Tani, M. Mikami, Y. Mori, T. Sasaki, S. Hébert, A. Maignan, *Phys. Rev. Lett.* **2004**, *92*, 17602.

[43] G. Lang, J. Bobroff, H. Alloul, P. Mendels, N. Blanchard, G. Collin, *Phys. Rev. B* **2005**, *72*, 94404.

[44] C. de Vaulx, M.-H. Julien, C. Berthier, M. Horvatić, P. Bordet, V. Simonet, D. P. Chen, C. T. Lin, *Phys. Rev. Lett.* **2005**, *95*, 186405.

[45] J.-Y. Kim, J.-I. Kim, S.-M. Choi, Y. Soo Lim, W.-S. Seo, H. Jin Hwang, *J. Appl. Phys.* **2012**, *112*, 113705.

[46] P. Ruleova, C. Drasar, P. Lostak, C.-P. Li, S. Ballikaya, C. Uher, *Mater. Chem. Phys.*

2010, *119*, 299–302.

[47]   J.-L. Lan, Y.-C. Liu, B. Zhan, Y.-H. Lin, B. Zhang, X. Yuan, W. Zhang, W. Xu, C.-W. Nan, *Adv. Mater.* **2013**, *25*, 5086–5090.

[48]   J. Sui, J. Li, J. He, Y.-L. Pei, D. Berardan, H. Wu, N. Dragoe, W. Cai, L.-D. Zhao, *Energy Environ. Sci.* **2013**, *6*, 2916–2920.

[49]   Y.-L. Pei, H. Wu, D. Wu, F. Zheng, J. He, *J. Am. Chem. Soc.* **2014**, *136*, 13902–13908.

[50]   R. R. Heikes, R. W. Ure, *Thermoelectricity. Science and Engineering*, Interscience Publisher, New York, **1961**.

[51]   W. Koshibae, K. Tsutsui, S. Maekawa, *Phys. Rev. B - Condens. Matter Mater. Phys.* **2000**, *62*, 6869–6872.

[52]   J. Androulakis, P. Migiakis, J. Giapintzakis, *Appl. Phys. Lett.* **2004**, *84*, 1099.

[53]   S. Okada, I. Terasaki, *Jpn. J. Appl. Phys.* **2005**, *44*, 1834–1837.

[54]   Y. Klein, S. Hébert, A. Maignan, S. Kolesnik, T. Maxwell, B. Dabrowski, *Phys. Rev. B* **2006**, *73*, 52412.

[55]   M. Uchida, K. Oishi, M. Matsuo, W. Koshibae, Y. Onose, M. Mori, J. Fujioka, S. Miyasaka, S. Maekawa, Y. Tokura, *Phys. Rev. B - Condens. Matter Mater. Phys.* **2011**, *83*, 1–5.

[56]   W. Kobayashi, I. Terasaki, M. Mikami, R. Funahashi, T. Nomura, T. Katsufuji, *J. Appl. Phys.* **2004**, *95*, 6825–6827.

[57]   G. V. M. Williams, E. K. Hemery, D. McCann, *Phys. Rev. B - Condens. Matter Mater. Phys.* **2009**, *79*, 1–7.

[58]   A. A. Taskin, A. N. Lavrov, Y. Ando, *Phys. Rev. B* **2006**, *73*, 121101.

[59]   M. Karppinen, H. Fjellvåg, T. Konno, Y. Morita, T. Motohashi, H. Yamauchi, *Chem. Mater.* **2004**, *16*, 2790–2793.

[60]   K. Takahashi, A. Sakai, H. Adachi, T. Kanno, *J. Phys. D. Appl. Phys.* **2010**, *43*,

165403.

[61]   J. Liu, X. Huang, D. Yang, G. Xu, L. Chen, *Dalton Trans.* **2014**, *43*, 15414–15418.

[62]   T. Sun, H. H. Hng, Q. Yan, J. Ma, *J. Electron. Mater.* **2010**, *39*, 1611–1615.

[63]   M. Tahashi, T. Tanimoto, H. Goto, M. Takahashi, T. Idoz, *J. Am. Ceram. Soc.* **2010**, *93*, 3046–3048.

[64]   W. Tremel, R. Hoffmann, *J. Am. Chem. Soc.* **1987**, *109*, 124–140.

[65]   M. Palazzi, S. Jaulmes, *Acta Crystallogr. Sect. B Struct. Crystallogr. Cryst. Chem.* **1981**, *37*, 1337–1339.

[66]   Y. Takano, C. Ogawa, Y. Miyahara, H. Ozaki, K. Sekizawa, *J. Alloys Compd.* **1997**, *249*, 221–223.

[67]   P. S. Berdonosov, A. M. Kusainova, L. N. Kholodkovskaya, V. A. Dolgikh, L. G. Akselrud, B. A. Popovkin, *J. Solid State Chem.* **1995**, *118*, 74–77.

[68]   A. M. Kusainova, P. S. Berdonosov, L. G. Akselrud, L. N. Kholodkovskaya, V. A. Dolgikh, B. A. Popovkin, *J. Solid State Chem.* **1994**, *112*, 189–191.

[69]   K. Ueda, S. Inoue, S. Hirose, H. Kawazoe, H. Hosono, *Appl. Phys. Lett.* **2000**, *77*, 2701.

[70]   S. Inoue, K. Ueda, H. Hosono, N. Hamada, *Phys. Rev. B* **2001**, *64*, 245211.

[71]   H. Hiramatsu, K. Ueda, H. Ohta, T. Kamiya, M. Hirano, H. Hosono, *Appl. Phys. Lett.* **2005**, *87*, 211107.

[72]   L. Pinsard-Gaudart, D. Bérardan, J. Bobroff, N. Dragoe, *Phys. Status Solidi - Rapid Res. Lett.* **2008**, *2*, 185–187.

[73]   I. I. Mazin, M. D. Johannes, *Nat. Phys.* **2009**, *5*, 141–145.

[74]   J.-F. Li, W.-S. Liu, L.-D. Zhao, M. Zhou, *NPG Asia Mater.* **2010**, *2*, 152–158.

[75]   Y.-L. Pei, J. He, J.-F. Li, F. Li, Q. Liu, W. Pan, C. Barreteau, D. Berardan, N. Dragoe, L.-D. Zhao, *NPG Asia Mater.* **2013**, *5*, e47.

[76] J. Li, J. Sui, C. Barreteau, D. Berardan, N. Dragoe, W. Cai, Y. Pei, L.-D. Zhao, *J. Alloys Compd.* **2013**, *551*, 649–653.

[77] J. Li, J. Sui, Y. Pei, C. Barreteau, D. Berardan, N. Dragoe, W. Cai, J. He, L.-D. Zhao, *Ener. Environ. Sci.* **2012**, *5*, 8543.

[78] L. D. Zhao, D. Berardan, Y. L. Pei, C. Byl, L. Pinsard-Gaudart, N. Dragoe, *Appl. Phys. Lett.* **2010**, *97*, 92118.

[79] T. Suzuki, M. S. Bahramy, R. Arita, Y. Taguchi, Y. Tokura, *Phys. Rev. B* **2011**, *83*, 35204.

[80] L.-D. Zhao, J. He, D. Berardan, Y. Lin, J.-F. Li, C.-W. Nan, N. Dragoe, *Energy Environ. Sci.* **2014**, *7*, 2900.

[81] H. Ohta, K. Sugiura, K. Koumoto, *Inorg. Chem.* **2008**, *47*, 8429–8436.

[82] H. Ohta, *Mater. Today* **2007**, *10*, 44–49.

[83] T. Okuda, K. Nakanishi, S. Miyasaka, Y. Tokura, *Phys. Rev. B* **2001**, *63*, 113104.

[84] S. Ohta, T. Nomura, H. Ohta, K. Koumoto, *J. Appl. Phys.* **2005**, *97*, 34106.

[85] J. Ravichandran, W. Siemons, D.-W. Oh, J. T. Kardel, A. Chari, H. Heijmerikx, M. L. Scullin, A. Majumdar, R. Ramesh, D. G. Cahill, *Phys. Rev. B* **2010**, *82*, 165126.

[86] S. Lee, R. H. T. Wilke, S. Trolier-McKinstry, S. Zhang, C. A. Randall, *Appl. Phys. Lett.* **2010**, *96*, 31910.

[87] S. Lee, G. Yang, R. H. T. Wilke, S. Trolier-McKinstry, C. A. Randall, *Phys. Rev. B* **2009**, *79*, 134110.

[88] T. D. Sparks, A. Gurlo, D. R. Clarke, *J. Mater. Chem.* **2012**, *22*, 4631–4636.

[89] T. D. Sparks, P. A. Fuierer, D. R. Clarke, *J. Am. Ceram. Soc.* **2010**, *93*, 1136–1141.

[90] Y. Shen, D. R. Clarke, P. A. Fuierer, *Appl. Phys. Lett.* **2008**, *93*, 102907.

[91] C. J. Vineis, A. Shakouri, A. Majumdar, M. G. Kanatzidis, *Adv. Mater.* **2010**, *22*, 3970–3980.

[92]   C. Chiritescu, D. G. Cahill, N. Nguyen, D. Johnson, A. Bodapati, P. Keblinski, P. Zschack, *Science* **2007**, *315*, 351–353.

[93]   C. Wan, T. D. Sparks, P. Wei, D. R. Clarke, *J. Am. Ceram. Soc.* **2010**, *93*, 1457–1460.

[94]   K. P. Ong, D. J. Singh, P. Wu, *Phys. Rev. B* **2011**, *83*, 115110.

[95]   Y. Kinemuchi, M. Mikami, K. Kobayashi, K. Watari, Y. Hotta, *J. Electron. Mater.* **2010**, *39*, 2059–2063.

[96]   D. G. Cahill, R. O. Pohl, *Annu. Rev. Phys. Chem.* **1988**, *39*, 93–121.

[97]   P. Jood, R. J. Mehta, Y. Zhang, G. Peleckis, X. Wang, R. W. Siegel, T. Borca-Tasciuc, S. X. Dou, G. Ramanath, *Nano Lett.* **2011**, *11*, 4337–4342.

[98]   Y. Fujishiro, M. Miyata, M. Awano, K. Maeda, *J. Am. Ceram. Soc.* **2005**, *87*, 1890–1894.

[99]   H. Kaga, Y. Kinemuchi, H. Yilmaz, K. Watari, H. Nakano, H. Nakano, S. Tanaka, A. Makiya, Z. Kato, K. Uematsu, *Acta Mater.* **2007**, *55*, 4753–4757.

[100]   M. Ohtaki, K. Araki, K. Yamamoto, *J. Electron. Mater.* **2009**, *38*, 1234–1238.

[101]   J. P. Wiff, Y. Kinemuchi, H. Kaga, C. Ito, K. Watari, *J. Eur. Ceram. Soc.* **2009**, *29*, 1413–1418.

[102]   N. Ma, J.-F. Li, B. P. Zhang, Y. H. Lin, L. R. Ren, G. F. Chen, *J. Phys. Chem. Solids* **2010**, *71*, 1344–1349.

[103]   Y. Fujishiro, M. Miyata, M. Awano, K. Maeda, *J. Am. Ceram. Soc.* **2003**, *86*, 2063–2066.

[104]   K. H. Kim, S. H. Shim, K. B. Shim, K. Niihara, J. Hojo, *J. Am. Ceram. Soc.* **2005**, *88*, 628–632.

[105]   E. Guilmeau, A. Maignan, C. Martin, *J. Electron. Mater.* **2009**, *38*, 1104–1108.

[106]   H. Colder, E. Guilmeau, C. Harnois, S. Marinel, R. Retoux, E. Savary, *J. Eur. Ceram. Soc.* **2011**, *31*, 2957–2963.

[107] Y. Michiue, T. Mori, A. Prytuliak, Y. Matsushita, M. Tanaka, N. Kimizuka, *RSC Adv.* **2011**, *1*, 1788–1793.

[108] K.-H. Jung, K. Hyoung Lee, W.-S. Seo, S.-M. Choi, *Appl. Phys. Lett.* **2012**, *100*, 253902.

[109] L. Shi, J. Chen, G. Zhang, B. Li, *Phys. Lett. A* **2012**, *376*, 978–981.

[110] Y. Yang, K. C. Pradel, Q. Jing, J. M. Wu, F. Zhang, Y. Zhou, Y. Zhang, Z. L. Wang, *ACS Nano* **2012**, *6*, 6984–6989.

[111] J. Le Lan, Y. C. Liu, B. Zhan, Y. H. Lin, B. Zhang, X. Yuan, W. Zhang, W. Xu, C. W. Nan, *Adv. Mater.* **2013**, *25*, 5086–5090.

[112] Y. L. Pei, H. Wu, D. Wu, F. Zheng, J. He, *J. Am. Chem. Soc.* **2014**, *136*, 13902–13908.

[113] T. Caillat, J.-P. Fleurial, A. Borshchevsky, *J. Phys. Chem. Solids* **1997**, *58*, 1119–1125.

[114] G. J. Snyder, M. Christensen, E. Nishibori, T. Caillat, B. B. Iversen, *Nat. Mater.* **2004**, *3*, 458–463.

[115] Y. Mozharivskyj, A. O. Pecharsky, S. Bud'ko, G. J. Miller, *Chem. Mater.* **2004**, *16*, 1580–1589.

[116] J. Nylén, M. Andersson, S. Lidin, U. Häussermann, *J. Am. Chem. Soc.* **2004**, *126*, 16306–16307.

[117] W. Schweika, R. P. Hermann, M. Prager, J. Perßon, V. Keppens, *Phys. Rev. Lett.* **2007**, *99*, 1–4.

[118] C. S. Birkel, E. Mugnaioli, T. Gorelik, U. Kolb, M. Panthöfer, W. Tremel, *J. Am. Chem. Soc.* **2010**, *132*, 9881–9889.

[119] B. C. Sales, D. Mandrus, R. K. Williams, *Science* **1996**, *272*, 1325–1328.

[120] V. Keppens, D. Mandrus, B. C. Sales, B. C. Chakoumakos, P. Dai, R. Coldea, M. B. Maple, D. A. Gajewski, E. J. Freeman, S. Bennington, *Nature* **1998**, *395*, 876–878.

[121] R. P. Hermann, R. Jin, W. Schweika, F. Grandjean, D. Mandrus, B. C. Sales, G. J. Long, *Phys. Rev. Lett.* **2003**, *90*, 135505.

[122] Y. Liang, H. Borrmann, M. Baenitz, W. Schnelle, S. Budnyk, J. T. Zhao, Y. Grin, *Inorg. Chem.* **2008**, *47*, 9489–9496.

[123] M. Stokkebro Schmøkel, L. Bjerg, J. Overgaard, F. Krebs Larsen, G. K. Hellerup Madsen, K. Sugimoto, M. Takata, B. Brummerstedt Iversen, *Angew. Chem. Int. Ed.* **2013**, *52*, 1503–1506.

[124] M. S. Schmøkel, L. Bjerg, F. K. Larsen, J. Overgaard, S. Cenedese, M. Christensen, G. K. H. Madsen, C. Gatti, E. Nishibori, K. Sugimoto, et al., *Acta Crystallogr. Sect. A Found. Crystallogr.* **2013**, *69*, 570–582.

[125] E. Visnow, C. P. Heinrich, A. Schmitz, J. de Boor, P. Leidich, B. Klobes, R. P. Hermann, W. E. Müller, W. Tremel, *Inorg. Chem.* **2015**, *54*, 7818–7827.

[126] S. Stefanoski, M. Beekman, G. S. Nolas, *The Physics and Chemistry of Inorganic Clathrates*, Springer, Berlin, **2014**.

[127] G. S. Nolas, D. T. Morelli, T. M. Tritt, *Annu. Rev. Mater. Sci.* **1999**, *29*, 89–116.

[128] J. He, M. G. Kanatzidis, V. P. Dravid, *Mater. Today* **2013**, *16*, 166–176.

[129] B. Qiu, H. Bao, G. Zhang, Y. Wu, X. Ruan, *Comput. Mater. Sci.* **2012**, *53*, 278–285.

[130] T. C. Harman, P. J. Taylor, M. P. Walsh, B. E. LaForge, *Science* **2002**, *297*, 2229–2232.

[131] K. Biswas, J. He, I. D. Blum, Chun-IWu, T. P. Hogan, D. N. Seidman, V. P. Dravid, M. G. Kanatzidis, *Nature* **2012**, *490*, 570–570.

[132] D. Wu, L.-D. Zhao, X. Tong, W. Li, L. Wu, Q. Tan, Y. Pei, L. Huang, J.-F. Li, Y. Zhu, et al., *Ener. Environ. Sci.* **2015**, *8*, 2056–2068.

[133] Y. W. Chai, Y. Kimura, *Acta Mater.* **2013**, *61*, 6684–6697.

[134] J. Androulakis, C.-H. Lin, H.-J. Kong, C. Uher, C.-I. Wu, T. Hogan, B. A. Cook, T. Caillat, K. M. Paraskevopoulos, M. G. Kanatzidis, *J. Am. Chem. Soc.* **2007**, *129*,

9780–9788.

[135] C. Fu, H. Xie, T. J. Zhu, J. Xie, X. B. Zhao, *J. Appl. Phys.* **2012**, *112*, 124915.

[136] L. Gao, S. Zhai, R. Liu, N. Fu, J. Wang, G. Fu, S. Wang, *J. Am. Ceram. Soc.* **2015**, *98*, 3285–3290.

[137] L. Xi, J. Yang, C. Lu, Z. Mei, W. Zhang, L. Chen, *Chem. Mater.* **2010**, *22*, 2384–2394.

[138] X. Shi, J. Yang, J. R. Salvador, M. Chi, J. Y. Cho, H. Wang, S. Bai, J. Yang, W. Zhang, L. Chen, *J. Am. Chem. Soc.* **2011**, *133*, 7837–7846.

[139] E. S. Toberer, A. F. May, G. J. Snyder, *Chem. Mater.* **2010**, *22*, 624–634.

[140] S. R. Brown, S. M. Kauzlarich, F. Gascoin, G. J. Snyder, *Chem. Mater.* **2006**, *18*, 1873–1877.

[141] H. Zhang, H. Borrmann, N. Oeschler, C. Candolfi, W. Schnelle, M. Schmidt, U. Burkhardt, M. Baitinger, J.-T. Zhao, Y. Grin, *Inorg. Chem.* **2011**, *50*, 1250–1257.

[142] J. V. Zaikina, T. Mori, K. Kovnir, D. Teschner, A. Senyshyn, U. Schwarz, Y. Grin, A. V. Shevelkov, *Chem. Eur. J.* **2010**, *16*, 12582–12589.

[143] M. Zebarjadi, K. Esfarjani, M. S. Dresselhaus, Z. F. Ren, G. Chen, *Ener. Environ. Sci.* **2012**, *5*, 5147–5162.

[144] A. J. Minnich, M. S. Dresselhaus, Z. F. Ren, G. Chen, *Ener. Env. Sci* **2009**, *2*, 466–479.

[145] D. Hirai, E. Climent-Pascual, R. J. Cava, *Phys. Rev. B* **2011**, *84*, 174519.

[146] Y. Kobayashi, M. Tian, M. Eguchi, T. E. Mallouk, *J. Am. Chem. Soc.* **2009**, *131*, 9849–9855.

[147] J. W. Fergus, *J. Eur. Ceram. Soc.* **2012**, *32*, 525–540.

[148] E. M. Hopper, Q. Zhu, J.-H. Song, H. Peng, A. J. Freeman, T. O. Mason, *J. Appl. Phys.* **2011**, *109*, 13713.

[149] H. Ohta, W.-S. Seo, K. Koumoto, *J. Am. Ceram. Soc.* **1996**, *79*, 2193–2196.

[150] A. Magnéli, *Pure Appl. Chem.* **1978**, *50*, 1261–1271.

[151] M. Backhaus-Ricoult, J. Rustad, L. Moore, C. Smith, J. Brown, *Appl. Phys. A* **2014**, *116*, 433–470.

[152] S. Andersson, B. Collén, U. Kuylenstierna, A. Magnéli, *Acta Chem. Scand.* **1957**, *11*, 1641–1652.

[153] S. Andersson, B. Collén, G. Kruuse, U. Kuylenstierna, A. Magnéli, H. Pestmalis, S. Åsbrink, *Acta Chem. Scand.* **1957**, *11*, 1653–1657.

[154] K. Fuda, T. Shoji, S. Kikuchi, Y. Kunihiro, S. Sugiyama, *J. Electron. Mater.* **2013**, *42*, 2209–2213.

[155] D. Portehault, V. Maneeratana, C. Candolfi, N. Oeschler, I. Veremchuk, Y. Grin, C. Sanchez, M. Antonietti, *ACS Nano* **2011**, *5*, 9052–9061.

[156] S. Harada, K. Tanaka, H. Inui, *J. Appl. Phys.* **2010**, *108*, 2–8.

[157] C. Liu, L. Miao, J. Zhou, R. Huang, C. a J. Fisher, S. Tanemura, *J. Phys. Chem. C* **2013**, *117*, 11487–11497.

[158] Y. Lu, Y. Matsuda, K. Sagara, L. Hao, T. Otomitsu, H. Yoshida, *Adv. Mater. Res.* **2011**, *415–417*, 1291–1296.

[159] I. Veremchuk, I. Antonyshyn, C. Candolfi, X. Feng, U. Burkhardt, M. Baitinger, J. T. Zhao, Y. Grin, *Inorg. Chem.* **2013**, *52*, 4458–4463.

[160] M. Backhaus-ricoult, J. R. Rustad, D. Vargheese, I. Dutta, K. I. M. Work, *J. Electron. Mater.* **2012**, *41*, 1636–1647.

[161] E. Canadell, M. Whangbo, *Chem. Rev.* **1991**, *91*, 965–1034.

[162] M.-H. Whangbo, E. Canadell, P. Foury, J.-P. Pouget, *Science* **1991**, *252*, 96–98.

[163] J. S. Anderson, B. G. Hyde, *J. Phys. Chem. Solids* **1967**, *28*, 1393–1408.

[164] J. S. Anderson, R. J. D. Tilley, *J. Solid State Chem.* **1970**, *2*, 472–482.

[165] S. Andersson, A. D. Wadsley, *Nature* **1966**, *211*, 581–583.

[166] J. S. Anderson, A. S. Khan, *J. Less Common Met.* **1970**, *22*, 219–223.

[167] F. Krumeich, A. Hussain, C. Bartsch, R. Gruehn, *Anorg. Allg. Chem.* **1995**, *621*, 799–806.

[168] F. Krumeich, C. Bartsch, R. Gruehn, *J. Solid State Chem.* **1995**, *427*, 268–274.

[169] F. Krumeich, M. Wörle, A. Hussain, *J. Solid State Chem.* **2000**, *149*, 428–433.

[170] R. Roth, J. Waring, *J. Res. Natl. Bur. Stand. (1934).* **1966**, *l*, 281–303.

[171] M. R. Winter, D. R. Clarke, *J. Am. Ceram. Soc.* **2007**, *90*, 533–540.

[172] M. W. Gaultois, J. E. Douglas, T. D. Sparks, R. Seshadri, *AIP Adv.* **2015**, *5*, 97144.

[173] A. Magnéli, *Acta Crystallogr.* **1953**, *6*, 495–500.

[174] S. Iijima, S. Kimura, M. Goto, *Acta Crystallogr. Sect. A* **1973**, *29*, 632–636.

[175] S. Iijima, J. G. Allpress, *Acta Crystallogr. Sect. A* **1974**, *30*, 29–36.

[176] S. Iijima, *J. Solid State Chem.* **1975**, *14*, 52–65.

[177] S. Andersson, J. Galy, *J. Solid State Chem.* **1970**, *1*, 576–582.

[178] R. J. D. Tilley, *Int. J. Refract. Met. Hard Mater.* **1995**, *13*, 93–109.

[179] L. A. Bursill, D. J. Smith, *Nature* **1984**, *309*, 319–321.

[180] R. M. Hazen, R. Jeanloz, *Rev. Geophys.* **1984**, *22*, 37.

[181] R. H. Condit, R. R. Hobbins, C. E. Birchenall, *Oxid. Met.* **1974**, *8*, 409–455.

[182] F. Koch, J. B. Cohen, *Acta Crystallogr. Sect. B Struct. Crystallogr. Cryst. Chem.* **1969**, *25*, 275–287.

[183] L. A. Bursill, B. G. Hyde, *Acta Crystallogr. Sect. B* **1971**, *27*, 210–215.

[184] J. M. Allred, R. J. Cava, *J. Solid State Chem.* **2013**, *198*, 10–17.

[185] G. Andersson, *Acta Chem. Scand* **1954**, *8*, 1599–1606.

[186]   H. Katzke, R. Schlögl, *Z. Krist.* **2003**, *218*, 432–439.

[187]   U. Schwingenschlögl, V. Eyert, *Ann. Phys.* **2004**, *13*, 475–510.

[188]   H. A. Wriedt, *Bull. Alloy Phase Diagrams* **1989**, *10*, 271–277.

[189]   P. J. England, J. Booth, R. J. D. Tilley, T. Ekström, *J. Solid State Chem.* **1982**, *44*, 60–74.

[190]   H. Schäfer, D. Bergner, R. Gruehn, *Anorg. Allg. Chem.* **1969**, *365*, 31–50.

[191]   K. M. Nimmo, J. S. Anderson, *J. Chem. Soc. Dalt. Trans.* **1972**, 2328–2337.

[192]   S. Kimura, *J. Solid State Chem.* **1973**, *449*, 438–449.

[193]   L. A. Bursill, *Proc. R. Soc. A* **1969**, *311*, 267–290.

[194]   L. Kihlborg, *Acta Chem. Scand.* **1959**, *13*, 954–962.

[195]   L. Kihlborg, A. Magnéli, *Acta Chem. Scand.* **1955**, *9*, 471–474.

[196]   A. Magnéli, N. Hofman-Bang, P. Gjertsen, *Acta Chem. Scand.* **1948**, *2*, 501–517.

[197]   P. Gadó, A. Magnéli, R. J. V. Niklasson, J. Brunvoll, M. Hinton, *Acta Chem. Scand.* **1965**, *19*, 1514–1515.

[198]   A. Magnéli, G. Andersson, B. Blomberg, L. Kihlborg, *Anal. Chem.* **1952**, *24*, 1998–2000.

[199]   D. B. Migas, V. L. Shaposhnikov, V. E. Borisenko, *J. Appl. Phys.* **2010**, *108*, 93714.

[200]   H. A. Wriedt, *Bull. Alloy Phase Diagrams* **1989**, *10*, 368–384.

[201]   C. N. R. Rao, J. Gopalakrishnan, *New Directions in Solid State Chemistry*, Cambridge University Press, Cambridge, **1997**.

[202]   S. Patoux, M. Dolle, G. Rousse, C. Masquelier, *J. Electrochem. Soc.* **2002**, *149*, A391–A400.

[203]   S. N. Ruddlesden, P. Popper, *Acta Crystallogr.* **1957**, *10*, 538–539.

[204]   S. N. Ruddlesden, P. Popper, *Acta Crystallogr.* **1958**, *11*, 54–55.

[205]   M. Dion, M. Ganne, M. Tournoux, *Mater. Res. Bull.* **1981**, *16*, 1429–1435.

[206]   A. J. Jacobson, J. W. Johnson, J. T. Lewandowski, *Inorg. Chem.* **1985**, *24*, 3727–3729.

[207]   B. Aurivillius, *Ark. Kemi.* **1950**, *1*, 463–480.

[208]   B. Aurivillius, *Ark. Kemi.* **1950**, *1*, 499–512.

[209]   B. Aurivillius, *Ark. Kemi.* **1951**, *2*, 519–527.

[210]   K. Scheunemann, H. Müller-Buschbaum, *J. Inorg. Nucl. Chem.* **1974**, *36*, 1965–1970.

[211]   I. Levin, L. A. Bendersky, *Acta Crystallogr. Sect. B Struct. Sci.* **1999**, *55*, 853–866.

[212]   Y. Le Page, P. Strobel, *J. Solid State Chem.* **1982**, *44*, 273–281.

[213]   U. Schwingenschlögl, V. Eyert, *Ann. der Phys.* **2004**, *13*, 475–510.

[214]   E. B. Lopes, M. Almeida, J. Dumas, H. Guyot, C. Escribe-Filippini, *J. Physics-Condensed Matter* **1992**, *4*, L357–L361.

[215]   M. Greenblatt, *Chem. Rev.* **1988**, *88*, 31–53.

[216]   R. Gruehn, R. Norin, *Anorg. Allg. Chem.* **1969**, *367*, 209–218.

[217]   R. Norin, S. E. Rasmussen, E. L. Hirvisalo, J. Munch-Petersen, J. Munch-Petersen, *Acta Chem. Scand.* **1963**, *17*, 1391–1404.

[218]   R. Norin, H. Hope, R. Nevald, V. Frank, J. Brunvoll, E. Bunnenberg, C. Djerassi, R. Records, *Acta Chem. Scand.* **1966**, *20*, 871–880.

[219]   R. Norin, M. Carlsson, B. Elgquist, C. Wentrup, O. Stokke, E. Bunnenberg, C. Djerassi, R. Records, *Acta Chem. Scand.* **1966**, *20*, 2892–2893.

[220]   B. M. Gatehouse, A. D. Wadsley, *Acta Crystallogr.* **1964**, *17*, 1545–1554.

[221]   R. S. Roth, A. D. Wadsley, B. M. Gatehouse, *Naturwiss.* **1964**, *51*, 262–263.

[222]   R. Gruehn, D. Bergner, H. Schäfer, *Angew. Chem. Int. Ed.* **1965**, *4*, 1083–1096.

[223]   C. N. R. Rao, B. Raveau, *Transition Metal Oxides: Structure, Properties, and*

Synthesis of Ceramic Oxides, 2nd Edition, Wiley - VCH, **1998**.

[224] C. P. Heinrich, M. Schrade, G. Cerretti, I. Lieberwirth, P. Leidich, A. Schmitz, H. Fjeld, E. Mueller, T. G. Finstad, T. Norby, W. Tremel, *Mater. Horiz.* **2015**, *2*, 519–527.

[225] Y. Lu, M. Hirohashi, K. Sato, *Mater. Trans.* **2006**, *47*, 1449–1452.

[226] J. Nowotny, W. Li, T. Bak, *Ionics (Kiel).* **2015**, *21*, 1399–1406.

[227] Y. Lu, Y. Matsuda, K. Sagara, L. Hao, T. Otomitsu, H. Yoshida, *Adv. Mater. Res.* **2012**, *415–417*, 1291–1296.

[228] I. Tsuyumoto, T. Hosono, M. Murata, *J. Am. Ceram. Soc.* **2006**, *89*, 2301–2303.

[229] J. Tang, W. Wang, G.-L. Zhao, Q. Li, *J. Phys. Condens. Matter* **2009**, *21*, 205703.

[230] N. A. Deskins, M. Dupuis, *J. Phys. Chem. C* **2009**, *113*, 346–358.

[231] L. R. Sheppard, T. Bak, J. Nowotny, *J. Phys. Chem. C* **2008**, *112*, 611–617.

[232] G. Kieslich, I. Veremchuk, I. Antonyshyn, W. G. Zeier, C. S. Birkel, K. Weldert, C. P. Heinrich, E. Visnow, M. Panthöfer, U. Burkhardt, Y. Grin, W. Tremel, *Phys. Chem. Chem. Phys.* **2013**, *15*, 15399–15403.

[233] G. Kieslich, C. S. Birkel, J. E. Douglas, M. Gaultois, I. Veremchuk, R. Seshadri, G. D. Stucky, Y. Grin, W. Tremel, *J. Mater. Chem. A* **2013**, *1*, 13050–13054.

[234] G. Kieslich, U. Burkhardt, C. S. Birkel, I. Veremchuk, J. E. Douglas, M. W. Gaultois, I. Lieberwirth, R. Seshadri, G. D. Stucky, Y. Grin, W. Tremel, *J. Mater. Chem. A* **2014**, *2*, 13492–13497.

[235] G. Kieslich, W. Tremel, *AIMS Mater. Sci.* **2014**, *1*, 184–190.

The contents of the following chapter are taken and partially adapted from *Materials Today: Proceedings*, **2016**, submitted.

Authorship contributions

Category 1

Conception and design of study:

G. Cerretti, G. Kieslich, W. Tremel.

Acquisition of data:

G. Cerretti – preparation of samples.

G. Cerretti – PXRD refinement.

G. Cerretti – measurements of the thermoelectric properties and Hall measurements.

G. Cerretti – SEM images.

B. Balke – ESCA measurements.

Analysis and/or interpretation of data:

G. Cerretti, B. Balke.

Category 2

Drafting the manuscript: G. Cerretti.

Revising the manuscript critically for important intellectual content: B. Balke, W. Tremel.

Category 3

Approval of the version of the manuscript to be published:

G. Cerretti, B. Balke, G. Kieslich, W. Tremel.

FIGURE 2.1: PREPARED BY G. CERRETTI.
FIGURE 2.2: PREPARED BY G. CERRETTI.
FIGURE 2.3: PREPARED BY B. BALKE AND G. CERRETTI.
FIGURE 2.4: PREPARED BY B. BALKE AND G. CERRETTI.
FIGURE 2.5: PREPARED BY B. BALKE AND G. CERRETTI.

# 2   Optimizing the charge carrier concentration of the WO$_{3-x}$ compounds

2.1   Motivation

In the 1950's Magnéli discovered reduced early transition metals oxides, the so-called Magnéli phases.[1] Among them the most studied materials for thermoelectric applications have been the Magnéli phases of Ti [2,3] and W.[4,5] Their peculiarity is the presence of periodic defects, called crystallographic shear (CS) planes which, acting as phonons scattering centers, ensure low values of thermal conductivity. In the Magnéli phases of tungsten oxides, the CS planes forms due to localized oxygen deficiencies. To overcome these lacks, the crystal structure has to rearrange itself. The ReO$_3$ like structure is formed by corner sharing octahedrons which, as a consequence of these oxygen deficiencies, reorder themselves generating parallel blocks of edge sharing octahedrons. These alterations of the crystal structure are the so-called crystallographic shear (CS) planes. Such compounds with adaptive structures are very interesting materials for TE applications because they offer the opportunity to overcome the limitation of the zT optimization. Indeed, the challenge to fulfil the "phonon-glass electron-crystal" concept is to decouple the optimization of the electronic properties from the thermal transport properties. As a matter of fact, the electronic properties of these kind of materials can be modified, through the manipulation of the charge carrier concentration, without affecting their intrinsic low thermal conductivity. In this chapter is shown how we effectively manipulated the charge carrier concentration in order to increase the thermoelectric properties of an already promising tungsten Magnéli phase, the W$_{10}$O$_{29}$ (WO$_{2.90}$). This compound is an *n*-type material with a metallic behavior, therefore to increase its thermoelectric performances

a reduction of the number of the available electrons has to be performed. This could be achieved increasing the oxygen content of the final composition.

2.2   Experimental

2.2.1   Synthesis

The reduced tungsten oxide $WO_{2.90}$ ($W_{10}O_{29}$), member of the Magnéli series W_nO_{3n-1}, was prepared according to the reaction:

$$\frac{29}{30}WO_3 + \frac{1}{30}W = WO_{2.90} \tag{16}$$
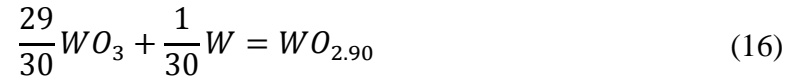
using commercially available W (99.9% - Sigma Aldrich) and WO_3 (99.9% - Sigma Aldrich) as precursors. This first specimen was taken as the reference sample for the further comparison of the obtained results. In order to optimize the thermoelectric properties, WO_3 nano-powders (NP; <100 nm - Sigma-Aldrich) were added to the previous composition. The choice of nano-powders was driven by the idea of creating a multiscale grain size distribution to increase the phonon scattering and hence reduce the thermal conductivity. Two further samples, containing 5 and 10 *wt%* of WO_3 nano powders respectively, were synthesized. In the following sections we will refer to the probes using the sample names listed in Table 2.1. In the same table the relative compositions, the measured stoichiometry, and the final densities of each sample are listed.

Sample name	Mixtures composition	Measured stoichiometry (XPS)	Density %
Ref.	$WO_{2.90}$	$WO_{2.90}$	96
NP-5	$WO_{2.90}$+5 *wt%* np	-	96
NP-10	$WO_{2.90}$+10 *wt%* np	$WO_{2.91}$	95

Table 2.1: Sample name, composition, measured stoichiometry, and densities of the sintered pellets. The relative densities are percentage of the theoretical value.

To synthesize the specimens, the starting molecules were weighted and homogenized in an agate mortar, prior to loading them in a 20 mm graphite die. A thin carbon foil was used to cover the internal surfaces to avoid any contact, hence contamination, between the die walls and the powders. The samples were synthesized through a SPS-assisted (FCT HP D 25) preparation similar to the one previously described in reference.[4] A pressure of 50 MPa, a maximal temperature of 1473 K, and a heating rate of 50 K/min were used. To ensure that both, the reaction and the consolidation of the pellets were completed, the maximum temperature was held for 10 minutes. Afterwards, the samples were cooled down to room temperature and the obtained cylindrical pellets were thoroughly polished to remove the carbon substrate and any potentially formed carbides.

2.2.2   Characterization

Powder X-ray diffraction (PXRD) measurements were used to check the phase purity of the synthesized materials. Parts of each pellet were ground until obtaining a fine powder and subsequently loaded on a two-circle-diffractometer (Siemens D5000) equipped with a Germanium (220) primary beam monochromator (CuK$_\alpha$ = 154.061 pm) and a Braun M50 position sensitive detector in transmission geometry. The software FullProf Suite 3.0 was used to refine the resulting profiles applying the fundamental parameter approach. The real stoichiometry of the Ref. and NP-10 samples were measured on a ESCA device from PREVAC equipped with a SCIENTA R4000 X-ray photoelectron spectrometer using Al K$_\alpha$ radiation (450 W, 15 kV, 30 mA). The binding energy was calibrated by setting the C 1s peak to 284.5 eV. The resolution of the ESCA analysis is ca. 1.0 eV. Fitting the core level spectra of W (4f) and O (1s) we were able to analyze the W to O ratio and therefore compute the overall stoichiometry.

To perform a complete thermoelectric characterization a bar-shaped and a square-shaped specimen with dimensions of $2 \times 1.5 \times 10$ mm^3 and $10 \times 10 \times 1.5$ mm^3 respectively, were cut out from each pellet using a linear precision diamond blade saw (Buehler IsoMet 4000). The Seebeck coefficient and the electrical resistivity were measured simultaneously on the bar-shaped samples in the temperature range 373 - 1223 K using a four points Linseis LSR-3 device. The square-shaped samples were used for both the measurement of the charge carrier

density and the thermal diffusivity. An IPM-HT-HALL-900K device was used for the evaluation of the carrier concentration. Such device has a four contact setup and the measurement is carried out using the van der Pauw method.[6] Temperature dependent thermal diffusivity D measurements were performed on a LFA 457 Microflash from Netzsch. In order to minimize errors in the emissivity, the samples were coated with a thin graphite layer prior the measurements. The used values of the heat capacity C_p are in agreement with the previously measured ones and reported in[4]. The physical densities d of the samples weres derived from the measured mass-to-volume ratio and resulted to be between 95% and 96% of the theoretical value for $WO_{2.90}$. The temperature dependent thermal conductivity κ was then obtained using the relationship:

$$\kappa = D \cdot C_p \cdot d \tag{17}$$

2.3 Results and discussion

2.3.1 Synthesis and structural characterization

The results of the PXRD measurements show that all three samples are phase pure $WO_{2.90}$ (Figure 2.1). We can hence deduce that the added amount of WO_3 nano-powders did not affect the composition and the crystal structure of the obtained compounds. The calculated densities of the sintered pellets (Ref., NP-5 and NP-10) are comparable and all above the 95% of the theoretical value for $WO_{2.90}$, making them adequate for thermoelectric applications.
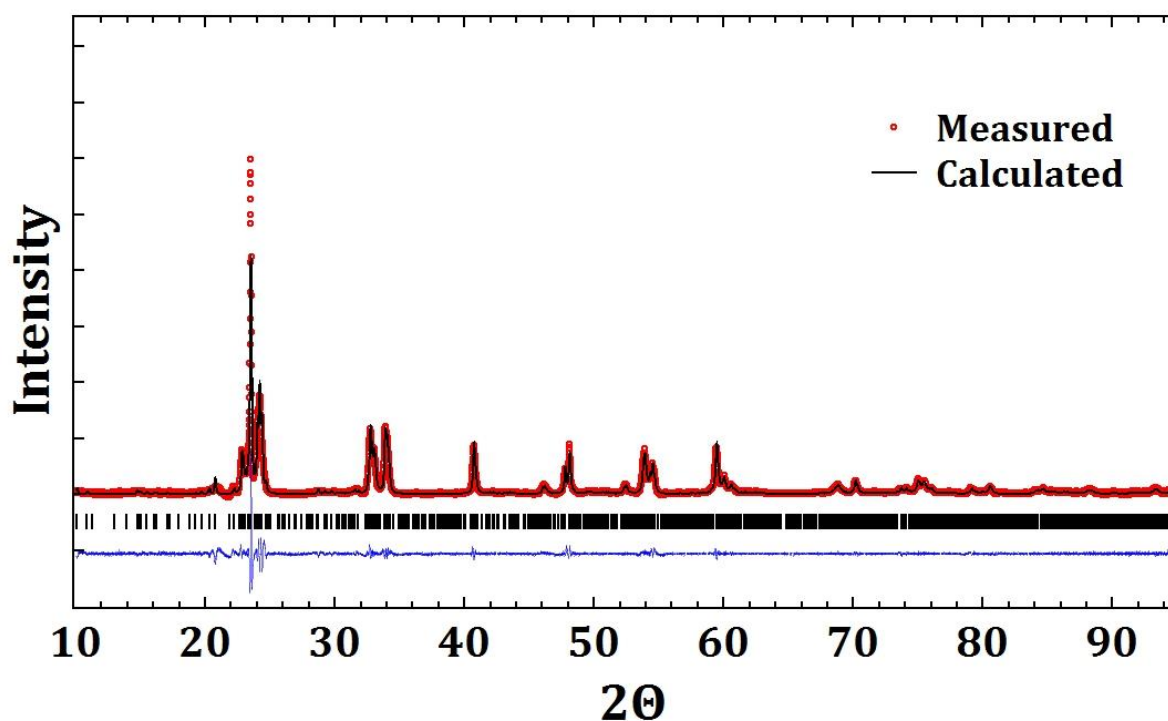
Figure 2.1: Refinement performed on the PXRD data for the sample NP-10. The patter shows that also this sample is single phase $WO_{2.90}$, meaning that the WO_3 powders had no effect on the stoichiometry and the crystal structure.

The high density is also confirmed by the scanning electron microscopy (SEM) images. Indeed, Figure 2.2a proves the complete lack of porosity of the pellets. The nanosize distribution of the grains confirm the efficiency of the SPS technique in limiting the grain growth during the sintering process.[7,8] Furthermore, the generated nanostructure is expected to have a positive

58

effect on the thermal conductivity because it has been already shown that the grain boundaries act as effective phonons scattering centers.[9] Figure 2.2b shows the cross sections of the samples proving the layered structure of the materials, which is an intrinsic characteristic of the WO_{3-x} phases.
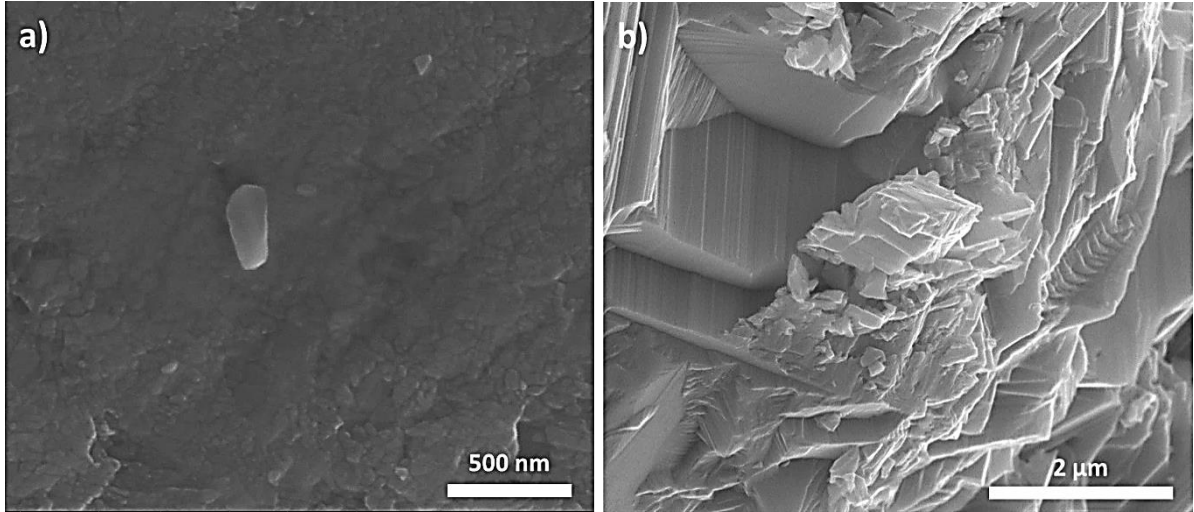

Figure 2.2: SEM images of the as sintered samples showing the lack of porosity in the samples and the intrinsic nanostructure of the pellets (a). The generated layered structure which is characteristic of the $WO_{2.90}$ phase is shown in (b).

2.3.2 Thermoelectric performances

A strategy to optimize the figure of merit consist in the manipulation of the charge carrier concentration. In the range of 10^{19} - 10^{20} cm^{-3}, hence in the semiconductor region, most of materials show their maximum in zT.[10] Adding WO_3 powders to the $WO_{2.90}$ composition, our purpose is to reduce the charge carrier concentration. At the same time, we want to leave untouched the crystal structure of the $W_{10}O_{29}$ phase because its intrinsic defects (CS planes) ensure low values of thermal conductivity. An increase of the oxygen content decreases the number of free electrons of the conduction band reducing the charge carrier concentration (*n*-type conduction) towards values closer to the semiconductor regime. As can be seen from Figure 2.3a the measured values of *n* are reduced to almost one half, even if the overall counting still indicates a metallic behavior. We tried to further reduce the carrier concentration

adding 20, 30, and 40 *wt*% WO₃ NP, but any attempt led to the creation of side phases and mechanical instability of the samples.
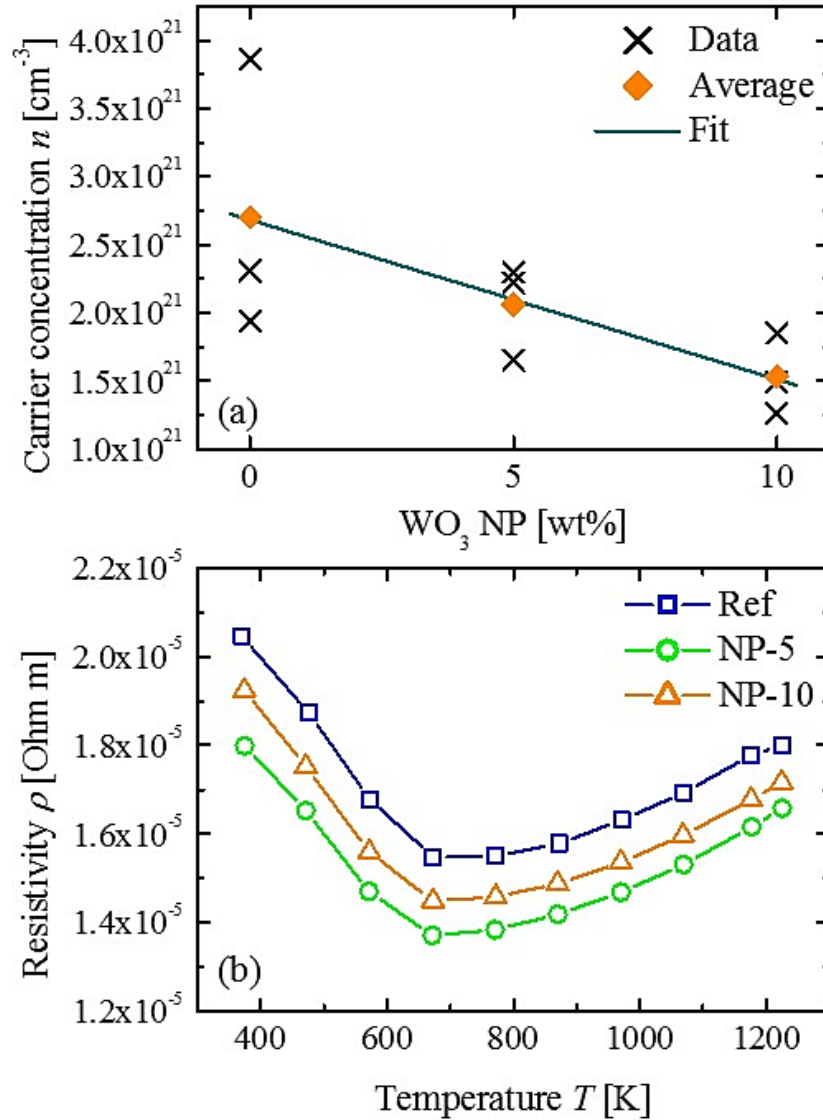

Figure 2.3: Reduction of the charge carrier concentration n upon increase of the oxygen content (a). Comparison of the electrical resistivity ρ for the prepared samples (b).

The trend of the electrical resistivity as a function of temperature is the same for all the samples. The measured values are comparable with those showed by heavily doped semiconductors or early transition metal compounds. The electrical resistivity seems to depend on the direction of formation of the CS planes. With increasing values of x (WO$_{3-x}$) the distribution of the CS planes passes from randomly oriented to periodic and parallel, rising the electrical conductivity

and reducing the activation energy.[11] In general, the measured electrical resistivity of the three sample does not show a clear trend between its value and the sample composition.
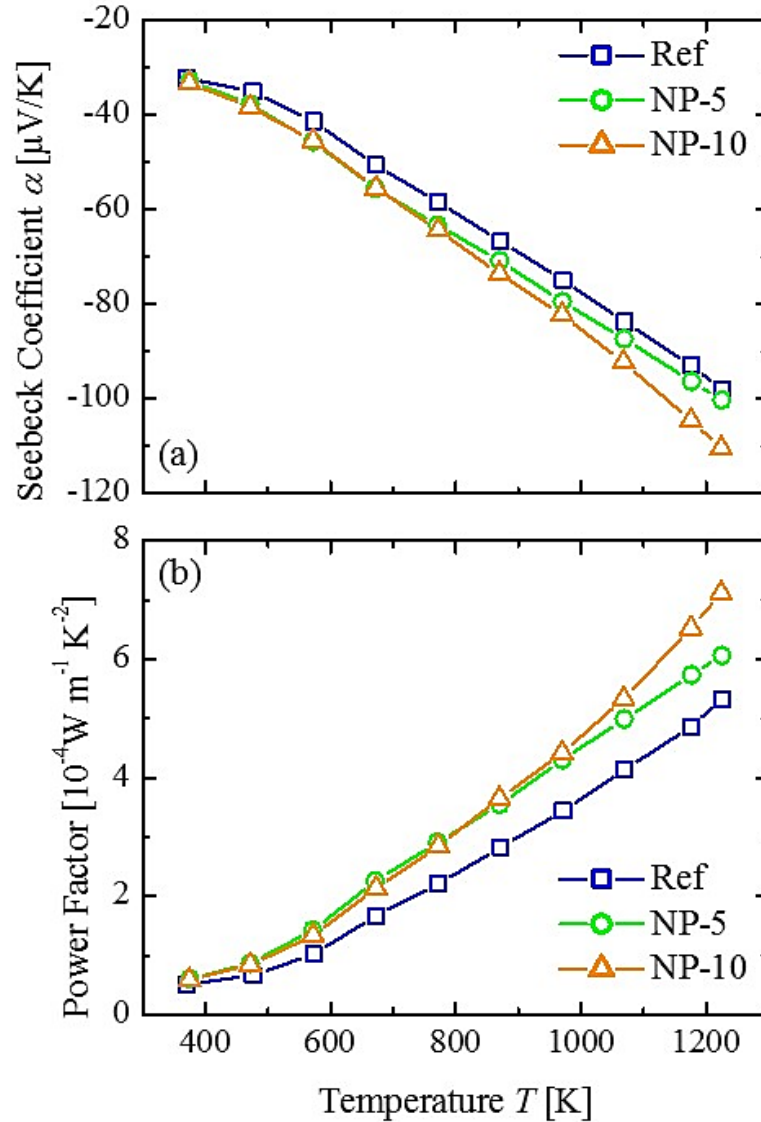

Figure 2.4: Trend of the Seebeck coefficient *S* in function of the temperature (a). The negative values of *S* mean that the samples are *n*-type conductors. Variation of the power factor *PF* with increasing temperatures (b).

On the other hand, the effect of the higher oxygen content, and hence a charge carriers reduction, is more evident in the Seebeck coefficient measurements. Indeed, the absolute value of the thermopower raises along with the oxygen content of the sample, up to a value of -117 µV/K at 1223 K. The negative measured values of *S* confirm that these are *n*-type materials,

therefore the charge carriers are electrons. The Seebeck coefficient and the power factor increase with increasing temperature, without showing any absolute maximum in the chosen temperature range (see Figure 2.4). The fact they have not yet reached their maximum values around 1200 K is a characteristic behavior of wide-gap semiconductors.

The power factor, being defined as

$$PF = \frac{S^2}{\rho} \tag{18}$$

is mainly affected by the increase of the thermopower rather than ρ. This dependence is even more evident since the electrical resistivity values are very similar for all the samples.

The thermal conductivity measurements show comparable values, but with a small increase for the samples with higher oxygen content. These higher values of κ could be linked to the CS planes. Since they are formed as a consequence of an oxygen deficiency, the higher oxygen content of the samples NP-5 and NP-10 could induce the formation of discontinuities along the CS planes. In these points the octahedra would move back to a corner sharing configuration creating "bridges" where the phonons are free to pass. The choice of WO_3 nano-powders rather than normal size WO_3 powders was led by the idea of further reducing κ through the generation of randomly distributed nanoclusters. On the contrary, from the measurements we can deduce that the nano-powders had no effect. Probably the size of the added nano-powders is in the same range of the already achieved level of nanostructuring (see Figure 2.2a). Despite this, the measured values of thermal conductivity are small compared to other conductive oxides.[12–14]
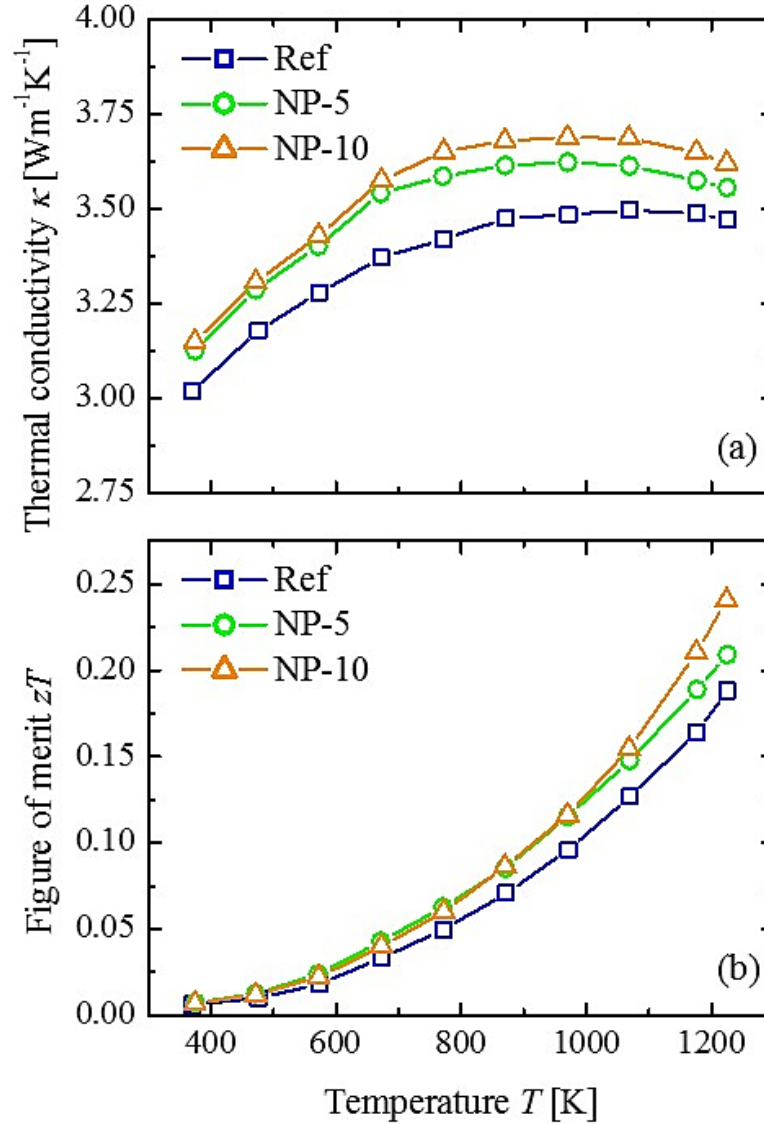
Figure 2.5: Plot of the thermal conductivity κ showing that the measured values are similar for all the prepared samples (a). The highest zT value is registered for the sample NP-10 with a value of 0.24 at 1223 K (b).

Figure 2.5b reports the calculated values of zT. We can observe that up to 1223 K a maximum is not achieved yet, for none of the samples. The highest registered figure of merit is equal to 0.24 at 1223 K for the sample NP-10, roughly 30% higher than the reference sample. We can state that this increase in zT is mainly due to the reduction of charge carriers. In fact, the thermal conductivity remained within an acceptable range upon oxidation, meanwhile the absolute Seebeck coefficient was increased. Even if the maximum value obtained here is still lower than the best thermoelectric oxides, [15–18] the adopted optimization strategy gave promising results.

2.4 Summary

In this chapter is reported the optimization of the already known $WO_{2.90}$ Magnéli phase adding WO_3 nano-powders in two different concentrations (5 and 10 $wt\%$) to the $W_{10}O_{29}$ composition. We showed how the induced higher oxygen content, which led to the reduction of the charge carrier concentration, modified the thermoelectric properties without affecting the crystal structure. We chose nano-powders with the idea of further reducing the thermal conductivity, but as seen in Figure 2.5a they had no effect on κ. On the contrary, the higher oxygen content induced a slight increase of the thermal conductivity. As showed by the X-ray patterns, the added amount of WO_3 was not enough to induce a phase change. This allowed to keep the intrinsic defects of the Magnéli phases, like CS planes, that ensure effective phonons scattering. On the other hand, the decrease of n had positive effects on the electronic properties. The value of the thermopower raised until -117 µV/K at 1223 K. This gain positively affected the figure of merit that arrived at 0.24, optimizing of almost 30% the reference value.

The research on the Magnéli phases for thermoelectric applications is still a relatively unexplored world even if they already showed their potential.[2,3,5] Moreover, the possibility to manipulate the charge carrier concentration without altering the characteristic low thermal conductivity, makes the Magnéli phases of the early transition metal oxides even more interesting materials.

References

[1]   A. Magnéli, *Acta Crystallogr.* **1953**, *6*, 495–500.

[2]   I. Veremchuk, I. Antonyshyn, C. Candolfi, X. Feng, U. Burkhardt, M. Baitinger, J. T. Zhao, Y. Grin, *Inorg. Chem.* **2013**, *52*, 4458–4463.

[3]   Y. Lu, Y. Matsuda, K. Sagara, L. Hao, T. Otomitsu, H. Yoshida, *Adv. Mater. Res.* **2011**, *415–417*, 1291–1296.

[4]   G. Kieslich, C. S. Birkel, J. E. Douglas, M. Gaultois, I. Veremchuk, R. Seshadri, G. D. Stucky, Y. Grin, W. Tremel, *J. Mater. Chem. A* **2013**, *1*, 13050–13054.

[5]   G. Kieslich, I. Veremchuk, I. Antonyshyn, W. G. Zeier, C. S. Birkel, K. Weldert, C. P. Heinrich, E. Visnow, M. Panthöfer, U. Burkhardt, Y. Grin, W. Tremel, *Phys. Chem. Chem. Phys.* **2013**, *15*, 15399–15403.

[6]   L. J. van der Pauw, *Philips Res. Reports* **1958**, *13*, 1–9.

[7]   D. V. Dudina, A. G. Anisimov, V. I. Mali, N. V. Bulina, B. B. Bokhonov, *Mater. Lett.* **2015**, *144*, 168–172.

[8]   O. Ravkina, J. Räthel, A. Feldhoff, *J. Eur. Ceram. Soc.* **2015**, *35*, 2833–2843.

[9]   K. Biswas, J. He, I. D. Blum, Chun-IWu, T. P. Hogan, D. N. Seidman, V. P. Dravid, M. G. Kanatzidis, *Nature* **2012**, *490*, 570–570.

[10]   G. J. Snyder, E. S. Toberer, *Nat. Mater.* **2008**, *7*, 105–114.

[11]   W. Sahle, M. Nygren, *J. Solid State Chem.* **1983**, *48*, 154–160.

[12]   T. Tsubota, M. Ohtaki, K. Eguchi, H. Arai, *J. Mater. Chem.* **1997**, *7*, 85–90.

[13]   G. Ren, J. Lan, C. Zeng, Y. Liu, B. Zhan, S. Butt, Y. H. Lin, C. W. Nan, *J. Miner. Met. Mater. Soc.* **2015**, *67*, 211–221.

[14]   A. Nag, V. Shubha, *J. Electron. Mater.* **2014**, *43*, 962–977.

[15]   M. Lee, L. Viciu, L. Li, Y. Wang, M. L. Foo, S. Watauchi, R. a Pascal, R. J. Cava, N. P. Ong, *Nat. Mater.* **2006**, *5*, 537–540.

[16]   Y. L. Pei, H. Wu, D. Wu, F. Zheng, J. He, *J. Am. Chem. Soc.* **2014**, *136*, 13902–13908.

[17]   J. Sui, J. Li, J. He, Y.-L. Pei, D. Berardan, H. Wu, N. Dragoe, W. Cai, L.-D. Zhao, *Ener. Environ. Sci.* **2013**, *6*, 2916–2920.

[18]   J. Le Lan, Y. C. Liu, B. Zhan, Y. H. Lin, B. Zhang, X. Yuan, W. Zhang, W. Xu, C. W. Nan, *Adv. Mater.* **2013**, *25*, 5086–5090.

The following chapter contains a partially adapted reproduction of the contents published in *Mater. Horiz.* **2015**, *2*, 519–527[1]. The taken parts are delimited by quotation marks.

This project was developed in collaboration with the Centre for Materials Science and Nanotechnology at the University of Oslo (FERMIO), and the Institute of Materials Research of the German Aerospace Center (DLR).

Authorship contributions

Category 1

Conception and design of study:

C. P. Heinrich, G. Cerretti, W. Tremel.

Acquisition of data:

C. P. Heinrich – preparation of samples with $x = 0, 0.075, 0.1, 1$.

M. Schrade, H. Fjeld, T. G. Finstad – measurements of the thermoelectric properties and thermogravimetric analysis of the prepared samples.

G. Cerretti – preparation of samples with $x = 1, 2$; consolidation and thermoelectric characterization of the same samples.

I. Lieberwirth – HRTEM micrographs.

P. Leidich – SEM images.

A. Schmitz – consolidation of samples.

Analysis and/or interpretation of data:

C. P. Heinrich, M. Schrade, G. Cerretti.

Category 2

Drafting the manuscript: C. P. Heinrich, M. Schrade.

Revising the manuscript critically for important intellectual content: G. Cerretti, E. Mueller, T. Norby, W. Tremel.

Category 3

Approval of the version of the manuscript to be published:

C. P. Heinrich, M. Schrade, G. Cerretti, I. Lieberwirth, P. Leidich, A. Schmitz, H. Fjeld, E. Mueller, T. G. Finstad, T. Norby, W. Tremel.

FIGURE 3.2: PREPARED BY P. LEIDICH.

FIGURE 3.3: PREPARED BY C. P. HEINRICH.

FIGURE 3.4: PREPARED BY I. LIEBERWIRTH.

FIGURE 3.5: PREPARED BY M. SCHRADE.

FIGURE 3.6: PREPARED BY M. SCHRADE.

FIGURE 3.7: PREPARED BY C. P. HEINRICH AND M. SCHRADE.

FIGURE 3.8: PREPARED BY C. P. HEINRICH AND M. SCHRADE.

FIGURE 3.9: PREPARED BY C. P. HEINRICH AND M. SCHRADE.

FIGURE 3.10: PREPARED BY C. P. HEINRICH AND M. SCHRADE.

3   Study of the early substituted compounds of the tetragonal tungsten bronze series $Nb_{8-x}W_{9+x}O_{47-\delta}$

3.1   Motivation

"Oxides exhibit great thermoelectric potential due to their abundance, to the high chemical and physical stability and to the low toxicity. However, thermoelectric oxides exhibit in general lower zT values than competing non-oxide materials.[2,3] In thermoelectric generators (TEGs) both n-type and p-type thermoelectric materials must be combined. Among the oxides, the highest zT values have been reported for layered cobaltates[4–7] (p-type), whereas different materials have been suggested as n-type thermoelectrics. Among the best performing n-type materials so far most are wide band-gap semiconductors like ZnO,[8,9] In_2O_3,[10–12] or $SrTiO_3$,[13] with power factors comparable to those of non-oxide state of the art materials. However, their high crystallographic symmetry and small unit cells lead to relatively high thermal conductivities, which seriously limits their zT values.[8,13,14]

Engineering of nanoscaled structures may help controlling the electrical and thermal transport in solids, in particular for thermoelectric applications that require the combination of low thermal conductivity and low electrical resistivity. Therefore, materials containing inherent phonon scattering centers at the atomic level have attracted scientific attention recently. The tetragonal tungsten bronzes series $Nb_{8-x}W_{9+x}O_{47}$ allow a continuous variation of the charge carrier concentration while fulfilling the concept of a ''phonon-glass electron-crystal'' through a layered nanostructure defined by intrinsic crystallographic shear planes. The structure of the complete series was investigated previously by HRTEM and electron diffraction by Krumeich et al.[15–17] The so called 4:9 phase ($Nb_8W_9O_{47} = 4 \cdot Nb_2O_5 + 9 \cdot WO_3$) and the complete series

of $Nb_{8-x}W_{9+x}O_{47}$, with x ranging from 0 to 5, crystallize in a threefold superstructure (lattice parameters $a = 12.251$ Å; $b = 36.621$ Å, $c = 3.94$ Å) of the basic TTB structure.[17] The crystal structure of these compounds is formed by corner sharing octahedra that form pentagonal tunnels partially filled by metal and oxygen atoms which give rise to the formation of pentagonal bipyramids (Figure 3.1).[15]
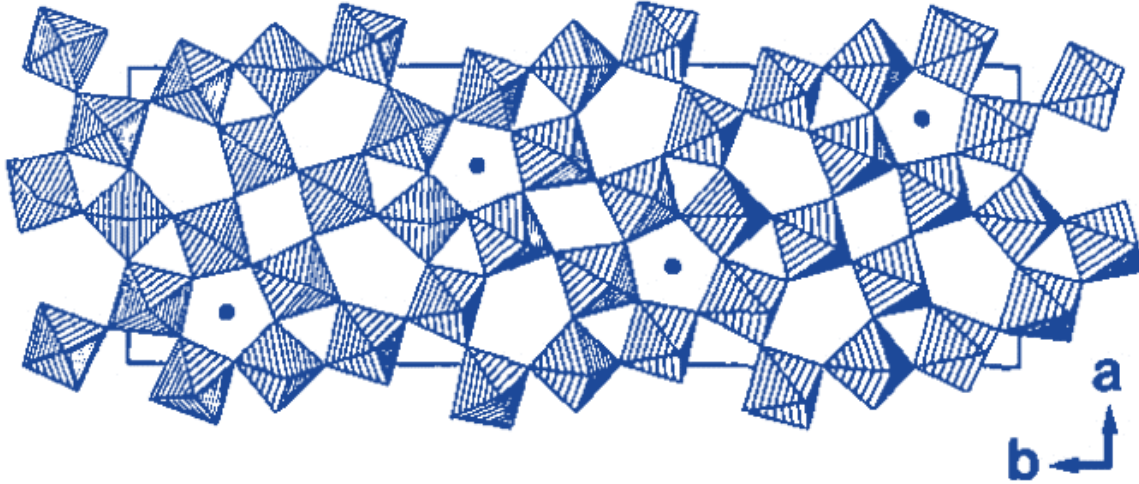

Figure 3.1: Crystal structure of the $Nb_{8-x}W_{9+x}O_{47}$ series. The formed pentagonal tunnels are partially filled with metal ions that linked to the oxygen atoms give rise to pentagonal bipyramids. Image adapted from literature.[15]

Due to the very large unit cell low values of the lattice thermal conductivity are expected. Starting from the composition $Nb_8W_9O_{47}$ with Nb and W in their highest oxidation states, the niobium Nb^{5+} is progressively replaced according to the relation $2Nb^{5+} \rightarrow M^{4+} + W^{6+}$ ($M^{4+} = Nb^{4+}$ or W^{4+}). The amount of transition metal ions in a lower oxidation state as compared to the pristine structure increases with increasing x, which corresponds to an increase in the electronic charge carrier concentration, being these materials are all n-type conductors. Since the main characteristics of the crystal structure are preserved over substitution, and hence also the thermal conductivity, the tetragonal tungsten bronzes $Nb_{8-x}W_{9+x}O_{47}$ with $0 \leq x \leq 5$ allow the independent optimization of the electronic and phononic transport properties.

In this chapter the thermoelectric properties of the TTB series $Nb_{8-x}W_{9+x}O_{47-\delta}$, with $0 \leq x \leq 2$, were studied in the temperature range from 373 to 973 K. Furthermore, the structural defects

and the thermal stability of the samples were investigated, under various oxygen partial pressure pO_2, by means of thermogravimetry, HRTEM, and PXRD.

3.2   Experimental

3.2.1   Synthesis and powder processing

Bulk samples of polycrystalline $Nb_{8-x}W_{9+x}O_{47}$ with compositions $x = 0, 0.075, 0.1, 1, 2$ were prepared by solid state reactions using powders of NbO_2 (Alfa Aesar, 99+%), Nb_2O_5 (ABCR, 99.5%), and WO_3 (Alfa Aesar, 99.8%). The phase purity of all starting materials was verified by X-ray diffraction. Annealing was performed in evacuated quartz ampoules, which were preheated at 1073 K under dynamic vacuum for 5 hours to ensure dry conditions. The stoichiometric amounts of the starting compounds were thoroughly ground, sealed in quartz ampoules, and annealed in a first step at 1173 K for 12 hours. In a second step, the harvested powders were ground again, re-sealed and re-annealed for 12 hours at 1173 K to ensure a homogeneous element distribution. Heating and cooling rates for all procedures in the horizontal tube furnaces were 5 Kmin^{-1}. The quartz ampoules were 10–12 cm in length and 11 mm in inner diameter with a maximum of 4 g starting materials per ampoule. The resulting powders of $Nb_{8-x}W_{9+x}O_{47}$ were manually ground. The phase purity was verified by powder X-ray diffraction prior to consolidation and characterization.

Batches of bulk powders with different degrees of substitution were used for consolidation into 1-1.5 mm thick, 12.7 mm diameter disks at 1173 K under vacuum and a pressure of 56 MPa by current-assisted short-time sintering utilizing a DSP (Direct sintering press). Boron nitride coated high density graphite was used as die material. In the first consolidation segment the pressure was applied, followed by a 6 min heating segment to 1173 K. After 10 min sintering time the pressure was released to 2 MPa, and the sample was cooled down to room temperature over a period of 6 min to obtain strain-free materials. The resulting pellets had > 95% theoretical density, as determined by the Archimedes method.

3.2.2   Characterization details

Room temperature powder X-ray diffraction measurements were performed on a Siemens D5000 powder diffractometer in transmission geometry with a Braun M50 position sensitive

detector, Ge (220) monochromator and CuK$_\alpha$ radiation, with a step size of 0.00781 in *2θ*. Le Bail fits of all diffraction data were performed with TOPAS Academic V4.152 applying the fundamental parameter approach using the crystallographic data from Craig and Stephenson as structure mode.l[18]

Thermogravimetric (TG) measurements were conducted using a CI Electronics MK2 microbalance. The atmospheric composition, in particular the oxygen partial pressure *pO$_2$* was controlled by an in-house-built gas mixer, of a type described elsewhere.[19] The sample and the counterweight were attached to the arms of the balance with platinum wires. The sample was hanging in an alumina tube in a vertical tube furnace and the counterweight was hanging in a glass tube kept at room temperature. To ensure equilibrium, the weight was monitored isothermally at constant *pO$_2$* values. Mixtures of O$_2$ and Ar were used to obtain an oxygen partial pressure between $\approx 10^{-5}$ and 1 atm. Lower oxygen partial pressures of up to 10^{-15} atm could be obtained by diluting CO in a carrier gas (CO + 1/2 O$_2$ = CO$_2$). All thermogravimetric reductions and oxidizations were performed under conditions where the tetragonal tungsten bronzes are stable as confirmed by X-ray diffraction. To measure the electrical conductivity and the Seebeck coefficient at high temperatures, we used a custom-built assembly mounted into a NorECs ProboStat measurement cell as described elsewhere.[20,21] The gas atmosphere in the measurement cell was controlled using a similar gas mixer as for the thermogravimetric investigation. The maximum temperature (973 K) and the atmospheric composition during the electrical measurements were chosen to prevent oxidation or reduction of the sample during the measurement. Based on previous TG experiments, this could be achieved by measuring in argon (*pO$_2$* 10^{-5} atm) for T > 773 K and diluted CO (*pO2* $\approx 10^{-15}$ atm) for T < 773 K.

Thermal diffusivity was measured in N$_2$ flow using a Netzsch laser flash diffusivity instrument (LFA micro flash 457). The thermal conductivity was calculated using the measured thermal diffusivity and sample density in combination with the heat capacity (*C$_p$*) calculated from the Dulong-Petit law.[22]

Scanning electron microscopy (SEM) images of the as-synthesized powders and the sintered pellets were recorded using a FEI Nova NanoSEM600 equipped with an Everhart-Thornley detector (ETD) and a low voltage high contrast detector (vCD) in high vacuum mode.

High-resolution transmission electron microscopy (HRTEM) images were taken using a FEI Tecnai F20 with an acceleration voltage of 200 kV. Samples were either finely crushed in an

agate mortar or cut with a microtome into 1–10 nm thick slices, then dispersed in ethanol and drop casted on a carbon-lacey grid.

3.3 Result and discussion

3.3.1 Synthesis and powder processing

Starting from the binary oxides, the solid state synthesis of the complete series $Nb_{8-x}W_{9+x}O_{47}$ with $0 \leq x \leq 5$ is possible.[15] The screening of reaction parameters showed that the 4:9 phase and the complete series of tetragonal tungsten bronzes can easily be obtained in larger batches of several grams at temperatures as low as 1173 K with short reaction times of 12 h. To ensure a homogeneous cation distribution, all samples were subjected to a second annealing step at 1173 K for 12 h after the powder was thoroughly ground and re-sealed in an ampoule. Cation substituted, hence reduced, samples are known to be oxidized at high temperatures under structural changes and/or decomposition, for example 8 $Nb_7W_{10}O_{47}$ + 2 O_2 → 7 $Nb_8W_9O_{47}$ + 17 $WO_{3.57}$. Therefore, both annealing steps were conducted under vacuum to prevent oxidation at higher T. The obtained powder of the unsubstituted end member $Nb_8W_9O_{47}$ exhibits a gray color, whereas all cation substituted samples exhibit a dark blue to purple color. This dark color is an indication of substantial concentrations of electronic defects, most likely itinerant electrons, confirming that the cation substitution is compensated to a large extent by electrons, thereby increasing the charge carrier concentration. The light gray color of the unsubstituted $Nb_8W_9O_{47}$ suggests that after synthesis already a few electron charge carriers are present, induced by the formation of oxygen vacancies during synthesis.

A series of samples with a low degree of substitution and nominal composition $Nb_{8-x}W_{9+x}O_{47}$ with x = 0, 0.075, 0.1, 1, and 2 were prepared to obtain a first assessment of the thermal stability, the thermoelectric transport properties and the electronic optimization potential of cation substituted TTBs.

In order to conduct proper thermoelectric characterization, the powders were consolidated into dense pellets by hot-pressing or current-assisted short-time sintering (also called spark plasma sintering, SPS). In the case of hot-pressing, the high temperatures, the reducing conditions, and the long consolidation times needed to obtain dense pellets induced material deterioration, as verified by PXRD of the consolidated pellets. Therefore, these pellets were not suited for further characterization. The use of current-assisted sintering, however, allowed the

combination of short sintering times with a relatively low consolidation temperature of 1173 K. No sample deterioration was observed via PXRD. The resulting short-time sintered pellets had all densities $> 95\%$. Scanning electron microscopy images were taken of the as-synthesized TTB powders and consolidated pellets (Figure 3.2).
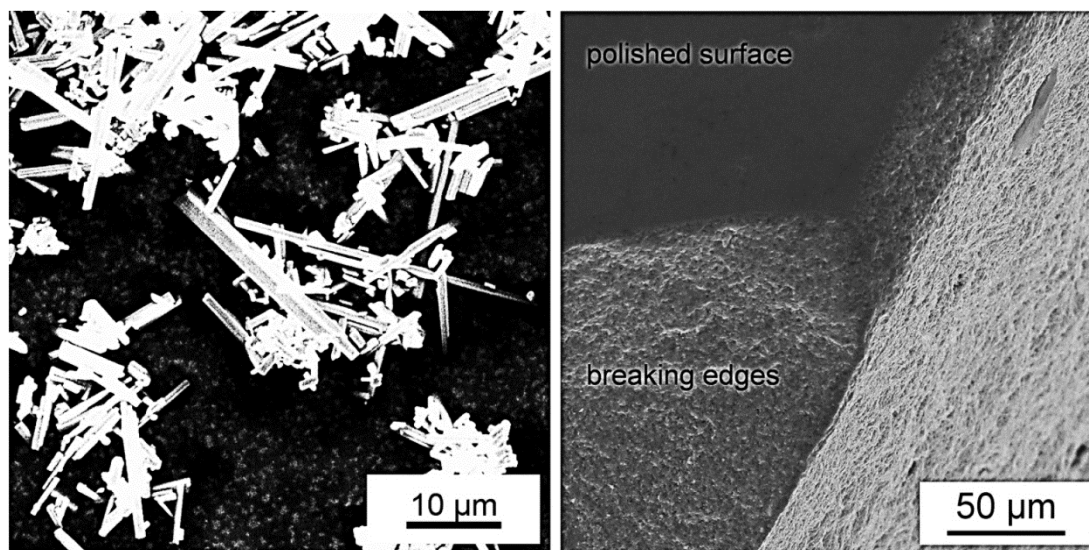

Figure 3.2: Scanning electron microscopy images of the as-synthesized powders (left) showing the needle-like shape of the crystals. The SEM pictures of the consolidated pellets (right) confirm the high obtained density of the samples.

The as-synthesized powders consisted of anisotropic match-like crystals with prismatic crystal habit, few micrometers in diameter and several micrometers in length. The consolidated pellets showed high density with only few cavities visible on the breaking edge. The polished surface showed no signs of contrast corroborating a homogeneous elemental distribution. No serious anisotropic contributions to the transport properties are expected, and therefore the consolidated pellets were used as such for further characterizations.

3.3.2   Structural characterization

Due to the large unit cell, complex structure, and low symmetry of the TTBs, structure refinement of the as-synthesized powders and consolidated pellets by the Rietveld method was not possible with standard laboratory X-ray diffraction data. Therefore, the computationally

simpler Le Bail fits were used to match the diffraction data. The refined diffraction data are shown in Figure 3.3.
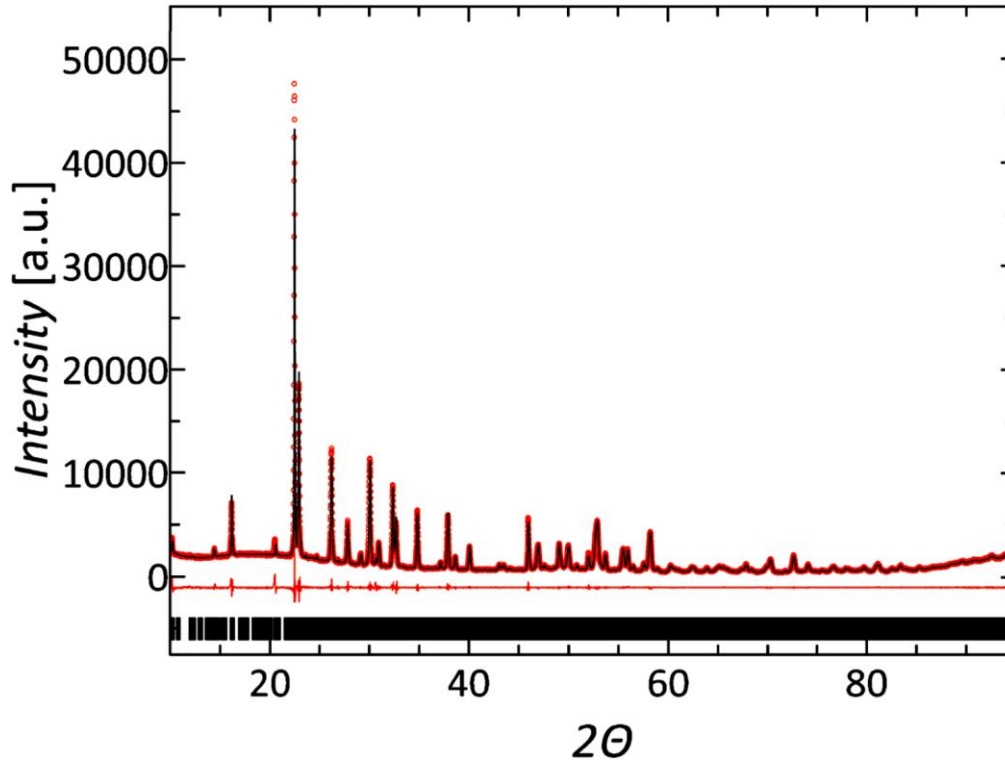

Figure 3.3: Le Bail fit for the powder diffraction data of $Nb_8W_9O_{47}$ (red dots), including profile fit (black solid line), and profile difference (red solid line). The refined Bragg's reflections are indicated by black ticks on the bottom part of the figure.

No structural changes were observed upon substitution, in agreement with the infinitely adaptive nature of the TTB. The data obtained from all as-synthesized samples and consolidated pellets could be fitted using the crystallographic structure model of $Nb_8W_9O_{47}$ with R_{wp} values < 5%. In addition, data obtained from consolidated samples and pellets, which were subsequently reduced or oxidized, showed no significant difference in structure within the experimental resolution limit.

The presence of prevalent oxygen defects was studied by HRTEM imaging. As-synthesized pellets of composition $Nb_8W_9O_{47}$ and $Nb_7W_{10}O_{47}$ were analyzed to investigate the influence of cation substitution on the micro- and nano-structure. In addition, an as-synthesized pellet of composition $Nb_8W_9O_{47}$ was cut into two pieces, which were subsequently either oxidized or reduced, to investigate the effect of oxygen deficiency on the structure. After oxidation the

sample color changed from dark gray to yellow/white, which indicates the absence of charge carriers corroborating the annihilation of oxygen vacancies.
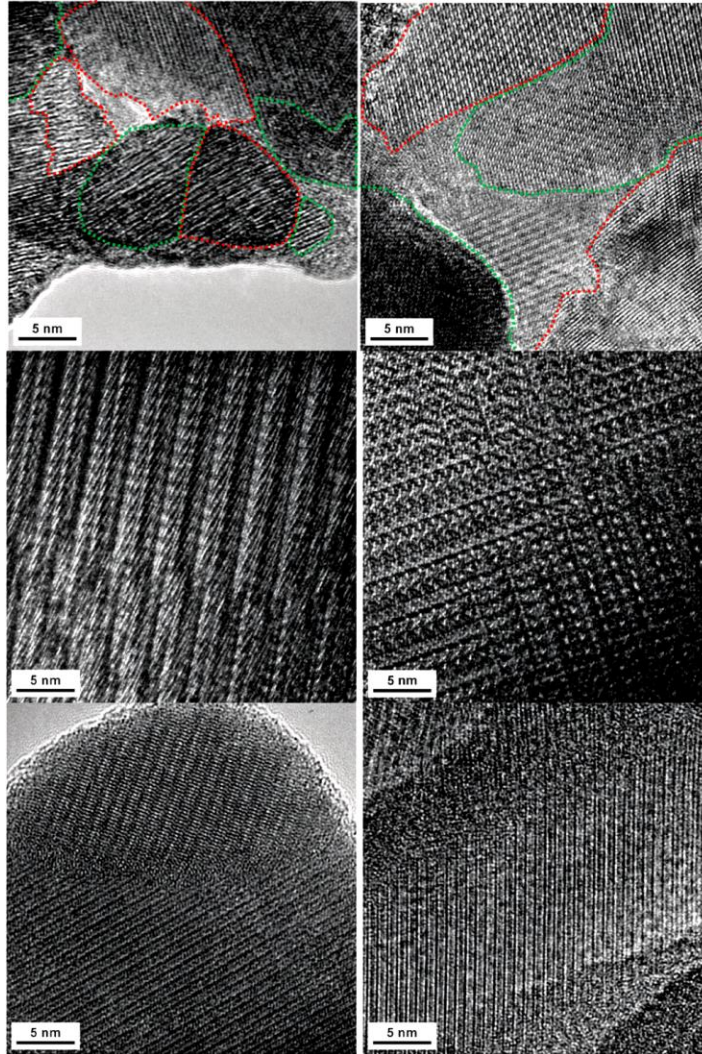

Figure 3.4: HRTEM micrographs, illustrating boundaries of different grain sizes marked with dashed lines (top), Wadsley defects (middle), and CS planes (bottom) found in sintered samples of different substitution degree and varying oxygen deficiency.

The HRTEM investigation revealed also that all samples – independently from the cation composition and the reduction state – contain a rich variety of defects, including point defects, Wadsley defects and CS planes. Additionally, a broad grain size distribution from a few nm to several μm was observed. An overview of different defects and grain sizes is shown in Figure 3.4. Due to the presence of both ordered CS planes and disordered grains of varying size, the

investigated TTB materials may be considered as nanostructured as well as nanoscaled materials. As a consequence, the lattice thermal conductivity is expected to be relatively low.

3.3.3 Thermal stability and oxygen deficiency

To obtain information on the thermal stability and the oxygen vacancy concentration at elevated temperatures, TG measurements under controlled atmospheres were conducted. Initially, the thermal stability was investigated under varying atmospheres. Enlarged sections of the TG run as a function of time can be seen in Figure 3.5.
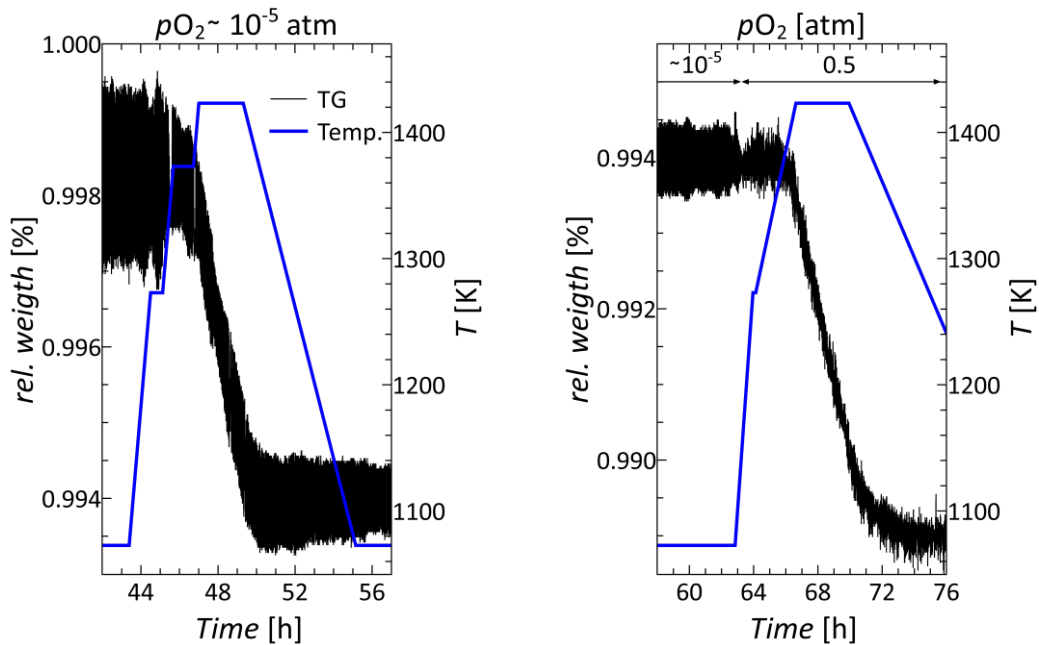
Figure 3.5: Relative weight of $Nb_8W_9O_{47}$ as a function of time at different temperatures and different oxygen partial pressures. The weight loss above 1373 K indicates an irreversible decomposition at both lower (left) and higher (right) oxygen partial pressures, probably associated with an evaporation of WO_3.

A slight initial weight loss of 0.2 % was encountered from room temperature up to 650 K, probably due to loss of adsorbed water. The measurement was conducted at pO_2 of 10^{-5} atm (left image in Figure 3.5) and 0.5 atm (right image in Figure 3.5), respectively. In both cases, the onset of an irreversible weight loss occurred at ≈ 1373 K, which is probably associated to the volatilization of WO_3. No weight gain was observed while increasing pO_2 at 1273 K (right

image in Figure 3.5), indicating no significant oxygen non-stoichiometry under these conditions. During the final cooling to room temperature, the pO_2 was again reduced to 10^{-5} atm at 920 K without any significant weight change. During this TG study, the sample color again had changed from dark gray to light yellow, due to the annihilation of oxygen vacancies. From these experiments, we conclude that the application of $Nb_{8-x}W_{9+x}O_{47}$ is limited to temperatures below 1373 K.

The residual oxygen partial pressure of argon ($pO_2 \approx 10^{-5}$ atm) was not low enough to cause reduction of the oxidized sample. Therefore, other more reducing gas mixtures were investigated as well to obtain higher reduction potentials. The use of wet H_2 as a reductive gas (pO_2 typically between 10^{-25} and 10^{-20} atm depending on temperature) did not lead to a reduction of $Nb_8W_9O_{47}$, but to sample decomposition, which could be verified by X-ray diffraction. Therefore, milder reducing gas mixtures were tested. A reduction of $Nb_8W_9O_{47}$ was possible with the use of a $CO/CO_2/Ar$ gas mixture. It was found that $Nb_8W_9O_{47}$ can be reduced at 1173 K and a $pO2$ of $\approx 10^{-15}$ atm, while preserving the overall TTB structure. Due to the weight loss correlated to oxygen vacancy formation, the reduction can be monitored gravimetrically. The subtle structural changes correlated with the defect formation, although detectable in the HRTEM images, could not be resolved by standard laboratory X-ray diffraction. Figure 3.6 shows the reversible weight loss and gain, associated with the reduction and oxidation of an as-synthesized $Nb_8W_9O_{47}$ sample.
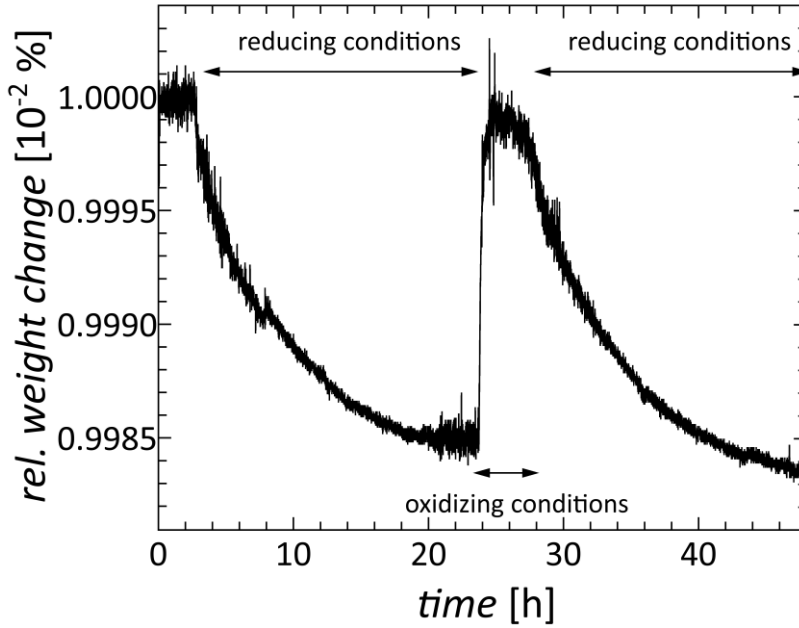
Figure 3.6: Redox reaction of $Nb_8W_9O_{47-\delta}$ monitored by thermogravimetric analysis. pO_2 was varied between $\approx 10^{-15}$ atm (reducing conditions) and 10^{-5} atm (oxidizing conditions) with the use of $CO/CO_2/Ar$ or O_2/Ar gas mixtures at 1173 K. A maximum oxygen deficiency of $\delta = 0.3$ was calculated.

The oxidation reaction is much faster than the reduction, demonstrated by the rapid weight gain at $t \approx 24$ h. The reduction - oxidation cycle was reversible and could be repeated without any sign of sample degradation. By thermal quenching to room temperature, the oxygen vacancy and the corresponding charge carrier concentrations could be preserved. Assuming a completely oxidized sample ($\delta = 0$) before reduction, the monitored relative weight loss of 0.15 % can be translated to an oxygen deficiency δ of 0.3 in $Nb_8W_9O_{47-\delta}$. Each oxygen vacancy donates two electrons therefore the effect of the maximum oxygen deficiency of 0.3 on the thermoelectric properties should be comparable to a substitution degree of $x = 0.6$.

3.3.4   TE properties and optimization strategies

Starting from non-substituted, fully oxidized $Nb_8W_9O_{47}$, the charge carrier concentration must be increased to enhance the thermoelectric properties. An increase of the charge carrier concentration can be achieved either by cation substitution or, to a lower extent, by an increase of the oxygen vacancy concentration. To obtain a first assessment of the thermoelectric potential, a series of cation substituted compounds with compositions $Nb_{8-x}W_{9+x}O_{47}$, $x = 0$,

0.075, 0.1, 1, and 2 was investigated for the thermoelectric transport properties. The results of the electronic transport measurements are plotted in Figure 3.7.
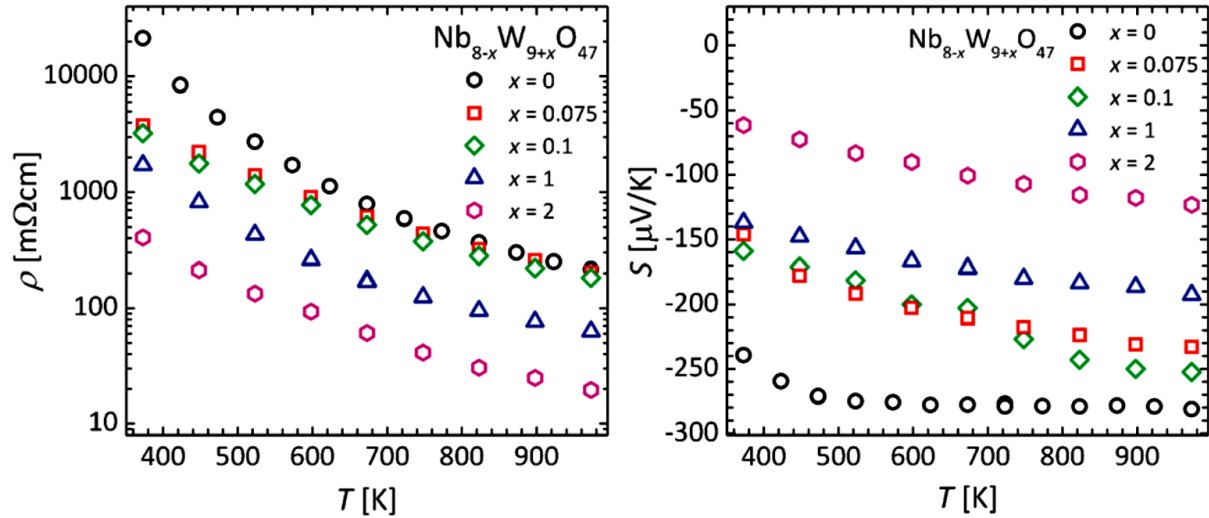

Figure 3.7: Temperature dependence of the electrical resistivity ρ (left) and the Seebeck coefficient S (right) of $Nb_{8-x}W_{9+x}O_{47}$ for different cation substitution levels x (x = 0, 0.075, 0.1, 1 and 2). From the plots can be observed how the cation substitution, with the consequent increase of the charge carrier concentration, affects the electronic properties.

The overall electrical resistivity of the samples was high compared to other thermoelectric materials, but it decreased considerably with rising temperature, probably due to a higher degree of charge carrier delocalization at high temperature. Since W has a higher electron count compared to Nb, an increasing degree of substitution leads to a higher charge carrier concentration and consequently to a lower electrical resistivity, reaching a value of 20 mΩcm at 973 K for a sample of composition $Nb_6W_{11}O_{47}$. The samples with a lower degree of substitution (x = 0, 0.075, 0.1), however, exhibit a similar electrical resistivity. A possible reason for this may be the dominating influence of oxygen vacancies on the charge carrier concentration at lower substitution degree.

In line with the high electrical resistivity, the measured Seebeck coefficients are rather large. At room temperature the Seebeck values range from -240 to -65 μVK^{-1} for samples of composition $Nb_8W_9O_{47}$ and $Nb_6W_{11}O_{47}$, respectively. This corroborates the assumption of an n-type material with a charge carrier concentration increasing with an increasing substitution level. All substituted samples showed an increase of the thermopower with increasing

temperature, probably due to an increase of the internal overall entropy of the system at higher temperatures. However, further studies are needed to fully understand the underlying principles of the electronic transport properties of the tungsten bronzes. When substituting niobium by tungsten, or when creating oxygen vacancies, the change in all transport parameters can be understood by a variation in the charge carrier concentration.
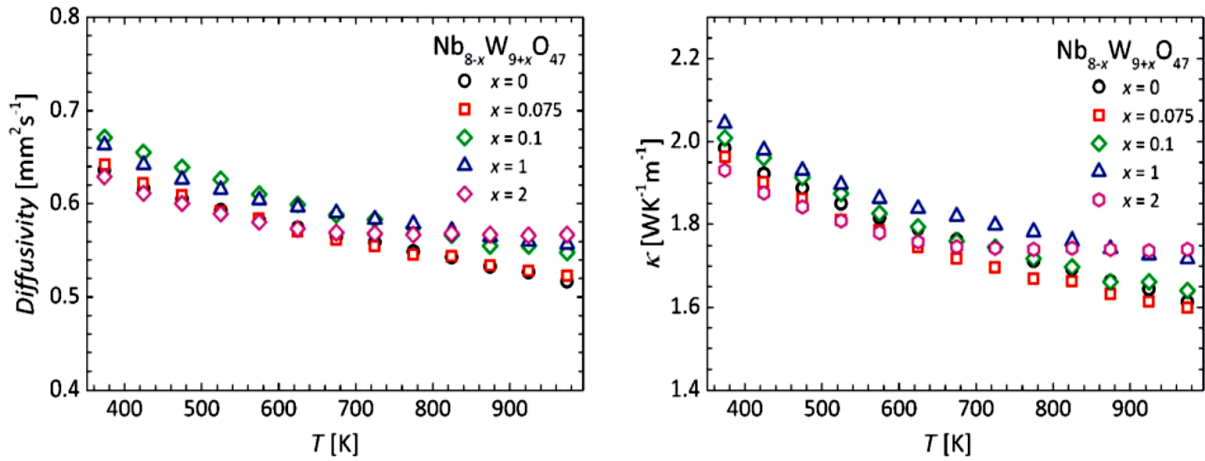

Figure 3.8: Temperature dependence of the thermal diffusivity (left) and thermal conductivity (right) in cation substituted TTBs of composition $Nb_{8-x}W_{9+x}O_{47}$ with $x = 0, 0.075, 0.1, 1,$ and 2.

The measured thermal diffusivities and calculated thermal conductivities of the cation-substituted series of TTBs are shown in Figure 3.8. The thermal diffusivity values of all samples are very similar to each other. Beside a subtle increase upon substitution, no clear trend was observed. With increasing temperature, the thermal diffusivity decreases slightly. The obtained thermal conductivities are all low, with values ranging from 1.6 to 2.0 $Wm^{-1}K^{-1}$ for the unsubstituted and substituted samples, respectively. The glass-like thermal conductivities can be attributed to the nano-sized grains and the complex disordered structure,[23] and are similar to values reported for other niobium tungsten compounds.[24] The similar thermal conductivities for all samples can be rationalized as (i) the structure of the TTB does not change upon substitution, (ii) the change in mass contrast (from 8:9 to 7:10 for $Nb_{8-x}W_{9+x}O_{47}$ with $x = 0$ and 2) is only moderate, and (iii) strain contrast should be low considering the ionic radii (0.64 and 0.60 Å) of Nb^{5+} and W^{6+} in octahedral coordination.[25] Due to the high electrical resistivity, the electronic contribution to the thermal conductivity is negligible for all studied compositions. Using these initial measurements, the power factor and

the thermoelectric figure of merit of the cation substituted series were calculated. The results are summarized in Figure 3.9.
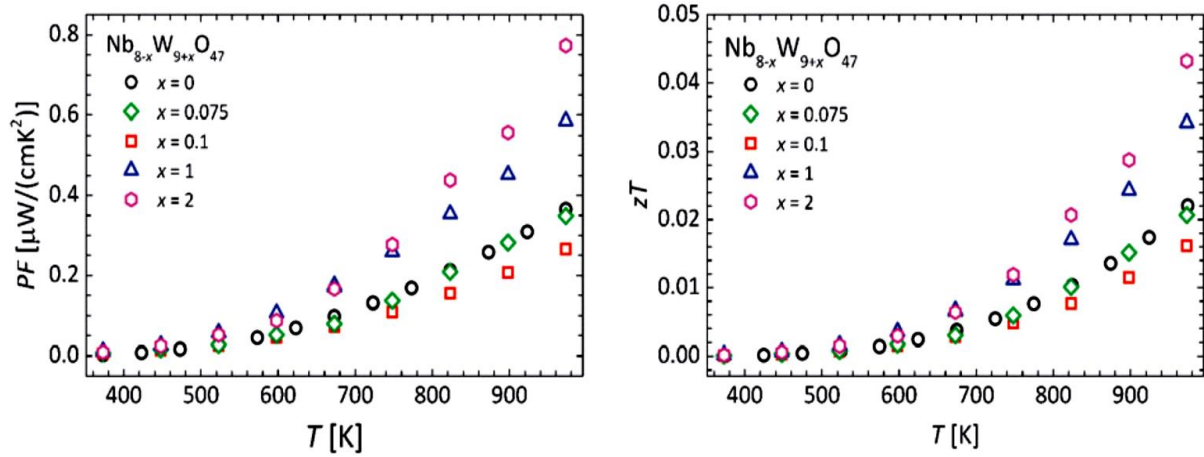

Figure 3.9: Temperature dependence of the power factor *PF* (left) and the figure of merit *zT* (right) in function of the cation substitution degree in tetragonal tungsten bronzes $Nb_{8-x}W_{9+x}O_{47}$ with $x = 0$, 0.075, 0.1, 1, and 2. The figure illustrates the trend of increasing power factor and figure of merit with increasing substitution degree.

As a consequence of the rather high electrical resistivity, the power factor is not very large, but increases with rising temperature and substitution degree. Indeed, a substantial increase of the power factor up to a value of 0.8 mWcm^{-1}K^{-2} at 973 K could be obtained for the composition $Nb_6W_{11}O_{47}$ with respect to the lower substituted samples. This trend is also reflected in the thermoelectric figure of merit, where a value of 0.043 was reached at 973 K for the highest substituted sample studied in this contribution ($x = 2$). In comparison to state of the art optimized *n*-type thermoelectric oxide materials, the figure of merit is still lower by a factor of ten. However, in this initial study, TTBs with a maximal substitution level of $x = 2$ have been investigated, although substitution levels of up to $x = 5$ ($Nb_3W_{14}O_{47}$) are reported in literature without significant structural changes. With increasing substitution level, the electrical properties are expected to improve even more, while keeping a similar low thermal conductivity. Therefore, the figure of merit is expected to be enhanced further with increasing substitution level.

In addition to cation substitution, a second optimization strategy contemplates the manipulation of the charge carrier concentration and the phonon scattering centers by acting on the oxygen deficiency. Indeed, an oxygen vacancy acts as a donor of two electrons to the

86

system. As previously shown, the oxygen content of $Nb_{8-x}W_{9+x}O_{47}$ can reversibly be varied at elevated temperatures by controlling the atmospheric composition (see Figure 3.6). In order to demonstrate that the control of the oxygen deficiency corroborates the control of the electronic properties, a simple experiment was conducted. A sample of composition $Nb_8W_9O_{47}$ was repeatedly reduced and oxidized over three cycles under controlled, almost identical thermodynamic conditions (temperature, pO_2) while monitoring the weight change. After equilibrium had been reached, the sample was quenched to room temperature. The corresponding electronic properties were determined after each cycle. In the oxidized state the color was white/slightly yellow. The sample resistivity was very high and could not be determined with our setup. In the reduced state, the sample was dark blue in color. The results of the electronic transport measurements after each red/ox-cycle are shown in Figure 3.10.
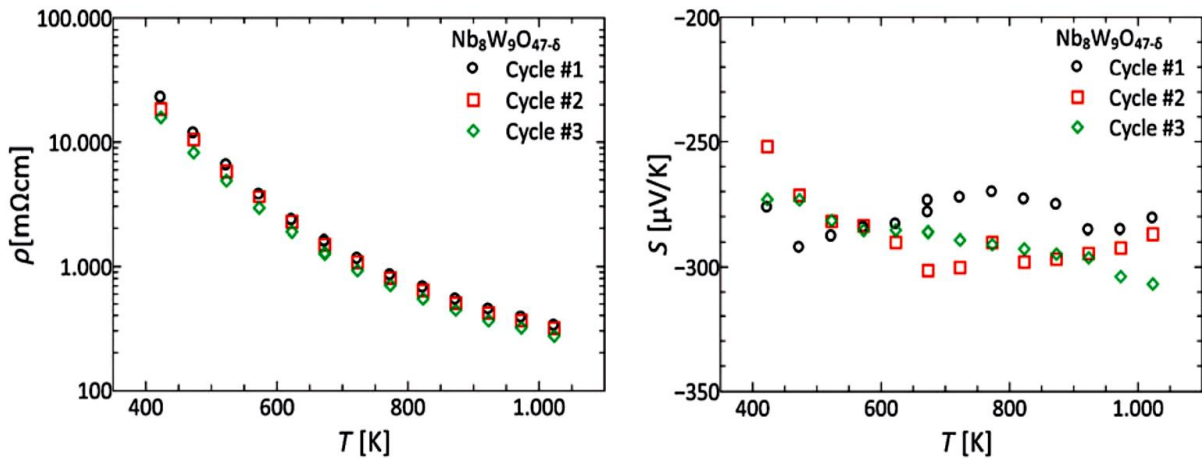

Figure 3.10: Electrical resistivity ρ (left) and Seebeck coefficient S (right) after controlled oxidization and reduction cycles. The measurements were performed in the reduced state, after the first, second and third redox cycle. The good reproducibility of the electronic properties illustrates the good control of the oxygen defect concentration, and hence the charge carrier concentration.

In consideration of the substantial changes from the white, oxidized, insulating sample to the dark blue, reduced, semiconducting sample, the measured electronic properties are very similar. The measured electrical resistivity and the Seebeck coefficients in the three cycles are reproducible within a relative error of 17% and 7%, respectively, and they are within the limits of reproducibility based on a round-robin testing of transport properties of bulk thermoelectrics.[26,27] The variation may be caused by changes in the nanostructure or slightly different oxygen vacancy concentrations after each quenching. However, it is evident that

control of the oxygen non-stoichiometry and the associated charge carrier concentration can be achieved. Analogue to the electronic properties no significant variation of the thermal conductivity upon oxidation/reduction cycling has been noted. These outcomes confirm that the control of oxygen vacancies can be considered as a viable further optimization strategy for tetragonal tungsten bronzes and even other thermoelectric oxides.

3.4　Summary

A first assessment of tetragonal tungsten bronzes as thermoelectric energy conversion materials was conducted. They were chosen because of their structural complexity and their possible electronic tuning by cation substitution x and oxygen deficiency δ. To this end, a series of compounds with low substitution degree $x = 0, 0.075, 0.1, 1,$ and 2, was synthesized and characterized structurally by X-ray diffraction and high-resolution transmission electron microscopy. In view of thermoelectric transport measurements, optimal sintering parameters, thermal stability and redox behavior at elevated temperatures were investigated.

The materials exhibit a complex atomic structure. HRTEM investigations revealed varying grain sizes down to few nanometers and a variety of different oxygen defects, including point defects, Wadsley defects and crystallographic shear planes.

The oxygen deficiency δ could be reversibly controlled by equilibrating the sample in a controlled atmosphere at 1173 K with subsequent quenching. Due to the reversible generation and annihilation of oxygen vacancies at elevated temperatures, the electronic properties can be tuned to some extent. A maximum oxygen deficiency of $\delta = 0.3$ was determined for $Nb_8W_9O_{47-\delta}$, corresponding to a change in substitution degree of $x = 0.6$.

Thermoelectric transport measurements were conducted up to 973 K under controlled atmosphere to prevent a change of the oxygen stoichiometry during measurements. All samples exhibited a relatively high electrical resistivity above 20 mΩcm and high negative Seebeck coefficients ranging from -280 to -65 μVK^{-1}, indicating n-type conduction. With increasing degree of substitution, charge carriers are introduced into the system. This leads to an increase of the electric conductivity and a decrease of the thermopower. The complex structure composed of nano-sized grains, and a high concentration of various defects results in glass-like thermal conductivities ranging from 1.6 to 2.0 Wm^{-1}K^{-1}. The highest power factor and zT were obtained for the highest substituted sample ($Nb_6W_{11}O_{47}$) with values of 0.8 mWcm^{-1}K^{-2} and 0.043, respectively, at 973 K. Although the obtained figure of merit is lower than in other optimized n-type oxides, the high Seebeck coefficient paired with the low thermal conductivity demonstrates the potential of tetragonal tungsten bronzes for thermoelectric applications.

Both optimization strategies, (i) cation substitution and (ii) controlled oxygen deficiency proved their suitability to tailor the thermoelectric properties. With increasing degree of substitution, significant further improvement of the figure of merit are expected."

References

[1]   C. P. Heinrich, M. Schrade, G. Cerretti, I. Lieberwirth, P. Leidich, A. Schmitz, H. Fjeld, E. Mueller, T. G. Finstad, T. Norby, et al., *Mater. Horiz.* **2015**, *2*, 519–527.

[2]   K. Koumoto, Y. Wang, R. Zhang, A. Kosuga, R. Funahashi, *Annu. Rev. Mater. Res.* **2010**, *40*, 363–394.

[3]   J. He, Y. F. Liu, R. Funahashi, *J. Mater. Res.* **2011**, *26*, 1762–1772.

[4]   I. Terasaki, Y. Sasago, K. Uchinokura, *Phys. Rev. B* **1997**, *56*, R12685–R12687.

[5]   P. Limelette, V. Hardy, P. Auban-Senzier, D. Jérome, D. Flahaut, S. Hébert, R. Frésard, C. Simon, J. Noudem, A. Maignan, *Phys. Rev. B - Condens. Matter Mater. Phys.* **2005**, *71*, 1–5.

[6]   H. Yamauchi, L. Karvonen, T. Egashira, Y. Tanaka, M. Karppinen, *J. Solid State Chem.* **2011**, *184*, 64–69.

[7]   F. Li, T.-R. Wei, F. Kang, J.-F. Li, *J. Mater. Chem. A* **2013**, *1*, 11942–11949.

[8]   T. Tsubota, M. Ohtaki, K. Eguchi, H. Arai, *J. Mater. Chem.* **1997**, *7*, 85–90.

[9]   H. Ohta, W.-S. Seo, K. Koumoto, *J. Am. Ceram. Soc.* **1996**, *79*, 2193–2196.

[10]   H. Ohta, W.-S. Seo, K. Koumoto, *J. Am. Ceram. Soc.* **1996**, *79*, 2193–2196.

[11]   T. Tani, S. Isobe, W.-S. Seo, K. Koumoto, *J. Mater. Chem.* **2001**, *11*, 2324–2328.

[12]   D. Bérardan, E. Guilmeau, A. Maignan, B. Raveau, *Solid State Commun.* **2008**, *146*, 97–101.

[13]   K. H. Lee, S. W. Kim, H. Ohta, K. Koumoto, *J. Appl. Phys.* **2006**, *100*, 63717.

[14]   E. Guilmeau, D. Bérardan, C. Simon, A. Maignan, B. Raveau, D. O. Ovono, F. Delorme, *J. Appl. Phys.* **2009**, *106*, 53715.

[15]   F. Krumeich, A. Hussain, C. Bartsch, R. Gruehn, *Anorg. Allg. Chem.* **1995**, *621*, 799–

806.

[16]   F. Krumeich, C. Bartsch, R. Gruehn, *J. Solid State Chem.* **1995**, *427*, 420–427.

[17]   F. Krumeich, M. Wörle, A. Hussain, *J. Solid State Chem.* **2000**, *149*, 428–433.

[18]   D. C. Craig, N. C. Stephenson, *Acta Crystallogr. Sect. B Struct. Crystallogr. Cryst. Chem.* **1969**, *25*, 2071–2083.

[19]   T. NORBY, *Solid State Ionics* **1988**, *28–30*, 1586–1591.

[20]   M. Schrade, H. Fjeld, T. G. Finstad, T. Norby, *J. Phys. Chem. C* **2014**, *118*, 2908–2918.

[21]   M. Schrade, H. Fjeld, T. Norby, T. G. Finstad, *Rev. Sci. Instrum.* **2014**, *85*, 103906-1–8.

[22]   D. R. Salmon, R. P. Tye, *Int. J. Thermophys.* **2010**, *31*, 338–354.

[23]   F. Krumeich, *Acta Crystallogr. Sect. B Struct. Sci.* **1998**, *54*, 240–249.

[24]   I. Henning, M. Mertig, R. Plath, G. Pompe, E. Heganbarth, R. Schalge, *Phys. Status Solidi* **1982**, *73*, K105–K109.

[25]   A. Simon, *Angew. Chemie Int. Ed. English* **1983**, *22*, 95–113.

[26]   H. Wang, W. D. Porter, H. Böttner, J. König, L. Chen, S. Bai, T. M. Tritt, A. Mayolet, J. Senawiratne, C. Smith, et al., *J. Electron. Mater.* **2013**, *42*, 654–664.

[27]   H. Wang, W. D. Porter, H. Böttner, J. König, L. Chen, S. Bai, T. M. Tritt, A. Mayolet, J. Senawiratne, C. Smith, et al., *J. Electron. Mater.* **2013**, *42*, 1073–1084.

The content of the following chapter is taken and partially adapted from the contribution *J. Mat. Chem. A.* **2016**, submitted. This project was developed in collaboration with the Centre for Materials Science and Nanotechnology at the University of Oslo (FERMIO).

Authorship contributions

Category 1

Conception and design of study:

G. Cerretti, W. Tremel.

Acquisition of data:

G. Cerretti – preparation of samples.

G. Cerretti – PXRD refinement.

G. Cerretti – measurement of the thermoelectric properties (Mainz data) and Hall measurements.

G. Cerretti, B. Balke – DSC measurements.

M. Schrade, X. Song – measurements of the thermoelectric properties (Oslo data).

I. Lieberwirth – HRTEM micrographs.

Analysis and/or interpretation of data:

G. Cerretti, M. Schrade, B. Balke.

Category 2

Drafting the manuscript: G. Cerretti.

Revising the manuscript critically for important intellectual content: M Schrade, X. Song, B. Balke, M. Panthöfer, T. Norby, W. Tremel.

Category 3

Approval of the version of the manuscript to be published:

G. Cerretti, M. Schrade, X. Song, B. Ballke, M. Panthöfer, I. Lieberwirth, T. Norby, W. Tremel.

FIGURE 4.1: PREPARED BY G. CERRETTI.
FIGURE 4.2: PREPARED BY I. LIEBERWIRTH.
FIGURE 4.3: PREPARED BY G. CERRETTI.
FIGURE 4.4: PREPARED BY G. CERRETTI.
FIGURE 4.5: PREPARED BY G. CERRETTI.
FIGURE 4.6: PREPARED BY G. CERRETTI.
FIGURE 4.7: PREPARED BY G. CERRETTI.
FIGURE 4.8: PREPARED BY G. CERRETTI.

4 Thermal stability and TE properties of the highly substituted samples of the TTB series $Nb_{8-x}W_{9+x}O_{47}$ $(3 \leq x < 5)$

4.1 Motivation

The ideal thermoelectric material possesses the electronic properties of a crystal combined with a glass-like thermal conductivity "phonon-glass electron-crystal").[1] The optimization of the thermoelectric materials is restricted by the interdependent thermal and electric transport properties.

Most oxides have narrow bands and therefore exhibit low charge carrier mobilities and large effective masses $m*$.[2–5] In addition, their high intrinsic thermal conductivity arising from the small atomic mass of oxygen and the strong bonding associated with large electronegativity differences in electronegativity is detrimental to thermoelectric applications. As a result, metal oxides remained mostly unrecognized as thermoelectrics, until a large thermopower was observed in Na_xCoO_2.[6] This led to a surge of activities on cobaltites[7–14] (and oxides in general[15–20]) for thermoelectrics. In parallel the thermoelectric performance of oxides was improved steadily. First studies on metal oxides with adaptive structures like Magnéli phases revealed that it is possible to overcome the shortcomings of oxides, because the charge carrier density can be tuned through the oxidation state of the metals and the thermal conductivity can be reduced through the shear elements and the structural complexity.[21] The concept underlying the use of Magnéli phases is based on the intrinsic, layered nanostructure defined by crystallographic shear (CS) planes as structure motifs.[22–37] This allows reducing the thermal conductivity through CS in a first step, thereby approaching the problem by starting

with a material with a low thermal conductivity, and then increasing its power factor by adjusting the carrier concentration by changing the oxidation state of the metal.[38]

The structures of many ternary compounds of early transition metal oxides show CS planes.[39] This underlines the tendency of different transition metals to adopt an octahedral coordination. The TTBs $Nb_{8-x}W_{9+x}O_{47}$ are another illustrative example. The structure of the TTBs with x ranging from 0 to 5 was studied first by Krumeich et al.[40–43] In the pseudo-binary system Nb_2O_5/WO_3, $Nb_8W_9O_{47}$ is the end member of a solid solution series $Nb_{8-x}W_{9+x}O_{47}$ ($0 \leq x \leq 5$), where Nb^{5+} ions are formally substituted by Nb^{4+} (or W^{4+}) and W^{6+} ions. Its crystal structure is based on corner sharing WO_6 octahedra forming pentagonal tunnels that are partially filled by Nb atoms with pentagonal bipyramidal coordination (inset of Figure 4.1). TTBs have large complex unit cells with anisotropic atomic bonding and high atomic mass. These characteristics in combination with a nanostructure defined by intrinsic crystallographic shear planes reduce the thermal conductivity dramatically, which allowed applications for thermal barrier coatings. Moreover, an independent manipulation of the charge carrier concentration is possible, without significant structural changes,[40] by substituting Nb^{5+} on the cation site according to $2Nb^{5+} \rightarrow M^{4+} + W^{6+}$ ($M^{4+}=Nb^{4+}$ or W^{4+}), i.e. all substituted variants have n-type properties. In the previous chapter the potential of TTBs for thermoelectrics[44] in the range $0 \leq x \leq 2$ is sketched.

In this chapter, the synthesis, the thermal stability and thermoelectric properties of TTBs with the highest degree of substitution, $Nb_5W_{12}O_{47}$ ($x = 3$), $Nb_4W_{13}O_{47}$ ($x = 4$), and $Nb_3W_{14}O_{47}$ ($x = 5$) are described. The reliability of the thermoelectric transport data was validated by using different testing methods and instrument types in the two partner laboratories. Over the full temperature range, the measurement discrepancies for the figure of merit zT were within the 10% from the averages.

4.2 Experimental

4.2.1 Materials and methods

Samples of $Nb_{8-x}W_{9+x}O_{47}$ (x = 3, 4, 5) were synthesized from NbO_2 (abcr, 99%), Nb_2O_5 (ChemPur, 99.98+%), and WO_3 (Alfa Aesar, 99.8%). The starting compounds were weighted in stoichiometric amounts and carefully mortared to obtain homogeneous mixtures. The prepared powders were loaded in quartz ampules that were evacuated subsequently. The reaction was carried out in a tubular furnace for three days at 1423 K. In this way polycrystalline samples with stoichiometric compositions $Nb_5W_{12}O_{47}$, $Nb_4W_{13}O_{47}$ and $Nb_3W_{14}O_{47}$ were prepared. For compaction, the obtained powders were loaded in a 20 mm diameter graphite die. In order to avoid contamination, the internal surfaces of the die were covered with a carbon foil. The compaction was carried out in a spark plasma sintering furnace (FCT Systeme GmbH - SPS Furnace HP D 25) by applying an uniaxial pressure of 50 MPa and heating the samples at 1273 K for 5 minutes. Once the samples were cooled down to room temperature, the pellets were carefully polished to remove the residues of the external carbon substrate. While pellets containing single phase $Nb_5W_{12}O_{47}$ and $Nb_4W_{13}O_{47}$ could be prepared, samples of $Nb_3W_{14}O_{47}$ showed decomposition to x = 4 and WO_3. Further attempts have been done varying the reaction temperature and the stoichiometric amount of the sample, but they always led to the same result.

4.2.2 Characterization

Powder X-ray diffraction (PXRD) was used to check the purity of the samples before and after SPS compaction on a Siemens D5000 diffractometer in transmission geometry, equipped with a Braun M50 detector, Cu Kα radiation with a Ge monochromator and a step size of 0.0078 in 2Θ. Samples with suitable shapes for thermoelectric measurements were cut with a linear precision diamond blade saw (Buehler IsoMet 4000). The remaining parts of each pellet were used for SEM, HRTEM, and DSC studies.

To verify the reproducibility of the measurements and the stability of the materials, a complete thermoelectric characterization of the samples was carried out on two different sets of machines.

At the Centre for Materials Science and Nanotechnology at the University of Oslo (FERMIO) all thermoelectric properties were measured on one single sample with dimensions 10 x 10 x 1.5 mm^3. First, the electrical conductivity and the Seebeck coefficient were measured using a custom-built assembly mounted onto a NorECs ProboStat measurement cell.[45,46] During the measurement the sample chamber was flushed with a constant Ar flux. The thermal diffusivities were measured in a N$_2$ atmosphere on a Netzsch LFA micro flash 457. The samples were previously coated with a thin homogeneous graphite layer in order to standardize absorption and emission properties.

A second characterization was carried out at the Johannes Gutenberg Universität Mainz. The Seebeck coefficient and the electrical resistivity were measured simultaneously on a bar shaped sample (2 x 1.5 x 10 mm) using a four point method under a He atmosphere on a Linseis LSR-3 machine. For the evaluation of the thermal diffusivity on a square sample (10 x 10 x 1.5 mm^3), a Netzsch LFA micro flash 457 with an Ar atmosphere was used. From the thermal diffusivity, the thermal conductivity was computed using the formula $\kappa = D C_p d$, where D is the thermal diffusivity in mm^{2}s^{-1}, C_p is the specific heat in Jg^{-1}K^{-1}, and d is the density in gcm^{-3} of the sample. The values of the heat capacity were measured on DSC (Netzsch DSC 204 F1 Phoenix) under an Ar atmosphere. Simultaneously, the device was used to analyze the thermal stability of the samples when subjected to several heating-cooling cycles through the analysis of the measured DSC signals.

A IPM-HT-Hall-900K system developed at the Fraunhofer Institute for Physical Measurement Techniques (IPM) was used to measure in a He atmosphere the charge carrier densities and the carrier mobility of the samples. This device uses a four contact setup to perform the measurement by the van der Pauw method.[47,48]

A FEI Nova NanoSEM600 equipped with an Everhart-Thornley detector (ETD) and a low voltage high contrast detector (vCD), and a FEI Tecnai F20 were used for acquiring the scanning electron microscopy (SEM) and high-resolution transmission electron microscopy (HRTEM) micrographs. SEM analyses were done on a finely polished piece of the SPS

sintered pellets; for the HRTEM investigation 1-10 nm thick slices of the same pellets were used.

4.3   Result and discussion

4.3.1   Structural characterization

Starting from NbO_2, Nb_2O_5, and WO_3 powders mixed in stoichiometric amounts, we synthesized samples of the TTB series $Nb_{8-x}W_{9+x}O_{47}$, the $Nb_5W_{12}O_{47}$ ($x = 3$) and $Nb_4W_{13}O_{47}$ ($x = 4$) with the highest degree of substitution. Krumeich et al.[40] studied the structure of single crystalline samples with a substitution level of $x = 5$. However, our attempts to obtain compacted bulk samples with compositions between $Nb_4W_{13}O_{47}$ and $Nb_3W_{14}O_{47}$ ($x = 4$ - 5) resulted in the formation of multi-phase mixtures. This indicates that the limit for the substitution in bulk materials is reached close to $x = 4$.

A Rietveld refinement of the measured profiles was not possible due to the complexity of the compounds deriving from the large unit cell, the intricate structure, and the low symmetry. Therefore, the refinement was performed using the computationally simpler Le Bail method to fit the diffraction data with the crystallographic data reported in literature.[40] The compositions $x = 3$ and 4 had a high purity even when the reaction was scaled up to several grams. Refinements made on PXRD data collected from both, powders and compacted samples showed good agreement with the theoretical profile ($X^2 < 3\%$; R_B and $R_F < 0.2$, Figure 4.1). In general, the X-ray patterns of unsubstituted $Nb_8W_9O_{47}$ ($x = 0$) and substituted $Nb_4W_{13}O_{47}$ ($x = 4$) showed only minor differences, i.e. the substitution of 2 Nb^{5+} by Nb^{4+} and W^{6+} (or W^{4+} and W^{6+}) induces only small structural changes to the crystal structure.
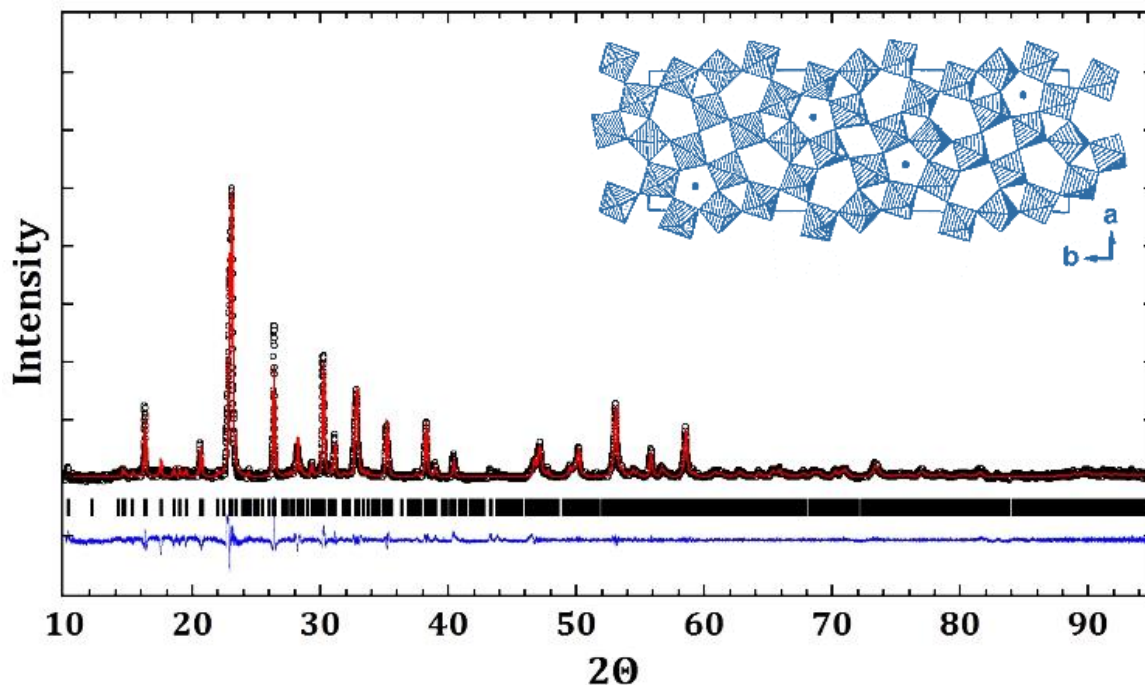
Figure 4.1: Le Bail fit of the PDXR pattern of $Nb_4W_{13}O_{47}$. The black dots are the measured points and the red line is the theoretical pattern calculated from the crystallographic data reported in literature.[40] Under the profile the refined Bragg's reflections (solid black lines) and the difference (solid blue line) between the measured and the calculated profiles are shown. The inset shows the unit cell of the TTBs.

Parts of the pellets of both $Nb_5W_{12}O_{47}$ ($x = 3$) and $Nb_4W_{13}O_{47}$ ($x = 4$) were cut for HRTEM studies. They revealed a multi-domain composition and a grain size distribution between the nano- and micro-scale (Figure 4.2c). Different kind of defects are present: point defects, discontinuities, Wadsley defects and crystallographic shear (CS) planes are clearly visible for all samples (Figure 4.2). No significant differences in the grain size nor in the defect distribution could be observed when the stoichiometric composition was changed. Both the CS and the presence of defects are believed to be the responsible of the low thermal conductivity of the TTBs. It has been shown before that more than the 80% of the heat is transported by phonons with a mean free path < 100 nm.[49]
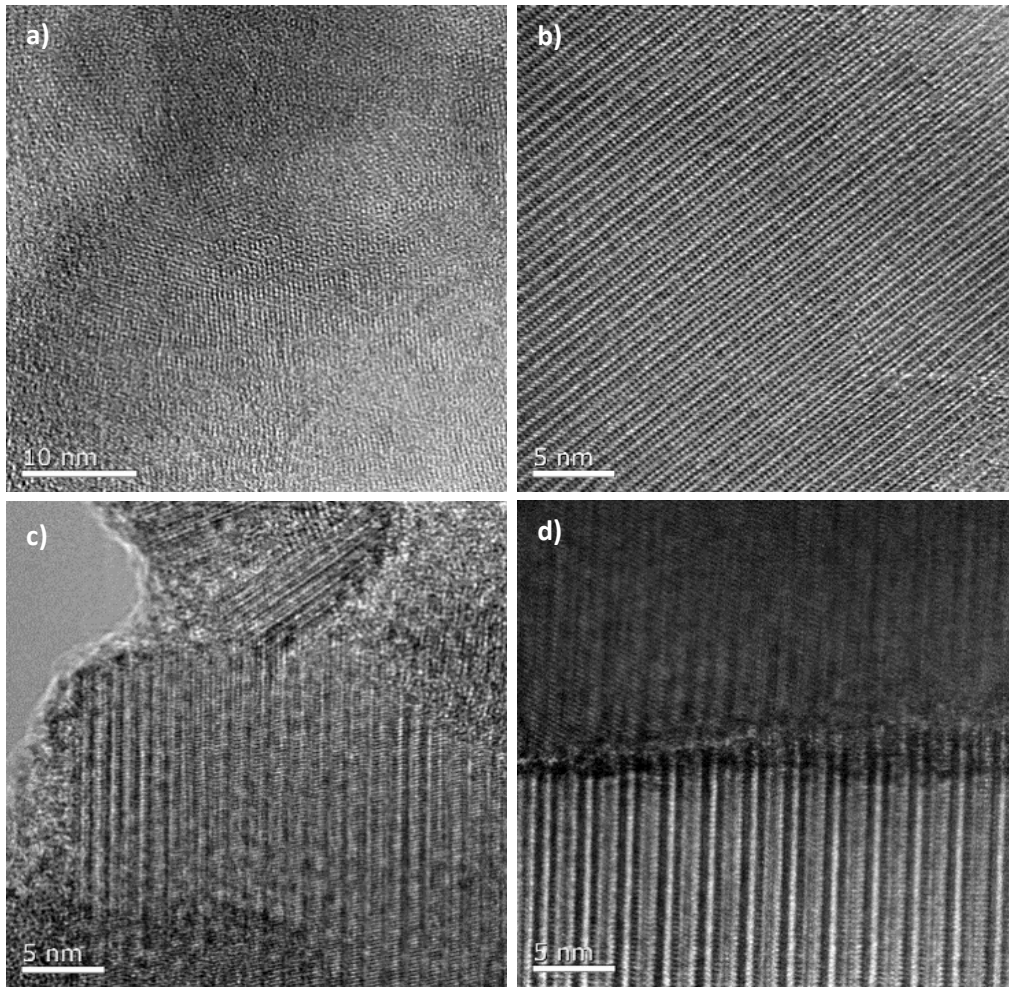
Figure 4.2: HRTEM micrographs of $Nb_4W_{13}O_{47}$. A whole booklet of defects can be observed, such as point defects in (a), Wadsley defects and CS planes in (b), the nano-scaled size of the grains and the different orientation of the defects in (c), and discontinuities in (d).

4.3.2   Thermal stability and thermoelectric properties

Before thermoelectric characterization, the sintered samples were subjected to heating-cooling cycles up to 873 K in a DSC to verify their stability. The maximum temperature was imposed by the testing range of the instrument. Figure 4.3 shows a consistent trend and consistent results (with deviations < 3%) for the thermal analysis of $Nb_5W_{12}O_{47}$ and $Nb_4W_{13}O_{47}$. Similar results were obtained for the heat capacity. The maximum values of C_p were 0.43 $Jg^{-1}K^{-1}$ and 0.48 $Jg^{-1}K^{-1}$ for $Nb_5W_{12}O_{47}$ ($x = 3$) and $Nb_4W_{13}O_{47}$ ($x = 4$), respectively (Figure 4.3c and d).
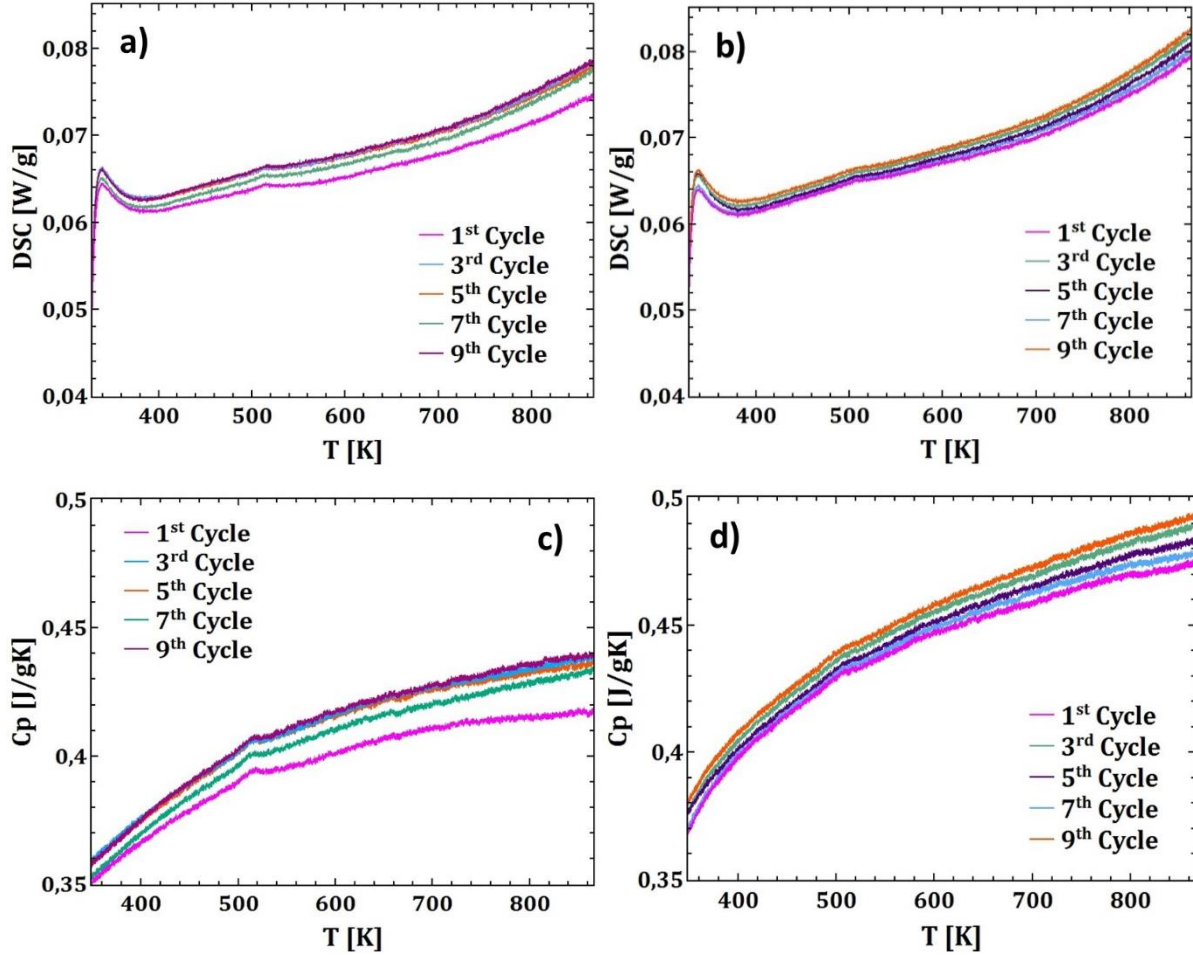
Figure 4.3: DSC measurement of parts of the sintered pellets undergoing thermal cycling. The measurements have been performed in the temperature range 323 - 873 K. The top plots show the measured DSC signals for the samples with composition $Nb_5W_{12}O_{47}$ (a) and $Nb_4W_{13}O_{47}$ (b). The bottom plots show the measured C_p values for the two characterized samples. The reported values are relative to the samples with composition $Nb_5W_{12}O_{47}$ (c) and $Nb_4W_{13}O_{47}$ (d).

In order to validate the measured data and to ensure their reproducibility, samples of identical compositions were measured on two different setups. One thermoelectric characterization was carried out in the laboratories at the Johannes Gutenberg University in Mainz, a second characterization was performed at the Centre for Materials Science and Nanotechnology at the University of Oslo (FERMIO). In the following plots we refer to the values measured in Mainz using the suffix "M" after the sample composition, and the suffix "O" for the values measured in Oslo.

Substitution on the cation site allows decoupling changes of the electrical properties from those of the thermal properties. Thus, the charge carrier density of the TTBs can be tuned while

maintaining the crystal structure and the lattice thermal conductivity. Starting from the non-substituted sample $Nb_8W_9O_{47}$ ($x = 0$), the electrical behavior of the TTBs passes from an insulating behavior for the non-substituted sample[44] to a semiconducting behavior for $Nb_4W_{13}O_{47}$ ($x = 4$). The values of the electrical resistivity drop by several orders of magnitude to 3 mΩ·cm for $Nb_4W_{13}O_{47}$ at 1173 K. The electrical resistivity show a similar trend on both devices and their individual values are in very good agreement. An effective increase of the charge carrier concentration upon substitution of Nb by W was confirmed by the Hall measurements (Figure 4.4) and by the decrease of ρ. At room temperature, the difference is most evident and the electrical resistivity decreases from 150 mΩcm (for $x = 3$) to 40 mΩcm (for $x = 4$). At higher temperatures the difference between the resistivity of the two compositions fades out, because the charge carriers are more delocalized due to thermal excitation with a concomitant decrease of the electrical resistivity.
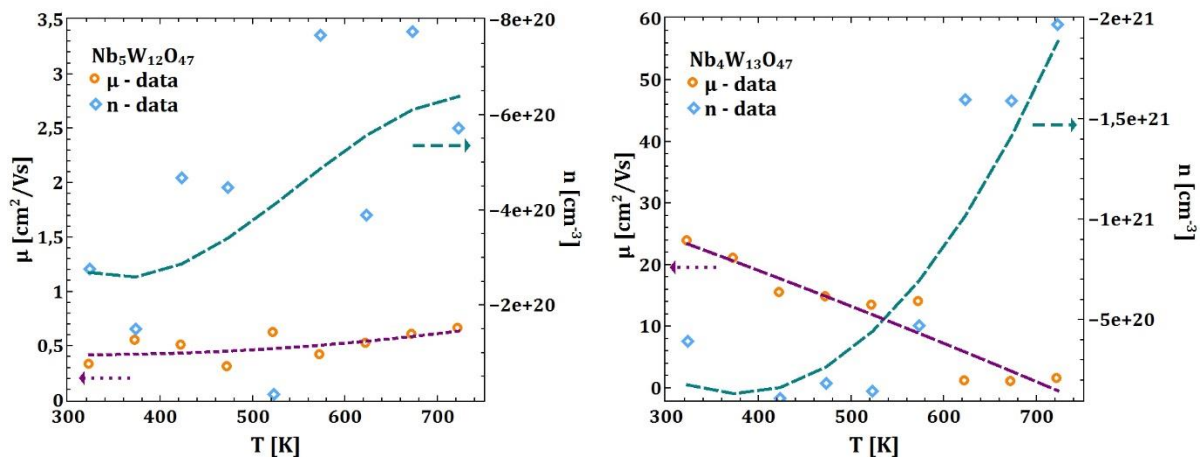

Figure 4.4: Variation of the charge carrier concentration n and carrier mobility μ over temperature for the samples with substitution degree $x = 3$ (left) and $x = 4$ (right). The values of n are negative because the charge carriers are electrons.

The increase of the charge carrier concentration was confirmed also by the Seebeck measurements on both instrumental setups, although not as distinct as for the electrical resistivity. At 1173 K, the measured Seebeck coefficients were -110 µV/K and -95 µV/K for $Nb_5W_{12}O_{47}$ and $Nb_4W_{13}O_{47}$, respectively. All samples show an increase of the thermopower with increasing temperature, which may be associated with an increase of the internal entropy at higher temperatures.
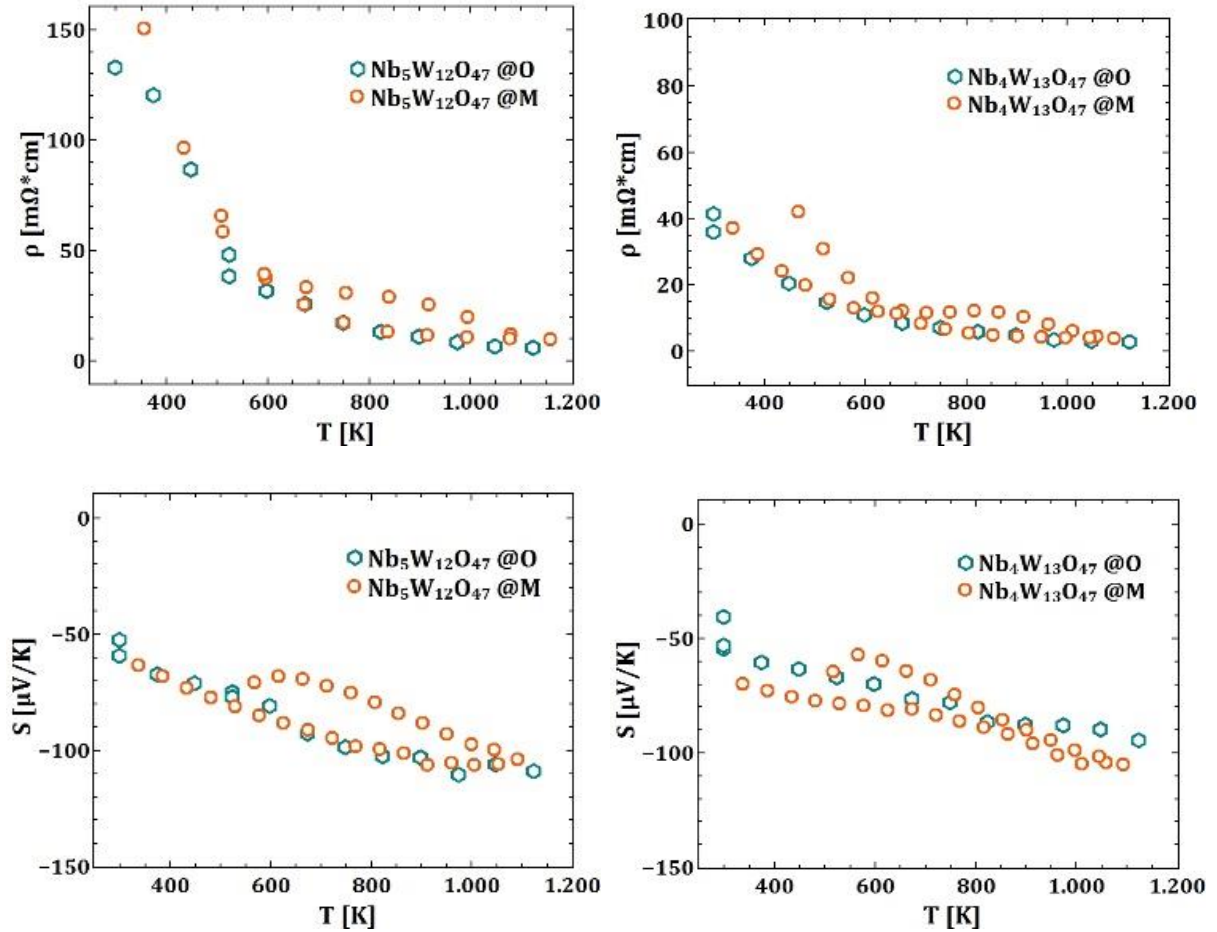
Figure 4.5: Comparison of the measurements of the electrical resistivity ρ and the Seebeck coefficient S. The suffix "M" refers to the measurements done in Mainz; the suffix "O" refers to the measurements done in Oslo (FERMIO). The top plots are relative to the sample with $x = 3$, and the plots on the bottom to the sample with $x = 4$.

As already summarized in Eq. (7), (8), and (9) the total thermal conductivity is the sum of two contributions, the lattice thermal conductivity (κ_L) and the electronic thermal conductivity (κ_{el}). The lattice contribution is a function of the volume of the unit cell (V), the heat capacity (C_p), the phonons mean free path (Λ) and the phonon velocity (v_g), while the electronic contribution is a function of the Lorentz number (L), the electrical conductivity (σ), and the temperature (T).
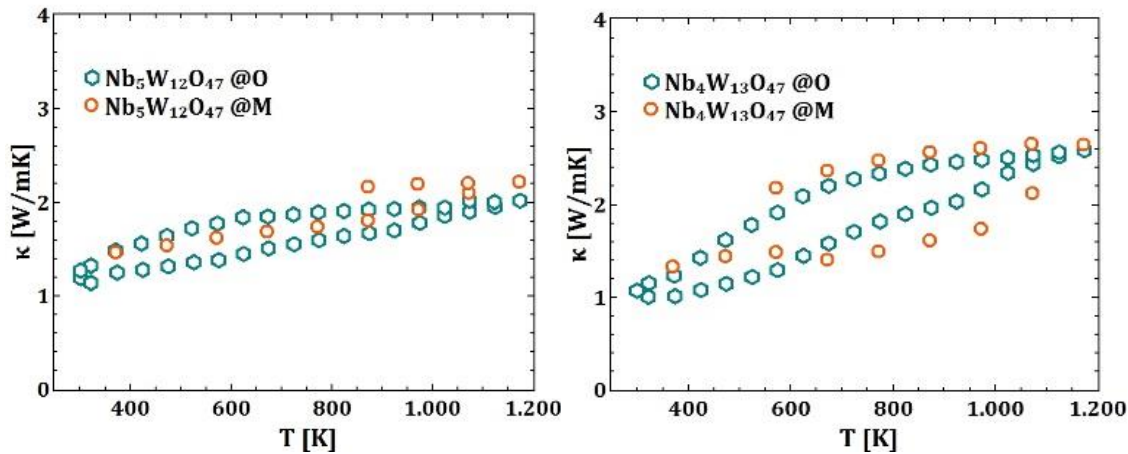
Figure 4.6: Comparison of the measured values of thermal conductivity. For both samples we can observe a good agreement of the results. The hysteresis phenomenon is more evident for the sample $Nb_4W_{13}O_{47}$, probably due to the lower electrical resistivity that further increase the importance of κ_{el} compared to the sample $Nb_5W_{12}O_{47}$.

The thermal conductivities of $Nb_5W_{12}O_{47}$ ($x = 3$) and $Nb_4W_{13}O_{47}$ ($x = 4$) show glass-like behavior at room temperature. The measurements show a similar trend with a good reproducibility of the results. For $Nb_5W_{12}O_{47}$, the values of κ range between 1.2 and 2.2 $Wm^{-1}K^{-1}$. $Nb_4W_{13}O_{47}$ exhibits slightly lower κ values at room temperature, possibly because of increasing internal disorder induced by the stoichiometric changes. With rising temperatures both samples exhibit an increase of the thermal conductivity. This behavior is attributed to the increased weight of the electronic contribution of the thermal conductivity, as κ_{el} is proportional to T. Moreover, the net increase of the electrical conductivity at higher temperatures provides a further boost to the thermal transport. We believe this to be the reason of the increment of κ for $Nb_4W_{13}O_{47}$ ($x = 4$), whose thermal conductivity reaches the value of 2.6 $Wm^{-1}K^{-1}$ at 1173 K. Figure 4.6 shows a hysteresis between the heating and the cooling measurements for both samples, even after repeated cycling. This behavior seems coherent with the small bump after the 500 K observed in the DSC signal (Figure 4.3), and with our measurements of the electrical properties (Figure 4.5). A tentative explanation could be dislocations of the oxygen deficiencies that locally induce small compositional changes. After cooling, the samples had maintained their starting composition and structure, as demonstrated by powder X-ray diffraction (Figure 4.7). Even after several cycles the transport properties

remained constant, indicating the stability of the tetragonal bronzes despite the observed hysteresis effect.
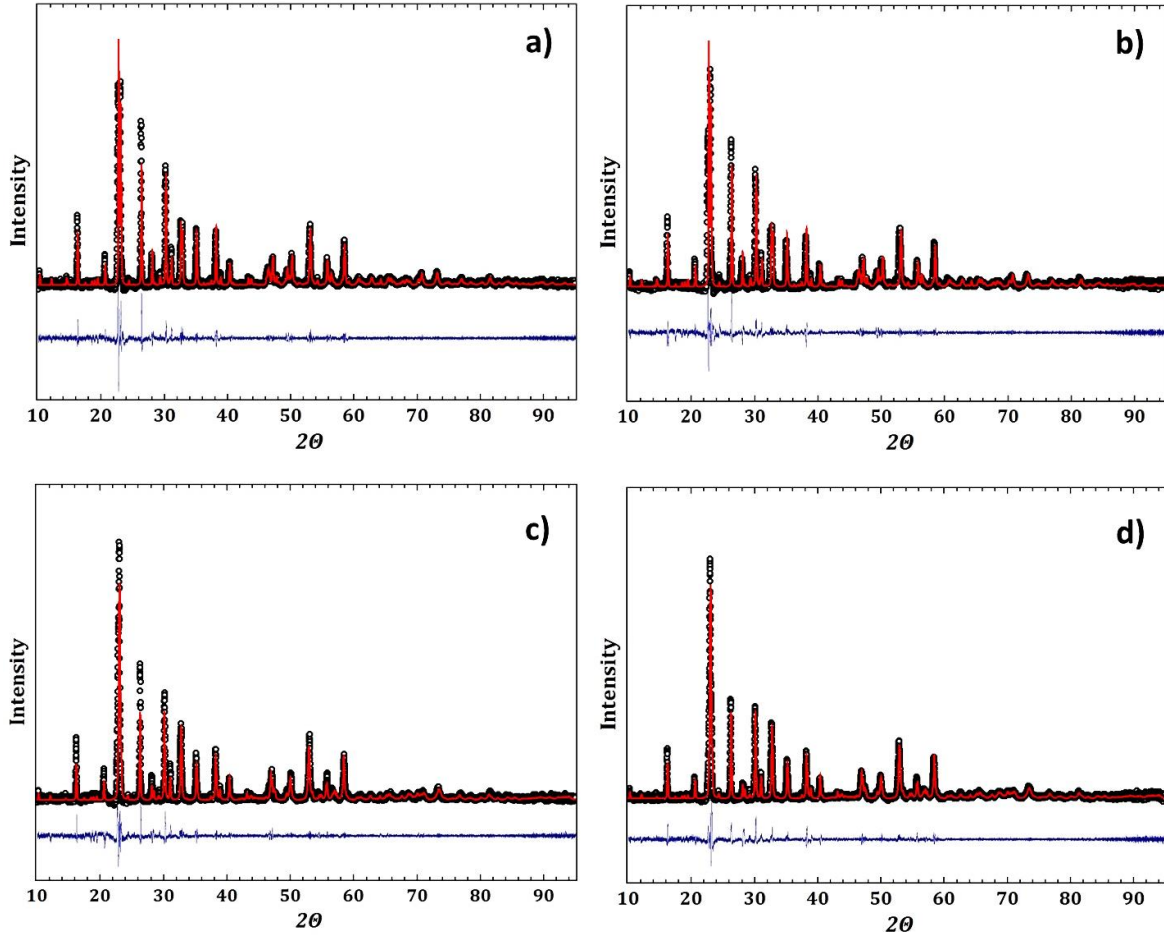

Figure 4.7: Comparison of the refinement of the PXRD data performed on the sample $Nb_5W_{12}O_{47}$ before (a) and after (b) the cycling of the thermoelectric measurements. The same comparison is reported for the sample $Nb_4W_{13}O_{47}$ before (c) and after (d) the cycling.

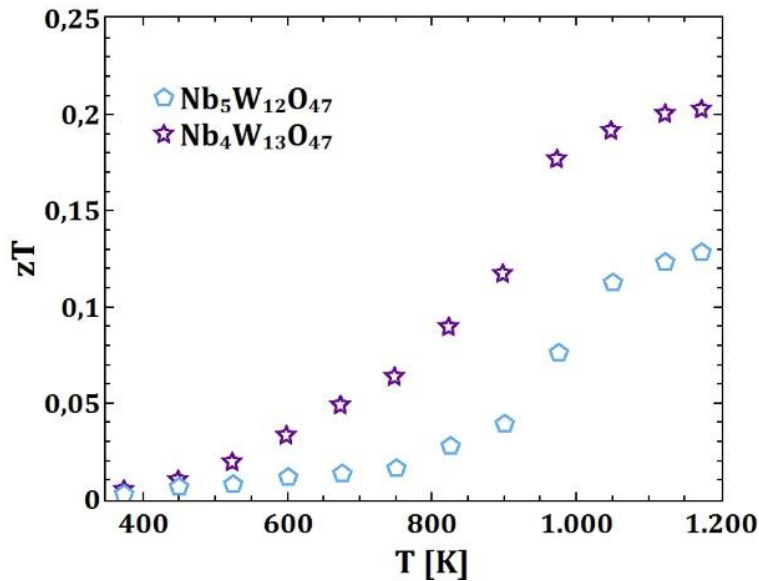**Figure 4.8:** Plot of the dimensionless thermoelectric figure of merit (zT) for the samples with stoichiometry $Nb_5W_{12}O_{47}$ ($x = 3$) and $Nb_4W_{13}O_{47}$ ($x = 4$). The maximum measured value is 0.2 for the sample $x = 4$. For both materials the maximum value of zT is reached around 1000 K, but at 1173 K the figure of merit has not started to decrease yet.

The increase of the charge carrier concentration is reflected as well in the figure of merit, zT. $Nb_4W_{13}O_{47}$ ($x = 4$) shows a $zT = 0.2$ at 1173 K, while a value of $zT = 0.13$ was obtained for $Nb_5W_{12}O_{47}$ ($x = 3$). These values may be compared with the zT values of 0.043 for $Nb_{8-x}W_{9+x}O_{47}$ ($x = 2$) and 0.034 and 0.015 for the representatives with $x = 1$ and $x = 0$. Compared to $Nb_5W_{12}O_{47}$ ($x = 3$), the highest substituted sample shows a zT increase of more than 50 %, which can be assigned to the reduced electrical resistivity, because the values of the remaining transport properties remain essentially unchanged. Close to 1000 K, zT reaches its maximum and remains constant for a temperature range of at least 200 K.

4.4 Summary

In this chapter are reported the thermal stability and the thermoelectric properties of the two representatives of the tetragonal bronzes $Nb_{8-x}W_{9+x}O_{47}$ highest degree of substitution ($x = 3$, 4). The synthesis of bulk quantities with even higher degrees of substitution ($4 < x \leq 5$) yielded no single-phase products, and it appears difficult to increase the substitution level up to $x = 5$. $Nb_5W_{12}O_{47}$ and $Nb_4W_{13}O_{47}$ were structurally and compositionally stable when subjected to thermal cycling. A full and comparative thermoelectric characterization of both compounds on two different instrumental setups in two laboratories showed a high thermal and physical stability of the samples along with a good reproducibility of the measured data. After nine thermal cycles the samples showed no signs of degradation, and the thermal and electrical properties remained unchanged. Replacement of niobium by tungsten in $Nb_{8-x}W_{9+x}O_{47}$ resulted in an increase of the charge carrier concentration, while all other transport properties remained essentially unchanged. As result, the $zT = 0.2$ for the $Nb_4W_{13}O_{47}$ is a promising result for an oxide thermoelectric, in particular considering the fact that this maximum value was achieved and maintained in a temperature interval of 200 K, because a fundamental requirement for thermoelectric applications is a constant high zT over a wide temperature window. Further enhancement of the thermoelectric performance could be achieved by controlling the oxygen deficiencies and by "anion doping".

References

[1]   G. A. Slack, *CRC Handbook of Thermoelectrics*, CRC Press, **1995**.

[2]   P. A. Cox, *The Electronic Structure and Chemistry of Solids*, Oxford University Press, New York, **1987**.

[3]   A. Shakouri, *Annu. Rev. Mater. Res.* **2011**, *41*, 399–431.

[4]   N. Tsuda, K. Nasu, A. Fujimori, K. Siratori, *Electronic Conduction in Oxides*, Springer Berlin Heidelberg, Berlin, Heidelberg, **2000**.

[5]   Y. Tokura, *Science* **2000**, *288*, 462–468.

[6]   I. Terasaki, Y. Sasago, K. Uchinokura, *Phys. Rev. B* **1997**, *56*, R12685–R12687.

[7]   P. Limelette, S. Hébert, V. Hardy, R. Frésard, C. Simon, A. Maignan, *Phys. Rev. Lett.* **2006**, *97*, 46601.

[8]   M. Lee, L. Viciu, L. Li, Y. Wang, M. L. Foo, S. Watauchi, R. a Pascal, R. J. Cava, N. P. Ong, *Nat. Mater.* **2006**, *5*, 537–540.

[9]   Y. Wang, N. S. Rogado, R. J. Cava, N. P. Ong, *Nature* **2003**, *423*, 425–428.

[10]   J. Sugiyama, J. H. Brewer, E. J. Ansaldo, H. Itahara, T. Tani, M. Mikami, Y. Mori, T. Sasaki, S. Hébert, A. Maignan, *Phys. Rev. Lett.* **2004**, *92*, 17602.

[11]   J.-Y. Kim, J.-I. Kim, S.-M. Choi, Y. Soo Lim, W.-S. Seo, H. Jin Hwang, *J. Appl. Phys.* **2012**, *112*, 113705.

[12]   A. I. Klyndyuk, I. V. Matsukevich, *Inorg. Mater.* **2015**, *51*, 944–950.

[13]   W. Koshibae, K. Tsutsui, S. Maekawa, *Phys. Rev. B - Condens. Matter Mater. Phys.* **2000**, *62*, 6869–6872.

[14]   A. A. Taskin, A. N. Lavrov, Y. Ando, *Phys. Rev. B* **2006**, *73*, 121101.

[15]   P. Ruleova, C. Drasar, P. Lostak, C.-P. Li, S. Ballikaya, C. Uher, *Mater. Chem. Phys.*

2010, *119*, 299–302.

[16]   J. Sui, J. Li, J. He, Y.-L. Pei, D. Berardan, H. Wu, N. Dragoe, W. Cai, L.-D. Zhao, *Energy Environ. Sci.* **2013**, *6*, 2916–2920.

[17]   J. Le Lan, Y. C. Liu, B. Zhan, Y. H. Lin, B. Zhang, X. Yuan, W. Zhang, W. Xu, C. W. Nan, *Adv. Mater.* **2013**, *25*, 5086–5090.

[18]   A. V Kovalevsky, A. A. Yaremchenko, S. Populoh, P. Thiel, D. P. Fagg, A. Weidenkaff, J. R. Frade, *Phys. Chem. Chem. Phys.* **2014**, *16*, 26946–54.

[19]   Y. L. Pei, H. Wu, D. Wu, F. Zheng, J. He, *J. Am. Chem. Soc.* **2014**, *136*, 13902–13908.

[20]   L. Gao, J. Wang, L. Li, S. Wang, S. Zhai, S. Liang, G. Fu, *Mater. Chem. Phys.* **2016**, 1–7.

[21]   G. Kieslich, G. Cerretti, I. Veremchuk, R. P. Hermann, M. Panthöfer, J. Grin, W. Tremel, *Phys. Status Solidi* **2016**, *213*, 808–823.

[22]   S. Andersson, A. D. Wadsley, *Nature* **1966**, *211*, 581–583.

[23]   S. Andersson, B. Collén, U. Kuylenstierna, A. Magnéli, *Acta Chem. Scand.* **1957**, *11*, 1641–1652.

[24]   A. Magnéli, *Acta Crystallogr.* **1953**, *6*, 495–500.

[25]   L. A. Bursill, B. G. Hyde, *Acta Crystallogr. Sect. B* **1971**, *27*, 210–215.

[26]   J. M. Allred, R. J. Cava, *J. Solid State Chem.* **2013**, *198*, 10–17.

[27]   G. Andersson, *Acta Chem. Scand* **1954**, *8*, 1599–1606.

[28]   H. Katzke, R. Schlögl, *Z. Krist.* **2003**, *218*, 432–439.

[29]   U. Schwingenschlögl, V. Eyert, *Ann. der Phys.* **2004**, *13*, 475–510.

[30]   K. M. Nimmo, J. S. Anderson, *J. Chem. Soc. Dalt. Trans.* **1972**, 2328–2337.

[31]   S. Kimura, *J. Solid State Chem.* **1973**, *6*, 438–449.

[32]   L. A. Bursill, *Proc. R. Soc. A* **1969**, *311*, 267–290.

[33]   L. Kihlborg, *Acta Chem. Scand.* **1959**, *13*, 954–962.

[34]   A. Magnéli, N. Hofman-Bang, P. Gjertsen, *Acta Chem. Scand.* **1948**, *2*, 501–517.

[35]   P. Gadó, A. Magnéli, R. J. V. Niklasson, J. Brunvoll, M. Hinton, *Acta Chem. Scand.* **1965**, *19*, 1514–1515.

[36]   A. Magnéli, G. Andersson, B. Blomberg, L. Kihlborg, *Anal. Chem.* **1952**, *24*, 1998–2000.

[37]   D. B. Migas, V. L. Shaposhnikov, V. E. Borisenko, *J. Appl. Phys.* **2010**, *108*, 93714.

[38]   M. Backhaus-Ricoult, J. Rustad, L. Moore, C. Smith, J. Brown, *Appl. Phys. A* **2014**, *116*, 433–470.

[39]   B. D. England P J, Booht J, Tilley R J DIdp, *J. Solid State Chem.* **1982**, *44*, 60–74.

[40]   F. Krumeich, a Hussain, C. Bartsch, R. Gruehn, *Zeitschrift für Anorg. und Allg. Chemie* **1995**, *621*, 799–806.

[41]   F. Krumeich, C. Bartsch, R. Gruehn, *J. Solid State Chem.* **1995**, *427*, 420–427.

[42]   F. Krumeich, M. Wörle, A. Hussain, *J. Solid State Chem.* **2000**, *149*, 428–433.

[43]   F. Krumeich, *Acta Crystallogr. Sect. B Struct. Sci.* **1998**, *54*, 240–249.

[44]   C. P. Heinrich, M. Schrade, G. Cerretti, I. Lieberwirth, P. Leidich, A. Schmitz, H. Fjeld, E. Mueller, T. G. Finstad, T. Norby, et al., *Mater. Horiz.* **2015**, *2*, 519–527.

[45]   M. Schrade, H. Fjeld, T. G. Finstad, T. Norby, *J. Phys. Chem. C* **2014**, *118*, 2908–2918.

[46]   M. Schrade, H. Fjeld, T. Norby, T. G. Finstad, *Rev. Sci. Instrum.* **2014**, *85*, 103906-1–8.

[47]   L. J. van der Pauw, *Philips Res. Reports* **1958**, *13*, 1–9.

[48]   L. J. van der Pauw, *Philips Tech. Rev.* **1958**, *20*, 220–224.

[49]   J. He, M. G. Kanatzidis, V. P. Dravid, *Mater. Today* **2013**, *16*, 166–176.

5 Solid state synthesis of MoO$_{3-x}$ Magnéli phases

5.1 Motivation

Molybdenum trioxide (MoO$_3$) is a thermodynamic stable compound under ambient conditions, but exist a large structural variety of binary oxides in the region MoO$_2$ - MoO$_3$. The first X-ray analysis of the molybdenum-oxygen system has been performed by Hägg and Magnéli.[1] Later on has been discovered the presence of at least seven stable or metastable phases with a mixed oxidation states of Mo^{4+} and Mo^{6+}. The structural chemistry of such compounds has been studied and reported several decades ago by Kihlborg.[2–5]

As previously outlined in the "Introduction" chapter, the Magnéli phases and the related "sub-stoichiometric" compounds fulfill many of the requirements for new materials. Indeed, they are interesting for commercial applications thanks to their low cost, to the low or no toxicity, and to their high physical and chemical stability. Among them, the molybdenum oxides attracted much attention due to their potential as catalytic material[6–8] and their possible application in lithium cells.[9] So far, a complete thermoelectric characterization of mixed metal molybdates has not been performed, probably because the internal dynamics taking place in these materials at high temperatures are not completely understood yet.

In this chapter an overview on the MoO$_3$ and MoO$_{3-x}$ systems is given. Along with it, a more detailed analysis of some reduced phases (Mo$_4$O$_{11}$, Mo$_{17}$O$_{47}$, Mo$_{18}$O$_{52}$) is provided. Afterwards the synthesis optimization of bulk materials for the selected phases is presented. In the end, the results of the chemical characterization through the PXRD method are shown.

5.2 The structural chemistry of the molybdenum oxides

In MoO_3, like in most of the transition metal oxides, when the partial oxygen pressure is reduced, the oxidation state of some of the Mo atoms decreases to compensate the lower oxygen content. This compensation induces a rearrangement of the crystal structure by the formation of two defects: oxygen vacancies and crystallographic shear (CS) planes.[10,11] Several stable or metastable sub-oxides have been observed between the compositions MoO_3 and MoO_2: η-Mo_4O_{11}, γ-Mo_4O_{11}, $Mo_{17}O_{47}$, Mo_5O_{14}, Mo_8O_{23}, and $Mo_{18}O_{52}$ (or Mo_9O_{26}). All these compounds have a crystal structure that can be derived from the ReO_3 structure.

5.2.1 α-MoO₃

The fully oxidized compound α-MoO_3 has a layered structure where each layer is made of two nets of distorted MoO_6 octahedra, as shown in Figure 5.1.

The two nets of each layers are connected through edge sharing octahedra along the [001] direction, meanwhile two following adjacent layers along the [010] direction are kept together by weak van der Waal forces. These interlayer connections are made by Mo-O-Mo bonds: one is short (1.734 Å) and strong, the other is longer (2.251 Å) and weaker. Within the same layer, each oxygen atom is then linked to three molybdenum atoms. Two of these connections have the same bond length (1.948 Å), and hence the same strength, while the third one is longer (2.332 Å). This difference in strength is the reason of the intrinsic anisotropy of the MoO_3 crystals.
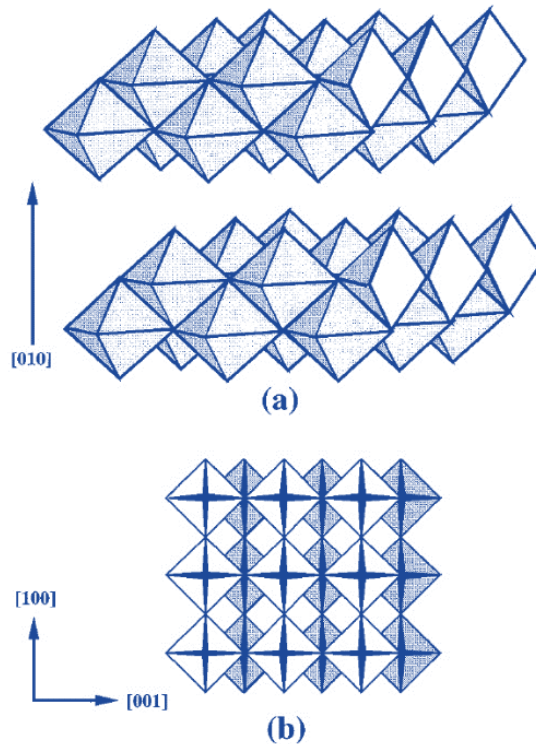
116

Figure 5.1: Schematic representation of the α-MoO$_3$ crystal structure. View of the double distorted octahedral layers along [010] direction (a). A partial portion of two overlapped nets of corner sharing octahedra is shown in (b). Image adapted from literature.[12]

5.2.2 Mo$_{18}$O$_{52}$

The crystal structure of the Mo$_{18}$O$_{52}$ can be derived from the MoO$_3$ structure by crystallographic shear operations as shown in Figure 5.2. The reduction of the Mo/O ratio from 1:3 to 1:2.889 (Mo$_{18}$O$_{52}$) corresponds to the transformation of a subset of octahedra along specific planes from a corner-sharing to an edge-sharing arrangement.[3,10,13]

The structure of the Mo$_{18}$O$_{52}$ phase is a layered structure where the shear is normal to (100) surface. Therefore, this phase is characterized, similarly to the MoO$_3$ phase, by layers joined through low van der Waals forces. The existence of a homologous series of shear structures related to the Mo$_{18}$O$_{52}$ phase has been proposed and it should have the general molecular formula Mo$_n$O$_{3n-m+1}$.[14] The various phases belonging to this series are differentiated by a variation of the spacing of the shear planes and the amount of edge sharing octahedra. However, higher members have only been sparsely observed during TEM studies.[11]
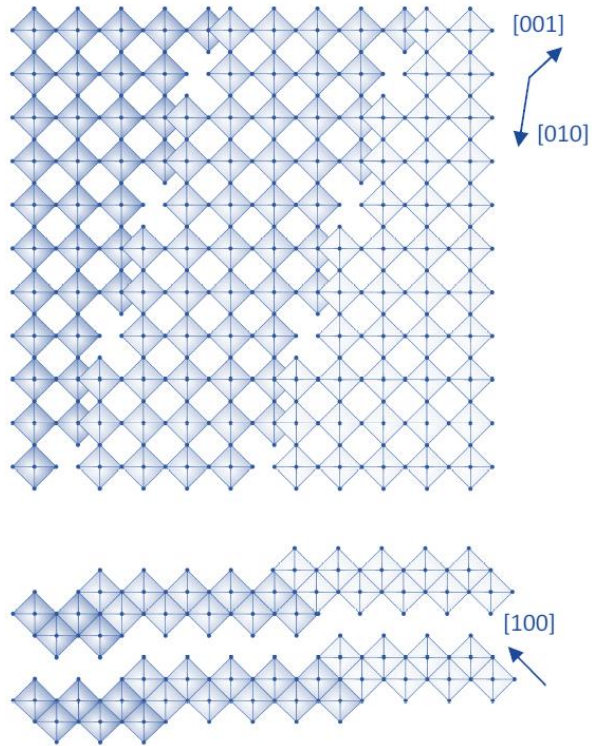
Figure 5.2: A layer of the $Mo_{18}O_{52}$ crystal structure (top), and the relative crystallographic shear operation (bottom). Image adapted from literature.[15]

5.2.3 η-Mo$_4$O$_{11}$ and γ-Mo$_4$O$_{11}$

The γ-Mo$_4$O$_{11}$ and the η-Mo$_4$O$_{11}$ are two modification of the same phase. The first is an orthorhombic high temperature modification which is stable above the 888 K, while the second is a monoclinic modification which can be synthesized at temperatures below the 888 K.[3,16]
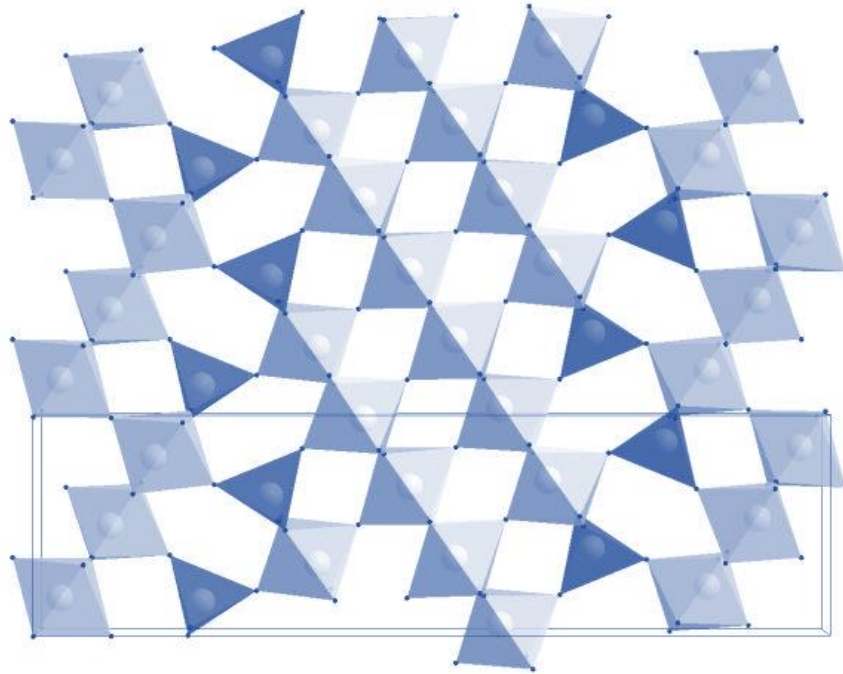
Figure 5.3: Crystal structure of the γ-Mo$_4$O$_{11}$ phase along the [010] direction. The molybdenum atoms are shown in white and the oxygen atoms in dark blue. Image adapted from literature.[15]

Instead of having the CS planes acting as connection between following slabs of ReO$_3$ structure, the distorted octahedra are linked through planes of MoO$_4$ tetrahedra. Both configurations can be described as composed by corner sharing octahedra with four MoO$_4$ tetrahedra per unit cell. The octahedra are strongly distorted as the Mo-O bond distances vary between 170 and 210 pm. In the monoclinic modification (η-Mo$_4$O$_{11}$) the connection of either two MoO$_4$ and two MoO$_6$ polyhedra or two MoO$_4$ and four MoO$_6$ polyhedra leads to the formation of square or hexagonal channels. In the orthorhombic modification (γ-Mo$_4$O$_{11}$) instead, the chains are connected via two MoO$_4$ tetrahedra and three MoO$_6$ octahedra leading to the formation of pentagonal channels (Figure 5.3). In this phase the increased metal to oxygen ratio is overcome by the formation of these MoO$_4$ tetrahedral planes, rather than through the formation of shear planes.

5.2.4 $Mo_{17}O_{47}$

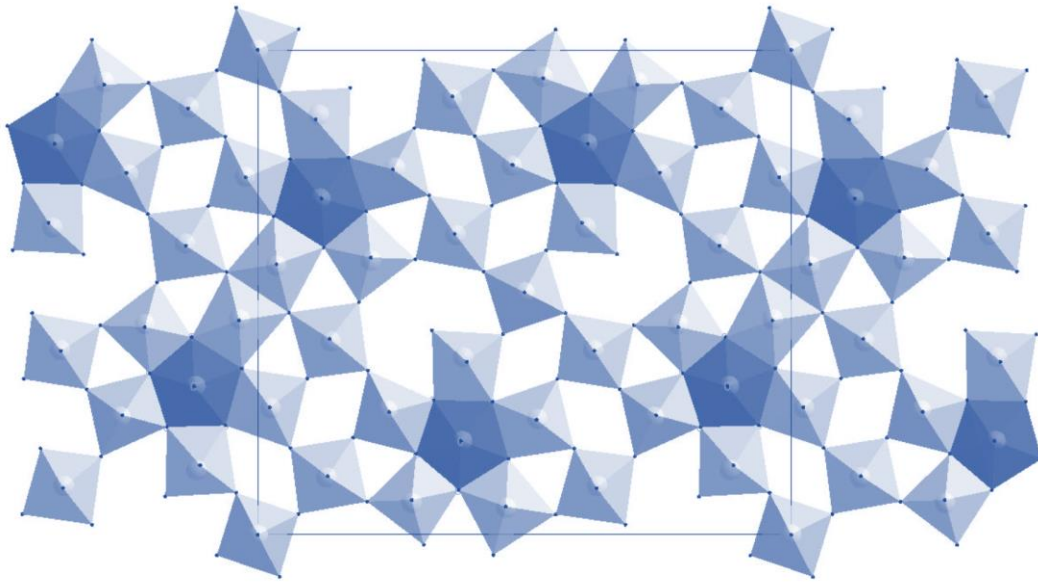**Figure 5.4:** Crystal structure of the $Mo_{17}O_{47}$ phase shown along the [001] direction. This phase is characterized by the formation of pentagonal tunnels filled by metal atoms. Image adapted from literature.[15]

The structure of $Mo_{17}O_{47}$ is characterized by planar polygonal network structures formed by polyhedra linked by corner and edge sharing in two dimensions, leading to the formation of complicated planar networks. The distorted octahedra give rise to the formation of pentagonal tunnel filled by metal atoms. This conformation creates distorted MoO_7 pentagonal bipyramids. Each bipyramid is connected with five octahedra in its equatorial plane leading to the formation of star shaped structures. The networks are connected in the perpendicular direction by shared corners to form a three dimensional network.[4]

5.3   Experimental

5.3.1   Synthesis

The starting materials used for the synthesis of the MoO_{3-x} compounds were molybdenum-(VI)-oxide (Sigma Aldrich; $> 99.5\%$), molybdenum-(IV)-oxide (Sigma Aldrich; $> 99\%$), and pure molybdenum powder (ChemPur; $> 99.95\%$). The samples were prepared by thoroughly grounding stoichiometric amounts of reactants and heating the mixtures in evacuated, sealed quartz ampoules. Before loading them, the ampoules have been cleaned and preheated at 1073 K under dynamic vacuum for 5 hours to ensure dry conditions. After being filled with the proper mixture, the ampoules have been repeatedly evacuated to a pressure of $\approx 10^{-3}$ mbar and flushed with argon, to avoid the presence of oxygen. The high volatility of MoO_3 made it necessary to minimize any temperature gradient within the tubes during the reaction, and this was achieved by keeping the ampoules as short as possible (12mm in diameter, 8 to 10 cm long). The loaded and sealed quartz ampoules were heated in multistep programmable Carbolite (MTF 12/38/400) tube furnaces, and a heating rate of 5 K/min was used. The samples were kept at reaction temperatures for several days or weeks depending on the synthesized composition. After the reaction period the furnace was cooled down to room temperature.

After verifying the purity of the synthesized powders, attempts of compaction have been done for all the compositions. The powders have been loaded in a 20 mm diameter graphite die and sintered in a SPS machine (FCT HP D 25). To prevent any contamination of the samples, a carbon foil has been used to avoid the contact between the powders and the internal surfaces of the die. Afterwards, the samples have been heated up to a proper sintering temperature ($\leq$ the reaction temperature) applying a pressure of 50 MPa and a heating rate of 100 K/min. Unfortunately, all the investigated condition for the sintering of dense pellet have produced no results. All the samples, independently from the composition, showed after the sintering the formation of side phases (mostly Mo_4O_{11}, Mo_8O_{23}, $Mo_{18}O_{52}$ and MoO_3), making them not suitable for a thermoelectric characterization.

5.3.2   Characterization

The molybdenum Magnéli phases and in general the reduced molybdenum oxides are characterized by a blue-violet color of the shiny crystals, which makes it quite easy to give a first impression about the result of a certain reaction.

The purity of the precursors was checked by X-ray diffraction and the same technique was used to characterize the products of the reactions. The samples for the PXRD were prepared by thoroughly ground the reaction product in agate mortars. The data were collected on a two-circle-diffractometer Siemens D5000 equipped with Ge (220) primary beam monochromator ($CuK_{\alpha}1 = 154.0596$ pm) and a Braun M50 position sensitive detector in transmission geometry. The data for phase analysis were collected from 10° to 90° 2Θ with a step size of 0.039° 2Θ and a time of 1.55 seconds per step.

Crystalline phases were identified according to the PDF-2 database using the software Bruker AXS EVA. Full profile fits (Pawley and Rietveld) were performed with TOPAS Academic 4.1[17] applying the fundamental parameter approach.

5.4   Results and discussion

5.4.1   Synthesis of $Mo_{18}O_{52}$

A mixture of MoO_2 + MoO_3 and a mixture of pure Mo and MoO_3 have been used to obtain phase pure $Mo_{18}O_{52}$. Several reaction temperatures ranging from 600°C to 750°C have been investigated for the same purpose. The stoichiometric amounts of the precursors (Table 5.1) have been weighted and homogenised and then processed as described in Section 5.3.1.

	M [g/mol]	n [mmol]	m [mg]
Mo	95.94	1.31	125.7
MoO₃	143.94	33.97	4889.6
Mo₁₈O₅₂	2558.92	1.96	5015.3

Table 5.1: Stoichiometric amounts of the used precursors and of the obtained product for the synthesis of the $Mo_{18}O_{52}$ phase.

Polycrystalline samples of $Mo_{18}O_{52}$ have been obtained after reacting a mixture of pure Mo and MoO_3 at 973 K for 36 h (or at 923 K for 48 h). The reactions carried out at higher temperatures (above 973 K) gave inhomogeneous mixtures of different phases including Mo_4O_{11}, Mo_8O_{23}, $Mo_{18}O_{52}$ and MoO_3. When the starting mixture was composed of the two molybdenum oxides, MoO_3 was present as side phase at almost every temperature.

The refinement of the diffraction data has been performed on of the purest sample obtained at 973 K. Besides $Mo_{18}O_{52}$, also MoO_3 has been taken into account in the fit. The crystal structure data for the fit profile have been obtained from Pearson's Crystal Database. The R_{wp} value for the refinement was 4.96. Without taking MoO_3 into account the R_{wp} value was 5.50, still remaining within an acceptable range.
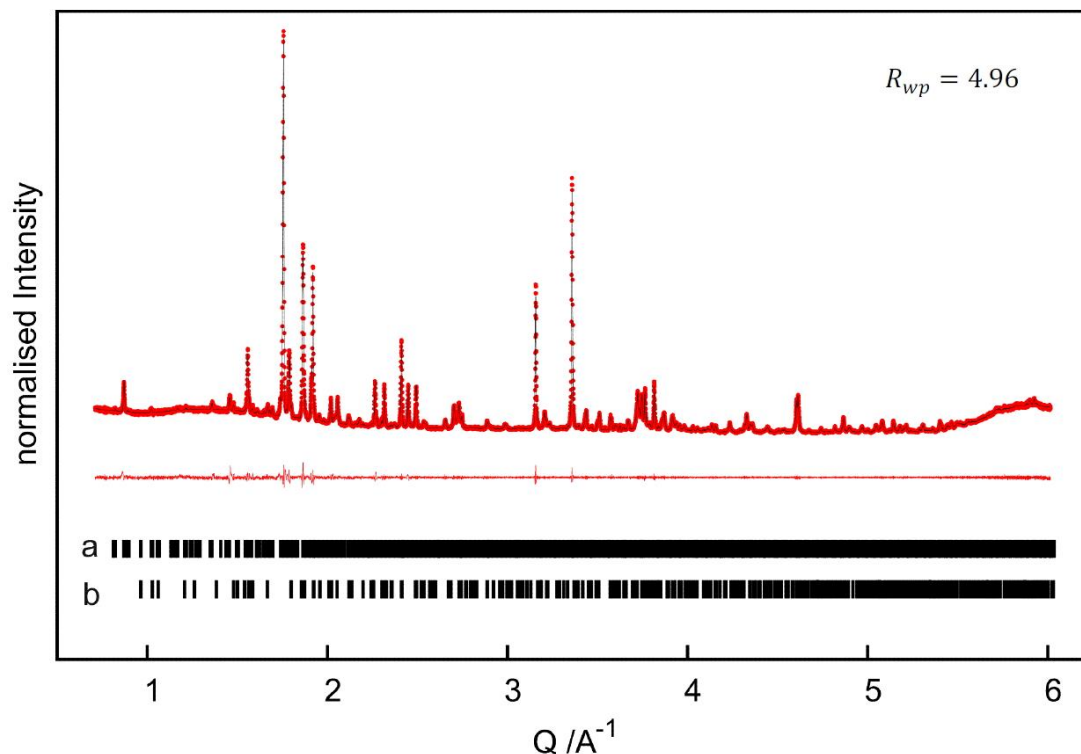
Figure 5.5: Refinement of the PXRD pattern for the phase $Mo_{18}O_{52}$. The measured points (reds dots), and the calculated profile (black line) are reported. Below, the profile difference (solid red line) and the Bragg's reflections for the $Mo_{18}O_{52}$ (a) and MoO_3 (b) are shown.[15]

5.4.2   Synthesis of Mo₄O₁₁

The study of the best conditions for the synthesis of pure Mo_4O_{11} has been carried out investigating both the use of different precursors ($Mo + MoO_3$; $MoO_2 + MoO_3$) and different reaction temperatures in the range 923-1053 K. The best results have been obtained using a mixture of the two molybdenum oxides, in the stoichiometric amounts reported in Table 5.12, and a reaction temperature of 1023 K. The prepared mixture has been loaded into an evacuated quartz ampoule and let react at the desired temperature for a total time of six days. In order to obtain a homogeneous purity, the ampoules have been opened, the mixture grinded and successively resealed in a quartz ampoule each two days.

	M [g/mol]	n [mmol]	m [mg]
MoO_2	127.94	8.93	1142.5
MoO_3	143.94	28.8	3857.6
Mo_4O_{11}	559.76	8.93	5000.1

Table 5.2: Stoichiometric amounts of used reactants and obtained product for the synthesis of the Mo_4O_{11} phase.

The reaction products were consisting of homogeneous blue-purple powders which were finely ground for powder X-ray diffraction. In some cases, MoO_3 was partially transported via the gas phase to the cold end of the ampoule leading to incomplete reactions. Therefore, ampoules containing large, transparent, light grey crystals were discarded.
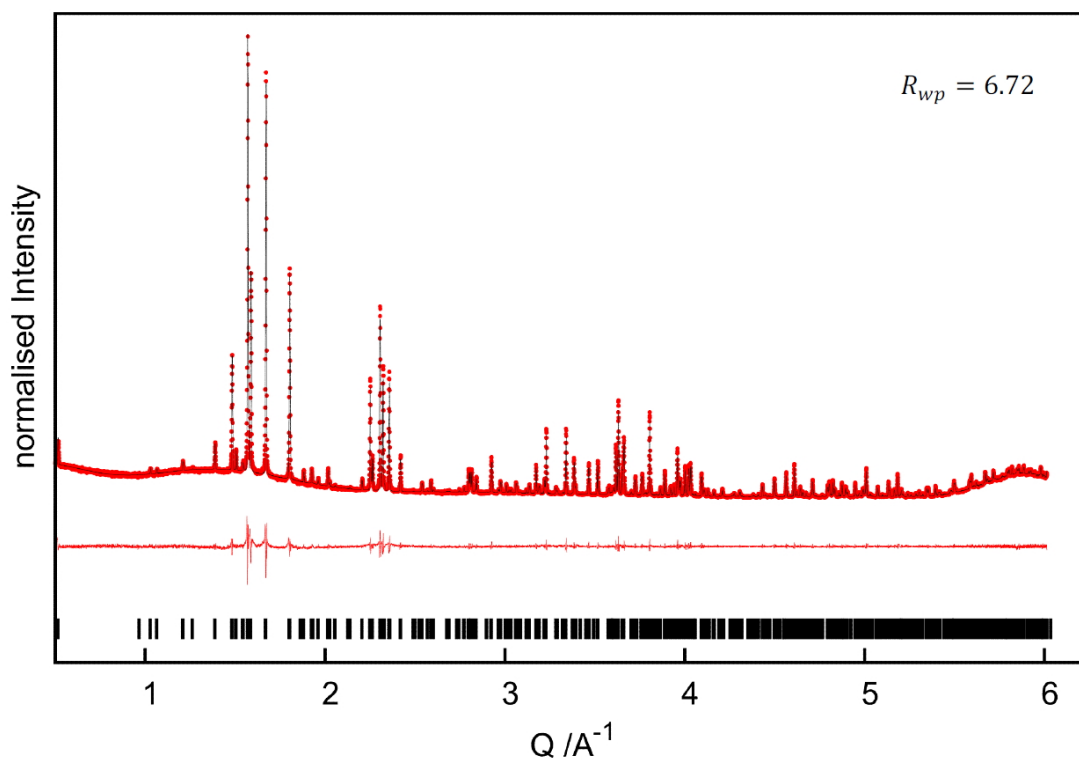

Figure 5.6: Refinement for the X-ray data (red dots) of Mo_4O_{11} and calculated profile (black line). The profile difference (red solid line) and the Bragg's reflections are reported below.[15]

Powder X-ray diffraction data have been collected for the samples without MoO_3 transport. A refinement has been performed on the diffraction data and is shown in Figure 5.6. The R_{wp}

value for the fit was 6.72. Since every reflection could be assigned to the Mo_4O_{11} phase, and the calculated lattice parameters were consistent with the parameters reported in the Pearson's crystal database, the sample has been considered to be phase pure with respect to the powder X-ray data.

There were several attempts to synthesize also the low-temperature modification of Mo_4O_{11} (η-Mo_4O_{11}) which forms below 888 K. Ampoules have been heated to 773 K and 823 K for several weeks, but no reaction could be observed at 773 K. In the ampoules heated to 823 K, the high-temperature and the low temperature modification of Mo_4O_{11} as well as MoO_2 and MoO_3 have been identified via X-ray diffraction after reaction times of two weeks. A further heating or a longer reaction time brought both to the formation of $Mo_{17}O_{47}$ as additional phase.

5.4.3   Synthesis of $Mo_{17}O_{47}$

According to the study of Kihlborg[3] the reaction times needed for the formation of this phase are very long. He reported that this phase is stable below the 833 K and it decomposes into orthorhombic Mo_4O_{11} and Mo_8O_{23} above 903 K. Polycrystalline samples of pure $Mo_{17}O_{47}$ have been obtained after a reaction time of six weeks, at a temperature between 773 K and 823 K. To ensure a good quality of the products, a grinding of the powders after each week of reaction was necessary. In Table 5.3 are reported the stoichiometric amounts of reactants used for the synthesis of $Mo_{17}O_{47}$.

	M [g/mol]	n [mmol]	m [mg]
MoO_2	127.94	8.4	1074.7
MoO_3	143.94	27.3	3929.6
$Mo_{17}O_{47}$	2382.98	2.1	5004.3

Table 5.3: Amounts of precursors and products for the synthesis of the $Mo_{17}O_{47}$ phase.

A refinement of the crystal data measured on the purest sample has been performed and is shown in Figure 5.7. The lattice parameters and all the crystal data for the refinement have been obtained from the Pearson's Crystal Database. The R_{wp} value of the fit is 5.94 and since

no residual intensities have been detected after the refinement, the sample has been considered to be pure phase with respect to the X-ray data.
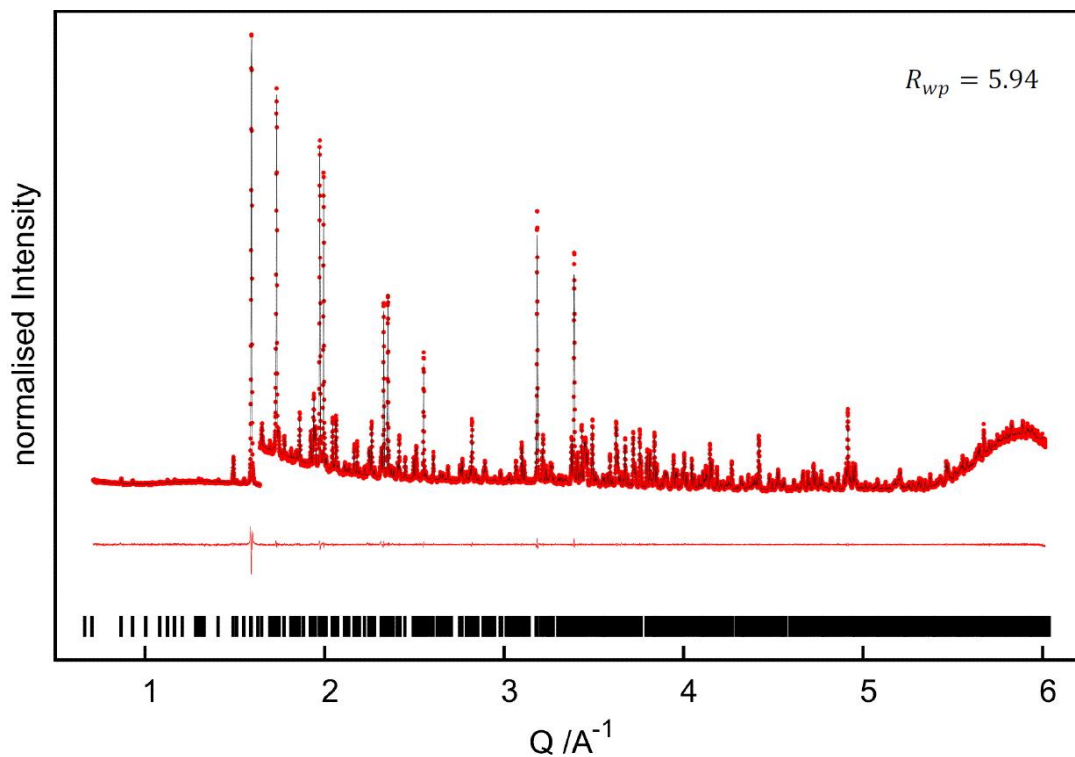

Figure 5.7: PXRD pattern (red dots) and calculated theoretical profile (black line) for the phase $Mo_{17}O_{47}$. For $Q > 1.64$, the intensities are multiplied by four to have a better visualization. The fit difference (red solid line) and the Bragg's reflections are also reported.[15]

5.5 Summary

In this chapter the synthesis conditions of a series of Mo(V)-Mo(VI) mixed valence metal oxides have been studied and optimized. According to semi-quantitative X-ray diffraction investigations γ-Mo_4O_{11}, and $Mo_{17}O_{47}$ were prepared as phase pure bulk samples. X-ray diffraction data for the reaction product of the $Mo_{18}O_{52}$ synthesis showed $Mo_{18}O_{52}$ as the main phase with some small impurity of MoO_3. Anyway, the achieved purity of this last phase remains within an acceptable range. Hence the parameters chosen for the synthesis of the selected phases can be considered as promising for obtaining pure phase compounds. In order to use Magnéli phases in thermoelectric devices it is necessary to obtain robust modules. Spark plasma sintering (SPS) technique has been used to consolidate dense pellets, but it was not possible to obtain phase pure samples after the sintering process because various side phases were formed. If dense pellets of the molybdenum Magnéli phases can be obtained without decomposition, a thermoelectric characterization of these compounds should be performed. The TE properties of the titanium and the tungsten Magnéli phases have already been examined and a remarkably low thermal conductivity is expected also for the molybdenum Magnéli phases as a consequence of the intrinsic shear structures of such compounds. Therefore, a further optimization of the sintering parameters or the investigation of other possible techniques for the compaction of the molybdenum mixed valence oxides has to be thoroughly studied.

References

[1]   G. Hägg, A. Magnéli, *Ark. Kemi Miner. Geol* **1944**, *19 A*, 1–14.

[2]   L. Kihlborg, A. Magnéli, *Acta Chem. Scand.* **1955**, *9*, 471–474.

[3]   L. Kihlborg, *Acta Chem. Scand.* **1959**, *13*, 954–962.

[4]   L. Kihlborg, *Acta Chem. Scand.* **1960**, *14*, 1612–1622.

[5]   S. Åsbrink, L. Kihlborg, *Acta Chem. Scand.* **1964**, *18*, 1571–1573.

[6]   K. Murugappan, C. Mukarakate, S. Budhi, M. Shetty, M. R. Nimlos, Y. Román-Leshkov, *Green Chem.* **2016**, *18*, 5548–5557.

[7]   K. Chary, *J. Catal.* **2004**, *226*, 283–291.

[8]   H. Hu, I. E. Wachs, *J. Phys. Chem.* **1995**, *99*, 10911–10922.

[9]   M. Icovi, S. Panero, A. D'Agate, G. Pistoia, C. Temperoni, *J. Electroanal. Chem.* **1979**, *102*, 343–349.

[10]   L. A. Bursill, *Proc. R. Soc. A* **1969**, *311*, 267–290.

[11]   L. A. Bursill, *Acta Crystallogr. Sect. A* **1972**, *28*, 187–191.

[12]   R. L. Smith, G. S. Rohrer, *J. Solid State Chem.* **1996**, *124*, 104–115.

[13]   A. Magnéli, N. Hofman-Bang, P. Gjertsen, *Acta Chem. Scand.* **1948**, *2*, 501–517.

[14]   L. Kihlborg, *Ark. Kemi.* **1963**, *21*, 471–495.

[15]   K. S. Weldert, Synthesis, Optimization and Characterization of Mo(V)-Mo(VI) Mixed-Valence Metal Oxides (Diplomarbeit), Johannes Gutenberg Universität Mainz, **2012**.

[16]   A. Magnéli, *Acta Chem. Scand.* **1948**, *2*, 861–871.

[17]   A. A. Coelho, *TOPAS-Academic 4.1 Computer Software*, **2007**.

6   Conclusions

This thesis focused on the synthesis optimization, the stability study, and the thermoelectric characterization of binary and ternary early transition metal oxides. The compounds studied in this work were chosen due to their adaptive structure. The peculiarity of such materials is the presence of a series of crystallographic defects that guarantee low values of the thermal conductivity. Furthermore, the possibility of tuning the electrical properties independently from the thermal properties, make them very attractive from a thermoelectric point of view.

The first part of this work discussed the optimization of the $WO_{2.90}$ Magnéli phase. This n-type material is characterized by a metallic behaviour, hence to increase its thermoelectric properties an effective manipulation of the charge carrier concentration (n) is needed. An increase of the oxygen content, that in turn reduced n, was achieved by adding WO_3 nano-powders to the starting composition (5 and 10 wt% respectively). As a consequence, the thermoelectric properties were modified without affecting the crystal structure. As confirmed by PXRD investigation, the added amount of WO_3 powders was not enough to induce a phase change. In this way the intrinsic defects characteristic of the Magnéli phases, and therefore the low values of the thermal conductivity, were preserved. Moreover, the decrease of the charge carrier concentration positively affected the electronic properties. This translated in an optimization of the figure of merit that reached the value of 0.24 at 1223 K.

Similar defects to that found in the Magnéli phases have been observed in the compounds belonging to the tetragonal tungsten bronze (TTB) series $Nb_{8-x}W_{9+x}O_{47}$. Due to their structural complexity and the possibility of tuning the electronic properties by cation substitution x and oxygen deficiency δ, compounds with low substitution degree ($x = 0, 0.075, 0.1, 1,$ and 2) have been synthesized to conduct a preliminary study on the thermoelectric properties of such materials. The samples showed n-type conduction and a relatively high electrical resistivity (> 20 mΩcm) along with high negative Seebeck coefficients (ranging between -280 and -65 μV K^{-1}). The substitution of niobium with tungsten introduces electrons into the system leading to an increase of the electrical conductivity and a reduction of the thermopower. The structural

complexities, the nano-sized grains, and the high concentration of crystal defects resulted in glass-like values of the thermal conductivities. Furthermore, the oxygen deficiency δ could be reversibly varied by equilibrating the sample in a controlled atmosphere at 1173 K. A maximum oxygen deficiency of $\delta = 0.3$, equivalent to a change in substitution degree of $x = 0.6$, has been determined for $Nb_8W_9O_{47-\delta}$. The highest power factor and zT have been registered for the highest substituted sample ($Nb_6W_{11}O_{47}$) with values of 0.8 mWcm^{-1}K^{-2} and 0.043, respectively, at 973 K. These results confirmed the expected improvement of the thermoelectric properties upon substitution.

For this reason, a further investigation on the highly substituted compositions of the series was carried out. The second part of the investigation focused on the highly substituted compounds of the series: $Nb_5W_{12}O_{47}$ ($x = 3$), $Nb_4W_{13}O_{47}$ ($x = 4$) and $Nb3W_{14}O_{47}$ ($x = 5$). The compositions $x = 3$ and $x = 4$ have been synthesized as polycrystalline phase pure samples, meanwhile the synthesis of $x = 5$ led to the formation of multiphase samples ($Nb_4W_{13}O_{47}$ and WO_3), indicating that the physical limit of substitution is probably reached in proximity of the $x = 4$ composition. The chemical and the physical stability of the phase pure compounds ($x = 3$ and $x = 4$) when subjected to thermal cycling has been studied, and the complete thermoelectric characterization of these samples has been performed. A second set of measurements has been done on the devices available at the University of Oslo (FERMIO), to verify the reproducibility of the obtained results. The X-ray analysis performed at different stages of the investigation and the agreement of the cycled measurements confirmed the high stability of these materials as well as the good reproducibility of the measured values. The substitution of Nb with W further reduced the electrical resistivity as a consequence of the increase of n. In the end, the zT value for $Nb_4W_{13}O_{47}$ ($x = 4$) compared to that measured for the unsubstituted sample $Nb_8W_9O_{47}$ ($x = 0$) registered an increase of one order of magnitude, passing from 0.016 ($x = 0$) to 0.2 ($x = 4$).

The last part of this work focused on the synthesis of a series of molybdenum mixed valence metal oxides belonging to the Magnéli phases. Through the optimization of the synthesis conditions, it was possible to obtain phase pure polycrystalline powders of γ-Mo_4O_{11}, $Mo_{17}O_{47}$, and $Mo_{18}O_{52}$. The purity of the synthesized products has been confirmed by PXRD measurements. Therefore, the chosen parameters can be considered as promising for the synthesis of pure phase samples of the selected compounds. In order to obtain dense pellets, a

132

spark plasma sintering machine has been used. Unfortunately, it was not possible to consolidate phase pure pellets because any attempts led to the formation of side phases. Therefore, before performing a proper thermoelectric characterization of these materials, an accurate study of the sintering conditions has to be carried out.

It can be concluded that this work showed the high potential of metal oxides as thermoelectric materials for high temperature applications. Simple optimization techniques, like cation substitution or manipulation of n through the control over the oxygen content of the samples, have showed their effectiveness in increasing the TE performances of the studied metal oxides. Therefore, there is optimism around these materials, also because the research on thermoelectric oxides is a relatively new field with still a lot of space for further improvements.